Dissertation

Operando SFG Spectroscopy of Pt/ZrO_2 ALD Model Catalysts

Carried out for the purpose of obtaining the degree

Doctor rerum naturalium

Under the supervision of

Univ. Prof. Dr.rer.nat. Günther Rupprechter

and

Dr.rer.nat. Christoph Rameshan

Institute of Materials Chemistry, E165

Submitted at Technische Universität Wien

Faculty of Technical Chemistry

by

Verena Pramhaas

00716140

Eidesstattliche Erklärung

Ich erkläre an Eides statt, dass die vorliegende Arbeit nach den anerkannten Grundsätzen für wissenschaftliche Abhandlungen von mir selbstständig erstellt wurde. Alle verwendeten Hilfsmittel, insbesondere die zugrunde gelegte Literatur sind in dieser Arbeit genannt und aufgelistet. Die aus den Quellen wörtlich entnommenen Stellen sind als solche kenntlich gemacht.

Das Thema dieser Arbeit wurde von mir bisher weder im In- noch Ausland einer Beurteilerin/einem Beurteiler zur Begutachtung in irgendeiner Form als Prüfungsarbeit vorgelegt. Diese Arbeit stimmt mit der von den Begutachterinnen/Begutachtern beurteilten Arbeit überein.

Wien, _____ _____

Unterschrift

Abstract

This thesis focused on non-linear optical sum frequency generation (SFG) spectroscopy and its application to examine industrially relevant supported Pt/ZrO_2 model catalysts. Complementary techniques such as transmission electron microscopy, x-ray diffraction and x-ray photoelectron spectroscopy were used to fully characterize the samples and to support and extend findings of the SFG measurements.

The studied model catalysts consisted of different thin Pt structures (from nanoparticles to continuous films) on supporting oxide layers and were produced by atomic layer deposition, which is industrially relevant due to its already extensive use in manufacturing of electronics. The model systems were characterized by bulk and surface methods to enable later comparison between different samples and correlation of spectroscopic results with surface structures.

The introduction to the SFG measurements includes an overview of the SFG process and setup as well as reference studies for a thorough description of the system. Followingly, CO adsorption studies were conducted for catalyst characterization, and CO oxidation reaction studies were performed in combination with mass spectroscopy. The SFG adsorption studies did not only monitor the increasing surface roughness of samples with less Pt deposited, but also revealed CO dissociation on rough samples at 250 °C. The reaction studies unraveled higher reaction onset temperatures for samples with less deposited Pt, which was unexpected, as smaller particles and metal-oxide interfaces are believed to promote CO oxidation. Complementary near ambient pressure X-ray photoelectron spectroscopy measurements explained this "discrepancy" by indicating that even in oxidative environment CO dissociation was occurring on rough Pt films.

Kurzfassung

Die vorliegende Arbeit befasst sich mit der nicht linearen Summenfrequenzspektroskopie (SFG) und deren Anwendung zur Untersuchung von Pt/ZrO_2 Modellkatalysatoren mit industrieller Relevanz. Zusätzliche Untersuchungsmethoden wie Transmissionselektronenmikroskopie, Röntgendiffraktion und Röntgenphotoelektronenspektroskopie wurden eingesetzt um die Proben umfassend zu charakterisieren und die SFG Ergebnisse zu unterstützen.

Die Modellkatalysatoren wiesen unterschiedliche Platinoberflächenstrukturen (von Nanopartikeln bis kontinuierlichen Filmen) auf, welche auf unterstützende Oxidschichten aufgebracht waren. Die Platin und Zirkonoxid Schichten wurden per Atomlagenabscheidung (ALD) hergestellt, einer Methode die bereits in unterschiedlichen mikroelektronischen Fertigungsprozessen eingesetzt wird und deshalb industriell relevant ist. Die Modellsysteme wurden mit Volumen und Oberflächenmethoden charakterisiert, um die Proben untereinander zu vergleichen und um Ergebnisse aus den spektroskopischen Messungen den unterschiedlichen Oberflächenstrukturen zuzuordnen.

Die Einführung in das SFG System beinhaltet einen Überblick über den nicht linearen optischen Effekt, den experimentellen Aufbau und Referenzmessungen. Danach werden CO Adsorptionsmessungen zur weiteren Charakterisierung der Modellkatalysatoren gezeigt, sowie Reaktionsmessungen für CO Oxidation in Kombination mit Massenspektrometrie. In den SFG Adsorptionsmessungen konnte eine steigende Oberflächenrauigkeit für Filme mit weniger Platin Abscheidezyklen (und ausgeprägter Partikelstruktur) gezeigt werden. Zusätzlich wurde für raue Oberflächen CO Dissoziation ab 250 °C beobachtet. Vergleiche der Reaktionsmessungen zeigten höhere Reaktionstemperaturen für Proben mit weniger Platin. Dieses Ergebnis war unerwartet, da rauere Metallteilchen und Metall-Oxidgrenzflächen die Reaktivität erhöhen sollten. Zusätzliche Röntgenphotoelektronenspektroskopie bei erhöhten Drücken (NAP-XPS) konnte diese Unstimmigkeit erklären, da gezeigt werden konnte, dass CO Dissoziation auf rauen Filmen auch in oxidierender Atmosphäre auftritt.

Table of Content

1 Introduction and Motivation

Catalysis plays a key part in modern economy. Catalysts are and have for many decades been important for various processes in chemical industry, e.g. for the production of fertilizers, pharmaceutics and fuels. In addition, catalysts are used for environmental protection, e.g. cars have a catalytic converter to reduce toxic waste gases like carbon monoxide. Another arising field of use for catalysis is the production and storage of energy to satisfy the increasing demand in renewable energies [1, 2]. Examples are catalysts used in fuel cells, utilizing hydrogen or methane to produce electricity, or conversion of greenhouse gases to fuel for energy generation [3]. Development of new or improved catalysts can allow companies to outperform their competitors and catalytic research is therefore strongly represented in industry.

All fields of application require the permanent advancement of catalysts to improve performance, selectivity towards desired end products and stability for long-lasting use. Furthermore, the availability of materials is important in the design. Today, many improvements on catalyst materials are still made by trial and error testing of material combinations, rather than by systematic research. Even structures and combinations of several catalysts used in industry already decades ago have never been determined. In addition, nowadays very complex base materials can easily and reproducibly be prepared (like differently structured oxides, metal organic frameworks, zeolites, perovskites and so on), combining various elements. In many cases these are not complete catalysts themselves, but are used as supports for well dispersed active (nano) particles. The sheer number of structures, support materials, dopants, deposition methods and nano particle compositions makes it impossible to find the best catalyst by testing all possible combinations. It is therefore essential to understand the influence of different materials properties on a reaction, to tailor the catalyst according to the specifications.

Most times it is impossible to gain detailed knowledge on the influence of different components of a catalyst using industrial catalysts, as they are very complex in both composition and structure. For fundamental research they are therefore often substituted by model catalysts of different complexity that allow focusing on special characteristics (surface terminations, support interfaces), and enable the use of special characterization techniques. For catalyst research it is especially important to apply surface science techniques to investigate the surface layers of a catalyst, which are responsible for catalyzing the reaction, and the adsorbates, which not only include

educts but also reaction intermediates that allow the identification of reaction pathways. These surface science methods often have special requirements on sample geometry, like flat surfaces, and electric conductivity, adding more constraints to the investigated catalyst models. The induced discrepancy between model catalysts and industrial catalysts is called the "materials gap". At the same time nearly all surface science methods require ultra-high vacuum (UHV) [4] and many model catalysts would have severe contamination in ambient pressure and are therefore only prepared and characterized in UHV. This difference to the industrially used ambient to high pressures is called the "pressure gap". In recent years increasing efforts are made to design more complex model catalysts and to apply special measurement setups that allow measuring model catalysts under more realistic reaction conditions to close these gaps and increase the relevance of data gathered from model studies [5].

Work in this thesis focuses on Pt model catalysts supported on ZrO_2. Pt was chosen for its unmatched use in a broad range of catalytic processes. The most well-known application is Pt in automotive catalytic converters and it will most likely be used in fuel cells. While Pt is superior to other materials in several applications [6], the limited availability as a noble metal is of great concern [7-9], thus many studies focus on reducing the amount of Pt required. This can be achieved by using nano particles with maximized numbers of active sites per amount of Pt, alloying metal that enhance the activity by opening up additional pathways for reactions, and by using support materials [10-12], e.g. oxide support interfaces acting as oxygen donors. The Pt of our model catalysts was therefore supported on zirconia to obtain metal-oxide interfaces.

In the following chapter, the main surface science techniques used in this study, sum frequency generation (SFG) spectroscopy and near ambient pressure x-ray photoelectron spectroscopy (NAP-XPS), will be presented. They were selected due to their suitability to bridge the "pressure gap" and work in relevant reaction pressure regimes. The next chapter will focus on the Pt/ZrO_2 model catalysts and their structural characterization. This will be followed by an introduction to our laboratory setup for SFG and chapters on CO adsorption. Afterwards, reaction measurements of SFG and NAP-XPS performed during CO oxidation will be presented, comparing different model catalysts and highlighting important trends. Finally, an overview of the results and an outlook will complete this thesis.

2 Methodology

As mentioned before, the improvement of catalysts requires a detailed understanding of the effect of different components of the catalyst (metal, oxide) on the presence and reactivity of adsorbates on the surface. Most techniques yield data on the bulk material, but in catalytic studies the most important information is often concerning structural and chemical surface properties, in addition to the surface adsorbates. It is therefore essential to apply special surface sensitive methods. These methods should specifically yield information on

- the elements constituting the surface layers of a catalyst, their abundance and chemical (oxidation) state,
- the surface structure, material crystallinity and particle sizes and
- the type and amount of surface adsorbates and where/how they are bound to the surface.

While the word "catalyst" was first defined as "a substance that speeds up a chemical process without being affected", catalysts taking part in reactions are often strongly influenced by the environment [13]. Active phases can form or disappear, surface structures can change and material deposition and integration in the surface can cause deactivation. Various surface sensitive methods require UHV measurements and can thus only be used to characterize the catalyst before and after reaction to identify persisting changes. It is therefore necessary to also employ techniques that work at higher pressures and can be applied during ongoing reactions.

For this thesis two *in situ* (near) ambient pressure surface sensitive methods have been employed and will be introduced in this chapter.

2.1 Sum Frequency Generation Vibrational Spectroscopy

For decades infrared (IR) spectroscopy has proven to be a powerful tool to investigate the presence, absence and changes of molecules in reaction media or on surfaces. The underlying process of IR spectroscopy is the absorption of an IR photon by a molecule when it is resonant to a vibrational excitation.

The resonance frequency of vibrations primarily depends on the atoms forming the bond e.g. stretching vibrations of a bond between C and H are always located around 2700-3200 wavenumbers, while stretching vibrations of bonds between C and O are located around 1700-2300 wavenumbers. The transition frequency is then influenced by

the bond character (e.g. single and double bond), which is influenced by the composition and structure of the molecule. For example the C O stretching vibration of the CO gas molecule is at lower wavenumbers than the C O stretch vibration of the CO_2 gas molecule due to the different bond strengths between carbon and oxygen. These contributions already allow distinguishing different molecules by IR spectroscopy.

Let us look further into IR spectroscopy on adsorbates, which is the most important application for surface science. When molecules bind to surfaces one can expect that the transition frequencies of the monitored vibrations also change. The surface bond has a great impact on the electronic structure of the molecule. To take again the example of the C-O stretching vibration of a CO molecule, different adsorption sites (like on-top, bridge or hollow adsorption) on a metal (e.g. Pt) surface, can vary over 100 wavenumbers [14]. The peak position for a certain adsorption site is also different for different materials and structures. For example, the on-top CO resonance on Cu is several wavenumbers shifted from the same adsorption site on Pt [15] and the on-top CO resonance on Pt terraces is still 10 wavenumbers shifted from CO on Pt steps [16]. This allows applying IR spectroscopy to follow surface structure changes and surface composition changes. Other minor influences are interactions between the molecules without forming bonds. This can for example be dipole-dipole interactions [17]. With a high surface coverage the dipole-dipole interaction has a higher impact due ordered adsorption structures. Shifts in transition frequencies can thus also be related to changes in surface coverage.

The different effects mentioned above make IR spectroscopy an important technique for surface science. Nevertheless, simple IR spectroscopy has a huge drawback for catalyst research. The acquired spectra do not only show adsorbates but also free gas molecules. If measurd in vacuum, before and after a reaction this is no problem, but to understand the properties of a working catalyst under reaction conditions one must measure at higher pressures. In this case the IR spectra include strong gas phase signals, which need to be subtracted using background measurements or interpreted using simulations to ensure that they do not obscure adsorbate signals. This gives rise to more complex methods that enable surface sensitive measurements. Two methods used in our research group are polarization modulated infrared reflection absorption spectroscopy (PM-IRAS) and sum frequency generation spectroscopy (SFG).

For PM-IRAS, image charges cancel the surface contribution of the IR signal in one polarization (s-pol.), leaving only the gas phase signal. The other polarization (p-pol) yields surface plus gas phase signal and subtraction of both polarization measurements

leaves only the surface contribution [18]. While this method is relatively straight forward, it is limited to metal surfaces, which create the image charges. In comparison SFG needs a much more complex laser system, but it can be used with most flat surfaces, not only metals but also metal oxides, perovskites and so on. In the following sections the concept of SFG as well as some of its properties like the surface sensitivity will be introduced.

2.1.1 Basic derivation of the sum frequency generation effect

Extensive theory on nonlinear optics in general and SFG in particular can be found in books by Boyd [19] and Shen [20], respectively. To explain SFG spectroscopy the interaction of light with matter is essential. Light causes an electric field, which affects the positive and negative charges of atoms and molecules, inducing dipoles. Thus, the equation for the total dipole μ of an atom or molecule is given as

$$\vec{\mu} = \vec{\mu}_0 + \alpha \vec{E} + \beta \vec{E}^2 + \gamma \vec{E}^3 + \cdots. \tag{1}$$

Here μ_0 is the permanent electric dipole, while all other terms are dependent on the electric field. Analogous, for a macroscopic material the polarizability P can be written as

$$\vec{P} = \vec{P}^{(1)} + \vec{P}^{(2)} + \vec{P}^{(3)} + \cdots = \varepsilon_0 \left(\chi^{(1)} \vec{E} + \chi^{(2)} \vec{E}^2 + \chi^{(3)} \vec{E}^3 + \cdots \right). \tag{2}$$

In case of small electric fields all higher order terms are negligible because their coefficients are several orders of magnitude smaller than $\chi^{(1)}$, thus only the linear term $P^{(1)} = \varepsilon_0 \chi^{(1)} \vec{E}$ is important. This term describes polarization oscillating with the electric field $\vec{E}$ and is responsible for "every-day phenomena" like reflection and diffraction.
For large electric fields, however, $\vec{E}^2$is much larger than $\vec{E}$, so the second order term $\vec{P}^{(2)}$ becomes significant.

For the basic derivation the fields of $\vec{P}^{(2)}$ and $\vec{E}$ will now be written as scalars and the influence of the vector character will be discussed later when taking into account the polarization dependence. Thus, the insertion of the scalar electric field of a photon $E = E_0 \, cos\omega t$ is used to change the expression to

$$\begin{aligned} P^{(2)} &= \varepsilon_0 \chi^{(2)} (E_0 \cos(\omega t))^2 \\ &= \varepsilon_0 \chi^{(2)} {E_0}^2 \cos^2(\omega t) \end{aligned} \tag{3}$$

With application of trigonometric addition theorems

$$\cos(x \pm y) = \cos(x)\cos(y) \mp \sin(x)\sin(y)$$

$$\cos(2x) = \cos^2(x) - \sin^2(x) = \cos^2(x) - (1 - \cos^2(x)) = 2\cos^2(x) - 1,$$

we receive the expression

$$P^{(2)} = \varepsilon_0 \chi^{(2)} {E_0}^2 \frac{1}{2} (1 + \cos(2\omega t)). \tag{4}$$

This shows that $P^{(2)}$ contains an oscillating part at the doubled incoming frequency for a single incoming laser beam. This effect is called second harmonic generation (SHG).

For SFG not only one laser beam but two are used. For two incoming beams with different frequencies the electric field is composed of $\vec{E} = E_1 \cos(\omega_1 t) + E_2 \cos(\omega_2 t)$. The resulting second order polarizability is

$$\begin{aligned} P^{(2)} &= \varepsilon_0 \chi^{(2)} (E_1 \cos(\omega_1 t) + E_2 \cos(\omega_2 t))^2 \\ &= \varepsilon_0 \chi^{(2)} ({E_1}^2 \cos^2(\omega_1 t) + {E_2}^2 \cos^2(\omega_2 t) + 2E_1 E_2 \cos(\omega_1 t)\cos(\omega_2 t)) \end{aligned} \tag{5}$$

Again trigonometric addition theorems can be applied to this equation to illustrate the effects arising from the second order interaction. The squared cosines can be arranged like before with

$$2\cos^2(x) = 1 + \cos(2x)$$

as

$${E_1}^2 \cos^2(\omega_1 t) = \frac{1}{2}({E_1}^2 + {E_1}^2 \cos(2\omega_1 t))$$

and

$${E_2}^2 \cos^2(\omega_2 t) = \frac{1}{2}\left({E_2}^2 + {E_2}^2 \cos(2\omega_2 t)\right).$$

For the term combining the frequencies both forms of the cosine addition theorem are added up

$$\cos(x + y) + \cos(x - y) = 2\cos(x)\cos(y)$$

$$2E_1 E_2 \cos(\omega_1 t)\cos(\omega_2 t) = E_1 E_2(\cos(\omega_1 t + \omega_2 t) + \cos(\omega_1 t - \omega_2 t)).$$

The final form of $P^{(2)}$ is therefore

$$\begin{aligned} P^{(2)} = \varepsilon_0 \chi^{(2)} \frac{1}{2} ({E_1}^2 + {E_2}^2 + {E_1}^2 \cos(2\omega_1 t) + {E_2}^2 \cos(2\omega_2 t) \\ + 2E_1 E_2 \cos(\omega_1 t + \omega_2 t) + 2E_1 E_2 \cos(\omega_1 t - \omega_2 t)). \end{aligned} \tag{6}$$

The first part ${E_1}^2 + {E_2}^2$ is a static term and the second part ${E_1}^2 \cos 2\omega_1 t + {E_2}^2 \cos 2\omega_2 t$ is the already discussed second harmonic generation for the single beams. The two remaining terms are oscillations at the sum and difference of the incoming

frequencies. The term to describe sum frequency generation spectroscopy, is therefore the term with oscillation at the sum of the incoming frequencies

$$P^{(2)} = \varepsilon_0 \chi^{(2)} E_1 E_2 \cos(\omega_1 t + \omega_2 t). \tag{7}$$

The time independent form that is commonly used in the literature is then

$$P^{(2)} = \varepsilon_0 \chi^{(2)} E_1 E_2. \tag{8}$$

For general vibrational spectroscopy applications, one of the input frequencies must be in the infra-red range to comply with the vibrational transitions one wants to map, while the other input frequency may be chosen freely, as long as it is non-resonant with the probed material. In most cases a frequency in the visible regime is used as it is easy to adjust and detect. The frequency of the generated photons in is then given as the sum of the scanning infrared and constant visible frequencies

$$\omega_{SF} = \omega_{IR} + \omega_{VIS}. \tag{9}$$

This also locates the SFG light in the visible regime, but the intensity is so low that it is commonly impossible to see the SFG signal with the naked eye.

2.1.2 Quantification of second order susceptibility

We have seen in the last paragraphs that the nonlinear susceptibility $X^{(2)}$ has a large influence on the polarizability $\vec{P}^{(2)}$. We also know that it is zero for centrosymmetric media, while it can be non-zero at interfaces. To get a useful quantification of the non-zero $X^{(2)}$ we have to go back to the molecular description. The microscopic value equivalent to $X^{(2)}$ is the molecular hyperpolarizability $\beta_{\alpha\beta\gamma}$ with α, β, γ for values of the axes a,b,c of the molecular coordinate system.

The macroscopic susceptibility is an orientation average of the molecular hyperpolarizability [20]

$$X^{(2)}_{ijk} = N \sum_{\alpha\beta\gamma} \langle R(\Psi) R(\Theta) R(\Phi) \beta_{\alpha\beta\gamma} \rangle_{ijk} \tag{10}$$

with N as the number of molecular contributions and R denoting rotation matrices for the Euler angles to translate the rotation of the molecular frame to the surface frame.

It has been shown in the literature [21, 22] that the hyperpolarizability can be derived as a relatively simple equation for resonant IR light. The equation for resonance n is

$$\beta_n^{\alpha\beta\gamma} = \frac{-\mu_{n0}^{\gamma}\left(\alpha_{0n}^{ij}\right)}{2\hbar(\omega_n - \omega_{IR} - i\Gamma_n)}. \tag{11}$$

In the denominator the resonance condition is given by $\omega_n - \omega_{IR}$, the difference between resonance frequency and IR frequency, with a dampening term $i\Gamma$. The nominator is a product between the Raman polarizability tensor μ and the IR transition dipole moment α. It is therefore obvious that if a vibration shows either no Raman activity or no IR activity it is not visible in SFG spectroscopy. In addition, the resonance intensities cannot be referenced to IR or Raman spectra due to the double dependency. Still, if the Raman polarizability and the transition dipole moment are known the hyperpolarizability can be directly calculated.

Apart from the hyperpolarizability at resonance there is also a "nonresonant" contribution. This contribution is accompanied by a phase factor, as its origin can be different than for the resonant contribution. Thus the full hyperpolarizability can be written as

$$\beta^{\alpha\beta\gamma} = \beta_{NR}^{\alpha\beta\gamma} e^{i\phi} + \sum_n \beta_n^{\alpha\beta\gamma} = \beta_{NR}^{\alpha\beta\gamma} e^{i\phi} + \sum_n \frac{-\mu_{n0}^{\gamma}\left(\alpha_{0n}^{ij}\right)}{2\hbar(\omega_n - \omega_{IR} - i\Gamma_n)}. \tag{12}$$

For the quantitative conversion of the molecular hyperpolarizability to the second order susceptibility detailed information, like the quantity and disorder of investigated molecules, is required. While this is often not accessible, $\chi^{(2)}$ can be qualitatively written again as the sum of a resonant and non-resonant term.

$$\chi_{ijk}^{(2)} = \chi_{ijkNR}^{(2)} e^{i\phi} + \sum_n \chi_{ijkRes}^{(2)} = \mathrm{A_{NR}} e^{i\phi} + \sum_n \frac{A_n}{\omega_n - \omega_{IR} - i\Gamma_n}. \tag{13}$$

Here A_n is the intensity of the n^{th} resonance with resonance condition $\omega_n - \omega_{IR}$,. This formula is used in general SFG fitting functions.

2.1.3 Important characteristics of SFG for spectroscopy

After this short introduction to the basics of SFG, two important properties will be discussed in this part. First the effect of having a coherent process and second the surface sensitivity that makes this technique so interesting for surface science and catalysis.

Direction of SFG light

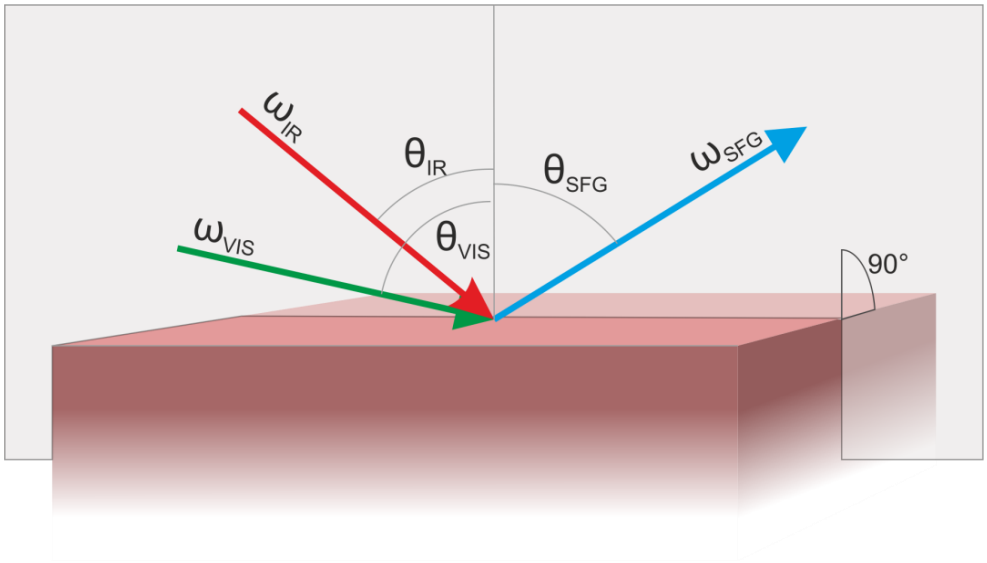

Figure 2.1: Orientation of beams in SFG with plane of incidence perpendicular to surface

While the SFG process uses high power pulsed laser beams to increase the E-field strength, the number of generated SFG photons is still limited. As mentioned above it is generally impossible to detect the SFG beam with the naked eye. Nevertheless, the layout of the experimental setup and especially the placement of the detector can be determined mathematically as the SFG process is a coherent process (due to the oscillation of ordered dipoles). The coherence defines the direction of the generated photons by the parameters of the incoming photons i.e. by the direction and frequency of the incident laser beams. Assuming both laser beams lie in the same plane of incidence (perpendicular to the surface) the SF photons are also emitted in this plane. Only the angle to the surface normal needs to be calculated. This can be achieved through the conservation of momentum. The parts of the wave-vectors parallel to the surface need to fulfill the equation

$$k_{3||} = k_{1||} + k_{2||}. \tag{14}$$

We can derive the parallel part using the respective angles of incidence and (and SFG exit angle) θ_i as

$$k_{i||} = \frac{\omega_i n_i}{c} \sin(\theta_i), \tag{15}$$

where n_i is the frequency dependent refractive index. The final equation is then

$$n_{SF}\omega_{SF} \sin(\theta_{SF}) = n_{IR}\omega_{IR} \sin(\theta_{IR}) + n_{VIS}\omega_{VIS} \sin(\theta_{VIS}). \tag{16}$$

For excitation beams coming from the same direction, as shown in Figure 2.1, the SFG photons are in between the reflected beams. For counter-propagating geometry of the excitation beams the SFG beam would have the same exit direction as the green light due to the higher frequency but at a different exit angle. In this case it is often easier to spatially separate the green and SFG light, which are typically hard to separate optically due to the close frequency relation.

Surface sensitivity

One of the main reasons the complex SFG process is nevertheless popular for IR spectroscopy, is, as mentioned, its interface sensitivity. On its way to the surface, the laser beam passes through gas phase, which adds peaks to conventional IR spectra. Gases are centrosymmetric media, as there is no preferred direction for the orientation of the gas molecules and thus even non-symmetric molecules give the same average over a larger area. In SFG this symmetry inhibits the generation of a gas phase signal. The effect of centrosymmetry on non-linear polarizability will be shown starting from formula (8)

$$P^{(2)} = \varepsilon_0 \chi^{(2)} E_1 E_2.$$

We can assume that in a centrosymmetric medium, if the electric fields E are reversed to $-E$, we also get the reversed polarizability $-P^{(2)}$ due to symmetry operations.

$$-P^{(2)} = \varepsilon_0 \chi^{(2)} (-E_1)(-E_2)$$

With the square the electric field loses its negative sign.

$$-P^{(2)} = \varepsilon_0 \chi^{(2)} E_1 E_2$$

Comparing the two equations shows that for centrosymmetric media the polarizability and its reversed form are the same.

$$-P^{(2)} = \varepsilon_0 \chi^{(2)} E_1 E_2 = P \tag{17}$$

Two values can only be the same with reversed sign if they are zero. This shows that as long as the electric field E is non zero, the susceptibility of centrosymmetric media has to be zero and is therefore not active for SFG. Accordingly, SFG spectroscopy receives no

contributions from gasses and liquids, which are always centrosymmetric, as well as from all centrosymmetric solids. Hence, in a catalytic system the gas phase does not yield a signal and the standard catalyst materials (e.g. noble metals) do not affect the measurement. The only non-centrosymmetric part in this system is the interface between gas phase and solid including adsorbates on the solid surface. Apart from the shown surface sensitivity used for catalytic gas measurements the interface sensitivity allows using this technique to investigate molecules on liquid and solid surfaces [23-25], liquid-liquid interfaces [26] (e.g. orientation of molecules with lipo-/hydrophilic groups at oil-water interfaces), liquid-solid interfaces [27] (e.g. adsorbates in electrochemistry), and even solid-solid interfaces [28].

While most bulk media are not contributing to SFG measurements, there are materials that are intrinsically not centrosymmetric due to their special crystal structures. In fact, out of 32 possible crystal point groups 21 are non-centrosymmetric [29]. Some frequently used materials are

- GaAs (-43m)
- ZnSe (-43m)
- Quartz (32)
- BBO [β-BaB_2O_4] (3m)
- KDP [KH_2PO_4] (2m) or KD*P [KD_2PO_4] (2m)

The respective crystal lattices are denoted in parenthesis. These materials generate a relatively large sum frequency signal and are therefore often used in optical elements (e.g. KDP is a standard SHG crystal). They are also well suited for adjustment of SFG systems.

2.1.4 Polarization dependence

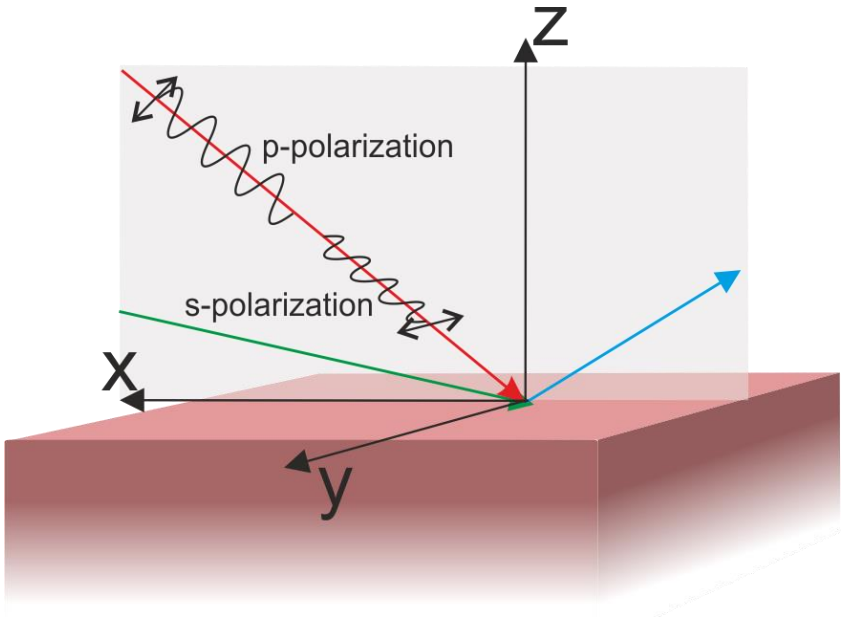

Figure 2.2: SFG beams in coordinate system. p-polarization is parallel to the plane of incidence in the x-z-plane, s-polarization is perpendicular to the plane of incidence.

In the basic explanation of the SF signal for simplicity we omitted the vector nature of the electric field and polarizability, but the orientation of the electric fields (i.e. polarization of the light) has quite some influence. In this section the effect of different polarizations is described.

In the time independent vector notation the polarizability is analogous to formula (8) given as

$$\vec{P}^{(2)} = \varepsilon_0 \chi^{(2)} \vec{E}_1 \, \vec{E}_2. \tag{18}$$

This equation indicates that the susceptibility $X^{(2)}$ is a 3x3x3 tensor with 27 components. The value for a single axis i of $\vec{P}^{(2)}$ is given as

$$P_{iSF} = \varepsilon_0 \sum_j \sum_k \chi_{ijk} E_{j1} E_{k2} \tag{19}$$

with i,j,k ∈ x, y, z for the different axes and 1 and 2 denoting the respective incident beam.

Polarization of light can in general be split into two orthogonal vector fields. These are chosen as p-polarization (from german "parallel"), which lies parallel to the plane of incidence of the laser beam, and s-polarization (from german "senkrecht"), which lies orthogonal to the plane of incidence (compare Figure 2.2). With the plane of incidence lying in the x-z plane of a coordinate system, we can directly see that s-polarization has

only a contribution to E_y and p-polarization only to E_x and E_z. Therefore, the quantities of E for the different directions are given as

$$E_{ix} = \mp\left(E_i^p \cos(\theta_i) - r_p E_i^p \cos(\theta_i)\right) = \mp \cos(\theta_i)\,(1 - r_p) E_i^p \tag{20}$$

$$E_{iy} = E_i^s + r_s E_i^s = (1 + r_s) E_i^s \tag{21}$$

$$E_{iz} = \left(E_i^p \sin(\theta_i) + r_p E_i^p \sin(\theta_i)\right) = \sin(\theta_i)\left(1 + r_p\right) E_i^p, \tag{22}$$

with i standing for the different beams in the SFG process and r_p and r_s are the reflectivity factors for the p- and s-polarized light. The different signs of E_x are for co- and counter-propagating incident beams.

Polarization dependent measurements can therefore be used to calculate single elements of the tensor matrix or calculate rough estimations of the molecular tilt angle. Figure 2.3 shows three simplified examples of s-polarized incident beams and their influence on different molecule configurations. This beam would only cause excitation in y direction as the electric field only oscillates in y direction. If a molecular bond is parallel to the surface normal, stretching vibrations are also parallel to the surface normal (in z direction). For an electric field in y direction it is therefore not possible to excite the stretching vibration and no resonance would be observed in the SFG spectrum. If the molecular bond is tilted with respect to the surface normal a contribution of the s polarization can drive an oscillation in the direction of the stretching vibration. The electric field strength in the direction of the molecular bond can be obtained by using a vector base in the y-z plane with one vector in the direction of the molecular bond and the other one perpendicular. In this case a corresponding peak appears in the SFG spectrum. The third panel in Figure 2.3 concerns a molecule on a smaller facet that is tilted with respect to the macroscopic surface normal (e.g. observed on a rough film). In this case even a molecule adsorbed perpendicular to the surface contributes to the SFG signal. As mentioned before, this is a simplified picture and the calculation of intensity ratios is quite complex. Detailed analysis for polarization dependent SFG and intensity correlation to the tilt angle can be found in the literature [30-32]. Still this simple explanation allows us to use polarization dependent SFG as a qualitative indicator for the roughness of our samples as CO bound perpendicular to the surface of small tilted facets is not parallel to the macroscopic surface normal.

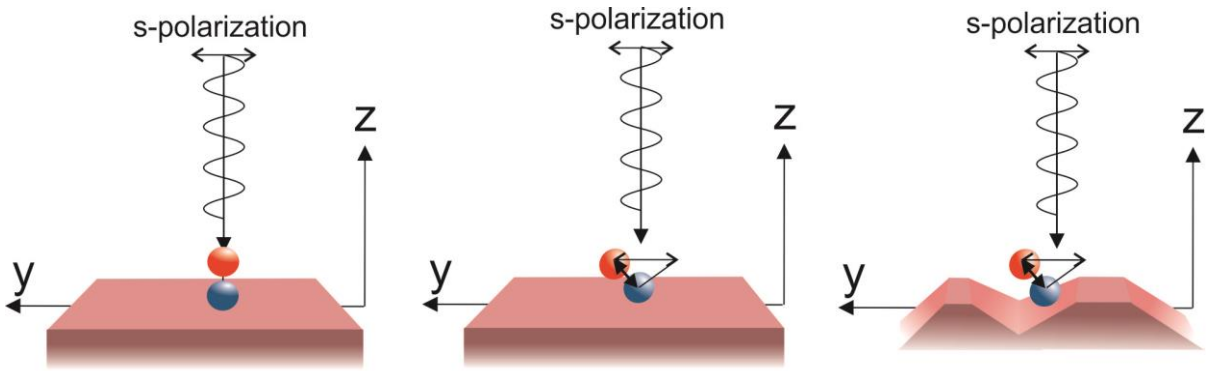

Figure 2.3: Scheme of s-polarized beams and their interaction with molecules. Left: a molecular bond perpendicular to the surface and parallel to the surface normal (z direction) is perpendicular to the electric field oscillations, i.e. no excitation for SFG signal. Mid: a molecule tilted on the surface is not parallel to the surface normal and can be excited by s-polarized light. Right: a molecule perpendicular to the surface but with a surface tilted to the plane of incidence (x-z direction) contributes to the SFG signal.

2.2 Near Ambient Pressure X-ray Photoelectron Spectroscopy

Infrared reflection adsorption spectroscopy (IRAS) is a very important surface science technique and in most cases it provides indirect information by using probe molecules (e.g. CO) and adsorbate changes. A method for direct surface investigation is x-ray photoelectron spectroscopy (XPS). It allows not only identification of chemical elements on the surface but also their oxidation state. Therefore, it was originally named electron spectroscopy for chemical analysis (ESCA) by Kai Siegbahn, who was awarded the Nobel Prize in 1981 for advances of this technique [33]. Standard XPS is limited to very low gas pressures (i.e. ultra-high vacuum, UHV) but specially designed analyzers and chambers allow measurements at several millibars pressure.

2.2.1 General principle of XPS

The underlying mechanism of XPS is a photoemission process, when an electron is excited by an X-ray photon. When the photon energy is high enough to ionize the atom the electron is no longer localized at the atom and travels through the sample. For its detection it is necessary that electron leaves the sample and reaches to the analyzer. The kinetic energy of the photoelectrons depends on the binding energy E_B of the atom core level (which is specific for each element and its electronic shells) and the X-ray photon energy $h\nu$. When the electron leaves the sample, the kinetic energy is also reduced by the surface work function WF. Thus electrons reaching the vacuum have a kinetic energy of

$$E_{kin} = h\nu - E_B - \mathrm{WF}_{Sample}. \tag{23}$$

This basic process is also shown schematically in Figure 2.4.

For spectroscopy the electrons with a certain kinetic energy are measured with an energy selective analyzer. The analyzer has its own work function, adding to the kinetic energy of the electrons. When the analyzer and sample are electronically connected the contact potential is $\Phi = \mathrm{WF}_{Sample} - \mathrm{WF}_{Analyzer}$. This changes the equation for the measured kinetic energy to

$$E_{kin@Analyzer} = h\nu - E_B - \mathrm{WF}_{Sample} + \Phi = h\nu - E_B - \mathrm{WF}_{Analyzer}. \tag{24}$$

This equation shows that the work function of the sample is irrelevant for measurements as it is compensated by the contact potential between analyzer and sample.

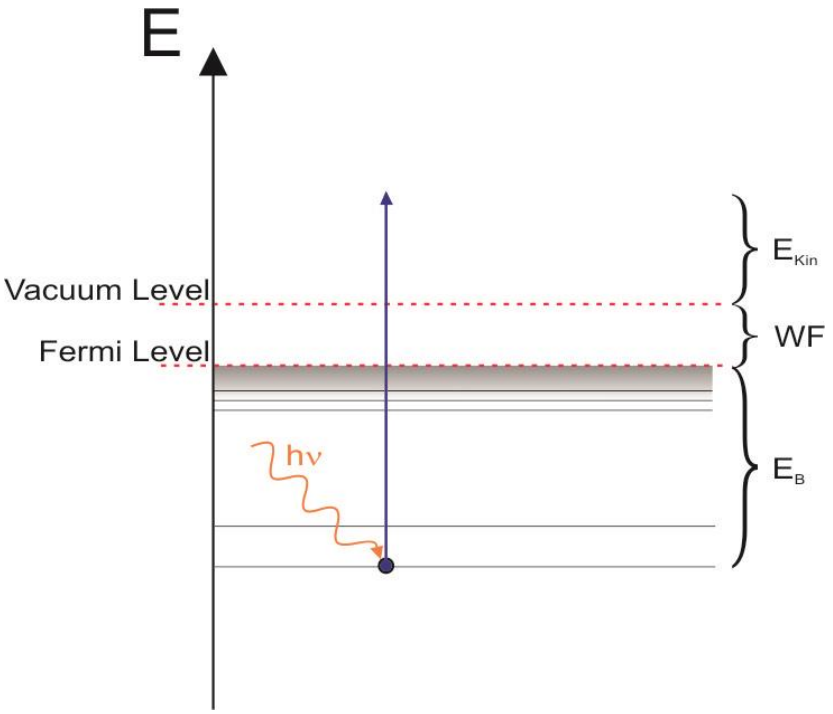

Figure 2.4: Energy diagram of the XPS process. An X-ray photon creates a photo electron from a core level of a surface atom. The kinetic energy E_{kin} of this electron depends on the binding energy EB and the sample work function WF.

Although the work function of the analyzer is unknown, the kinetic energy of the XPS spectra can be calibrated. For metallic samples this is easily done by measuring the Fermi edge of a spectrum. Electrons from the Fermi edge can be assumed to have a kinetic energy equal to the X-ray photon energy hν (since E_B is zero, there is no reduction from binding energy). Thus, the electrons with highest E_{kin} in the XPS spectrum (assumed to be the Fermi edge electrons) are set to a kinetic energy equal to hν, shifting the whole XPS spectrum in energy. The calibrated values correspond to the kinetic energy of electrons before leaving the sample (i.e. before influence of the sample work function) as $E_{kin-calibrated} = h\nu - E_B$. For samples that do not exhibit a well-defined fermi edge it is also possible to calibrate the energy using a known peak position, like the C 1s of graphitic carbon.

For XPS analysis counts per second (CPS) are plotted versus E_B. In this way of plotting, peak fitting can be performed for data analysis giving information on peak shifts (chemical nature of the element), peak areas (quantification), components and so on. An exemplary survey spectrum of a Pt/ZrO_2 sample is shown in Figure 2.5. The spectrum consists of narrow peaks from the core level electrons of different elements. An increasing background arises from electrons that are inelastically scattered and thereby lose energy before leaving the sample. Other possible features not observed in this

survey spectrum are (broad) Auger peaks [34]. The kinetic energy of Auger electrons is only defined by the Auger process and independent from the X-ray excitation energy. Then, when plotting E_B vs. intensity, these peaks move in the spectrum when changing the excitation energy. This effect can be utilized to differentiate Auger from photoelectron peaks and to prevent Auger peaks from obscuring relevant XPS features.

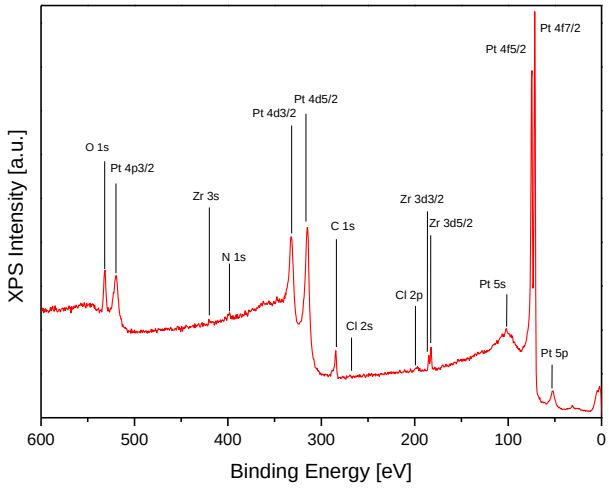

Figure 2.5:Example of an XPS survey spectrum of a Pt/ZrO_2 model catalyst. Most prominent peaks are from different Pt core levels (4p, 4d, 4f, 5s and 5p) as well as from C 1s, O 1s and Zr 3d.

2.2.2 Information gain and Surface sensitivity

The position of XPS peaks in the spectrum mainly depends on the elements monitored. It is possible that features of different elements overlap due to similar electron binding energies but this is mostly limited to the emission from one electron shell. Therefore, different material combinations still have characteristic peaks that can be used to clearly identify the surface composition of a sample. In the example survey in Figure 2.5 the peaks for platinum, zirconium and oxygen (from zirconia) are well separated and some surface contaminants can be identified (especially carbon). XPS is therefore suitable to monitor surface composition and contamination.

Apart from the general E_B difference for different elements (which is in many cases relatively large), the core levels are also influenced by the surrounding atoms. Different molecular bonding and connected oxidation states cause a shift that is also visible in XPS spectra. As an example Figure 2.6 shows a C1s spectrum with three different components that form the overall envelope. All three shown features arise from carbon core levels, but due to the different bonds of carbon atoms to other surrounding atoms they are split into three peaks. XPS is therefore suitable to identify various important

surface science characteristics like oxidation states of different atoms in a sample, molecular bindings and surface contaminations. This is due to the differences in the local electronic structure of different bonding configurations. A higher electron concentration (lower oxidation state) can cause increased screening of the positively charged atom core, decreasing the binding energy, while higher oxidation states generally increase the binding energy of the electrons.

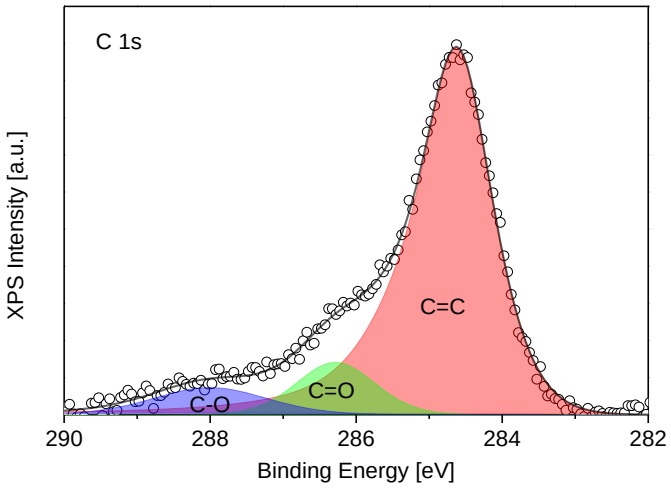

Figure 2.6: Example of a C 1s spectrum with three different contributions due to differently bound carbon.

To generate an XPS spectrum the photoelectrons have to fulfill several requirements. While they are still inside the sample they can collide elastically or inelastically with other compound atoms. Inelastic collisions will cause the electrons to lose energy or even prevent them from leaving the sample at all. In both cases the electrons are lost for the XPS spectrum, as inelastically scattered electrons that reach the detector only contribute to the background. The probability of an electron from depth d to reach the surface without energy loss depends on the inelastic mean free path λ exponentially with $e^{-d/\lambda}$. The inelastic mean free path of electrons in solids is in general very short and mainly depending on their kinetic energy [35]. This means that electrons from the surface have a much higher chance to leave the sample than electrons from lower layers and electrons with more kinetic energy also have a higher chance to reach the surface than electrons with low kinetic energy do.

The implications for XPS measurements are that the majority of the signal contribution comes from the surface layers and that with higher X-ray photon energies the proing depth increases. The technique is therefore inherently more sensitive to the surface layers but can be tuned by selecting excitation energies close to the binding energy of investigated peaks (probing only top layers) or to much higher excitation energies

(probing also lower layers). For laboratory setups the X-ray sources typically comprise two possible photon energies, which are high (above 1k eV) to allow measurements over a large range of binding energies. Two different energies are required to handle Auger peaks that may obscure signals for one of the excitation energies. The constant excitation energies also imply that laboratory XPS sources often probe deeper into the sample than the desired surface layers and have different signal depths for different elements. This is different at synchrotron facilities, where not only the beam brilliance (i.e. number of photons with the same direction and wavelength per area and time) is much higher, but photon energies can be chosen over a wide range. For example, for measuring peaks at binding energies of 80 eV and 530 eV, the respective excitation energies of 140 eV and 590 eV could be used to achieve similar information depths. Changing the excitation energy for measurements of a single peak (e.g. successive increase of excitation energy by 150 eV) yields depth profiles, because electrons from lower layers have an increased probability to leave the sample. In laboratory measurements depth profiling is possible be changing the angle between the surface normal and analyzer. The higher the angle, the longer is the path through the sample for electrons from deeper layers. Thus, for high angles the measurements are very surface sensitive even with high X-ray photon energies, but the overall intensity of a spectrum is low.

2.2.3 Near ambient pressure XPS

Inelastic collisions of photoelectrons within the solid sample may prevent their detection. However, even after leaving the sample they can still have inelastic collisions with gas phase molecules. This is especially problematic as the electron path from surface to analyzer is much longer than the path through the solid. To encounter this problem samples are located in UHV chambers to minimize gas phase collisions and ensure that a high number of photoelectrons reaches the analyzer without losing their energy. Standard XPS setups are therefore not suitable for catalytic in situ measurements. They can be used to compare surfaces before and after exposure to different gas phases or before and after reactions. Still, in many cases there may be phenomena occurring during reaction, which cannot be observed with ex situ measurements [18, 36].

To facilitate XPS measurements in gas phase, special setups have been designed with differential pumping stages towards the analyzer. In these setups higher gas pressures can be realized, due to special geometrical arrangement of x-rays, sample and analyzer.

Right in front of the sample is a nozzle with a very small diameter that allows electrons to fly towards the analyzer. Inside the nozzle, the first pumping stage drastically lowers the surrounding pressure (at least 10^{-4} mbar) and additional pumping stages further lower the pressure down to 10^{-8} or 10^{-9} mbar to ensure that a multitude of photoelectrons reaches the detector and to prevent damage to the detector.

With such a setup it is possible to perform XPS measurements in reaction gas mixtures up to catalytically relevant pressures [37, 38]. It is therefore called "Near Ambient", as significant spectra can in some cases be acquired up to a few tens of millibars.

One characteristic of NAP XPS spectra are gas phase peaks. As mentioned before the nozzle of the analyzer is very close to the sample surface to minimize the pathway of photoelectrons through the high pressure region. Nevertheless, in the remaining space in-between sample and nozzle it is possible that the X-ray photons excite photoelectrons from the gas phase molecules. They cause additional peaks in the XPS spectrum. Gas phase peaks are in general located at higher binding energies than those from surfaces and are very narrow due to the more discrete electronic structure of atoms and molecules in comparison to the band structures in solids. In addition, the photoelectrons from the gas phase are not retarded by the surface work function. Shifts of gas phase peaks in XPS spectra can thus be directly correlated to changes in the surface work function of the measured samples.

In summary, near ambient pressure XPS can be used to investigated surfaces and adsorbates under reaction conditions up to several millibars with a specially designed setup. Additionally, gas phase peaks can be observed, which may be a valuable addition for studying the evolution of gas phase compositions or detecting reaction intermediates. Nevertheless, the NAP-XPS setups are complex and expensive and are therefore mostly found at synchrotron facilities where they gain additional value from the high X-ray brilliance.

3 Model catalysts: Concept & Preparation

3.1 Introduction to Model Catalysts in Heterogeneous Catalysis

The aim of surface science studies in catalysis is to investigate the active catalyst surface, to characterize the active sites and to monitor reaction processes. This may yield information on the nature of active surface compositions or structures, about reaction intermediates and catalyst deactivation. The gained information provides deep understanding of the processes taking place and can be used to create new catalysts or improve existing ones for industrial use.

Surface science methods often impose special requirements on investigated materials.

- Often the samples have to be conducting, e.g. for scanning tunneling microscopy (STM). Other samples cannot be used or special equipment would be required, like an electron flood gun for x-ray photoelectron spectroscopy (XPS) to discharge the surface.
- Surfaces need to be well defined to make a connection between results and surface structures. For example adsorption sites with different coordination numbers influence peak positions, but there are also other effects like influence of supports or alloying on the peak position.
- Samples also need a very smooth surface for many techniques. For example STM or atomic force microscopy (AFM) cannot be used to investigate pores and spectroscopic methods working in reflectance like SFG need focused light for detection.

Industrially used catalysts do not meet these requirements, as they are designed to have large surface areas and therefore high porosity and surface roughness. Nanoparticles are often deposited on support materials to enhance the catalytic activity, which may be oxides and therefore insulating. To conquer this challenge model catalysts are used for surface science investigations.

3.1.1 Examples of model catalysts

In early surface science studies, single crystals were mainly used as models. Single crystals have a defined structure, a well know composition and can be polished to achieve very low surface roughness. They can be prepared for measurements by Ar sputtering to remove contaminations from the surface and annealing (heating to high

temperatures) to smooth microscopic roughness afterwards. The main variation in single crystal studies (apart from using different elements) is choosing different surface terminations of the crystals. Choosing for example a Pt(335) instead of a Pt(111) single crystal allows observing the difference between step and terrace interaction for a Pt surface [39, 40]. Overall, single crystals can be used with most surface science methods and yield results that can often be linked well to the surface structures and compositions. Nevertheless, the well-defined surface is also a great disadvantage for drawing relevant conclusions as it is very different from real catalysts, where complex structures and material interfaces have a huge impact.

To add the influence of catalyst/support interfaces to the single crystal studies inverse model catalysts can be designed [41, 42]. Instead of the usual metal on support system, a single crystal of the metal material is used (as support) and small amounts of the oxide are deposited on top. This can either be achieved by evaporating the oxide onto the surface, or by using an alloy single crystal [43]. In the latter case one metal of the alloy may form an oxide layer or particles on the crystal surface upon oxidation. These inverse models feature the properties of well-defined catalyst materials (similar to single crystals) but add support interfaces to the reaction process.

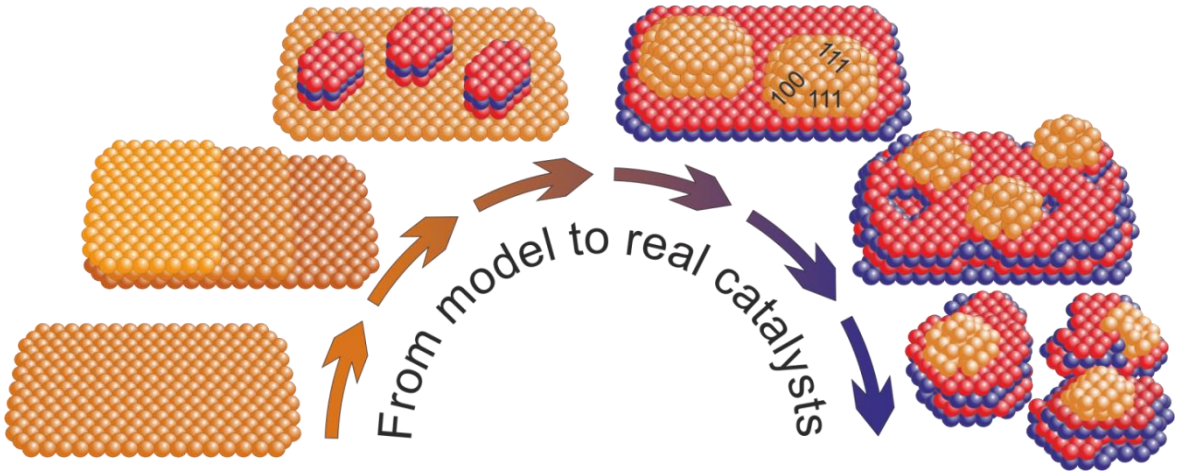

Figure 3.1: Evolution of model catalysts from single crystals to increasing complexity.

The next step in model catalyst complexity is using a well-defined support (e.g. single crystal or thin film) with exact metal structures on top. These can be specially prepared crystalline nanoparticles or size-selected clusters deposited on the surface. In this case the composition is already similar to industrial catalysts, while most features are still well defined. Still the macroscopic roughness is very small and suitable for most surface science techniques. To increase the complexity further, the metal particles on top may be less defined polycrystals with grain boundaries and random surface terminations.

Apart from the described catalyst models, there are many more possibilities for certain measurements, e.g. polycrystalline foils, self-assembled monolayer surfaces etc.

3.2 Atomic Layer Deposition: Theory and Catalyst Production

One method that has gained importance in catalyst production over the last few years is atomic layer deposition (ALD). As its name indicates this is a method where atomic layers are formed, whereby thickness and stoichiometry can be controlled. ALD is a form of chemical vapor deposition (CVD) using volatile precursors and applied especially in the production of electronic devices. In comparison to standard CVD, where all required precursors are in the gas atmosphere at the same time, the ALD process consists of separate dosing of the precursors with intermediate evacuation or purging of the gas phase with inert gas.

The ALD process consists of four main steps as shown in Figure 3.2 and sometimes of an initializing step at the beginning to activate the surface. In the first step one precursor (in general a metal core complex) is dosed into the ALD chamber. It reacts with the surface, removing several ligands from the metal core, and forming a new layer. The process is self-limiting, as the reaction at the surface can only occur as long as there are active end groups. In the second step the gas phase with remaining precursor and reaction products is purged/evacuated. In the third step the second precursor (in most cases water or oxygen) is dosed into the ALD chamber. It removes the remaining ligands from the metal complexes at the surface and adds a new layer (in most cases chemisorbed OH or O). The fourth step is purging/evacuating after the second precursor to ensure that not more than one layer is formed per cycle. These steps are repeated until the desired thickness of the film is achieved.

The general ALD procedure is straight forward, but there are several things to consider:

Pace of the ALD process: The alternating precursor use and purge phase make this technique quite slow compared to other CVD applications. Thus it is important to know the dependence of layer growth to dosing time and the inertness of the precursor and reaction products in the purging step to minimize the cycle duration.

Temperature control: The temperature of the precursor, the ALD chamber walls and the sample are crucial. The precursor temperature is responsible for the amount of precursor available in the dosing step, while the chamber temperature needs to be higher than the precursor temperature to keep it from sticking and low enough to

prevent the chemical deposition/decomposition. The temperature of the sample needs to be high enough for the reaction to occur but low enough to prevent thermal decomposition of the precursor on the surface.

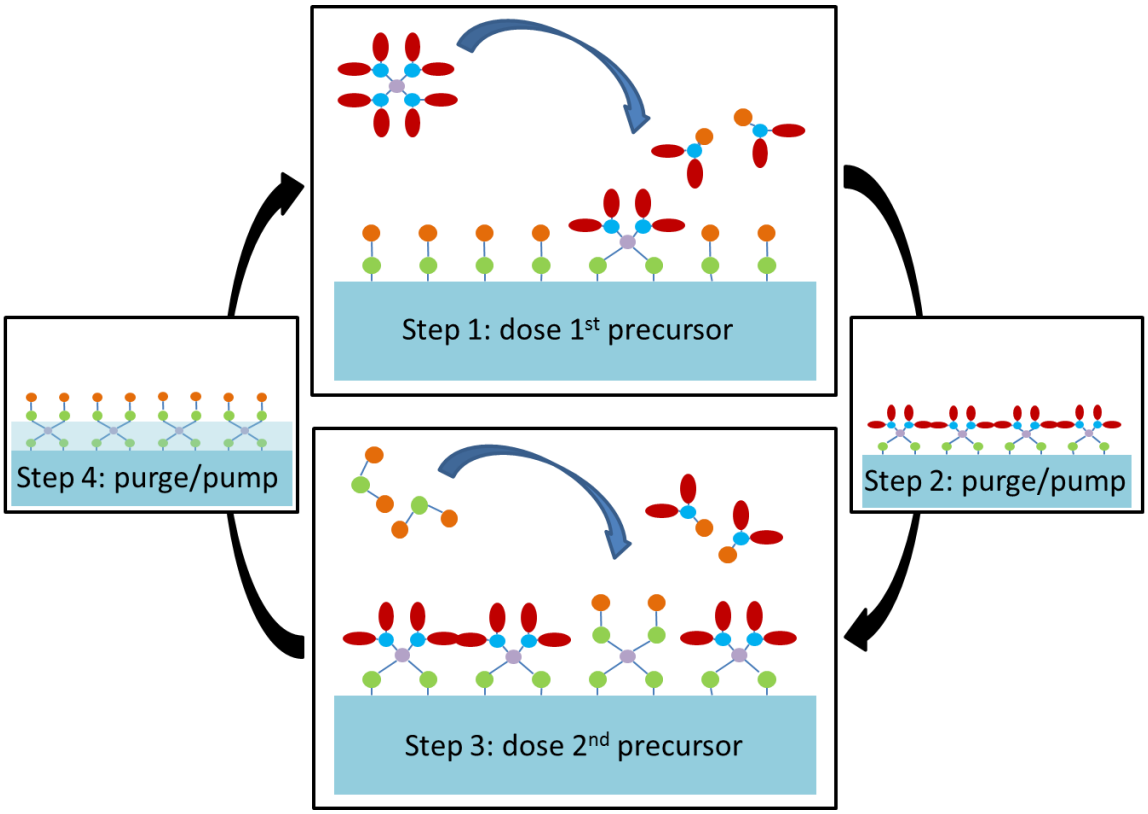

Figure 3.2: ALD process in 4 steps. In step 1 the first precursor (metal complex) is dosed. The complexes react with the active surface groups until the surface is covered with a new layer. The 2nd step is a purging or pumping of the gas environment to hinder gas phase reactions. In the 3rd step the other precursor is dosed, removing the rest of the ligands remaining from the metal complex and forming a new layer with active end groups again. In step 4 the gas phase is again purged/pumped to avoid gas phase reactions and disturbances in the self-limitation of the process.

Stoichiometry of the sample: One of the advantages of ALD is the direct control of stoichiometry of the deposited material, e.g. in the deposition of oxides. This is possible by exchanging the metal complex precursors with suitable complexes featuring a different metal core every x cycles depending on the desired composition. In this case it is very important to know the deposition rate per cycle for the different precursors.

Wetting: Another important point, which is connected with deposition rate and sample temperature, is the so called "nucleation delay". In theory an ALD process forms mostly uniform layers on the surface. Nevertheless, when starting the deposition on a different material the bond to the surface is very weak, causing the deposited material to

aggregate to nanoparticles/islands instead of layers from the beginning. This can, for example, be observed when depositing metal films onto oxide surfaces [44]. It has been shown for Pt on oxides that up to 20 deposition cycles there was no continuous surface layer, while after a certain threshold the surface smoothed out and a uniform film was obtained at higher numbers of deposition cycles. This effect can be influenced by surface pretreatment of the base material prior to ALD. While this nucleation is a great problem for many applications of ALD, especially in the manufacturing of electronic components, it is an interesting tool for the production of catalysts, where controlled growth of nanoparticles is desired.

The very uniform surfaces that can be obtained by ALD (especially when using a single crystal as base material) fit the afore mentioned smoothness requirements of model catalysts in surface science, while the nucleation in several material combinations can be used to create well dispersed nanoparticles of comparable size. This makes ALD a perfect method for model catalyst creation. The final model catalysts designed herein consised of a silicon (100) wafer as base material, because the wafer has a well-defined, very smooth surface and is easily available due to its use in electronics. On the silicon wafer, zirconia (ZrO_2) was deposited via ALD. The precursors used for the zirconia were tetrakisdimethylamido-zirconium ($Zr(NMe_2)_4$, see Figure 3.3 left) for ALD step 1 and water for ALD step 3. The reaction process starts with an OH terminated surface. In the first step two of ligands are removed from the metal complex by reaction with hydrogen of the OH groups, while the zirconium precursor binds to oxygen and forms a layer (compare Figure 3.2). In the third step, the remaining two ligands are removed by reaction with water and the surface becomes OH terminated again.

$$2(OH)_{ads} + Zr(N(CH_3)_2)_4(g) \rightarrow O_{2surface}\text{-}Zr(N(CH_3)_2)_2 + 2\,HN(CH_3)_2(g)$$

$$O_{2surface}Zr(N(CH_3)_2)_2 + 2\,H_2O(g) \rightarrow O_2Zr_{surface}\text{-}2(OH)_{ads} + 2\,HN(CH_3)_2(g)$$

The precursor temperature was 75 °C to provide a saturating dose and the sample temperature was 200 °C, as deposition below 180 °C causes impurities [45]. The precursor pulse time for step 1 was 0.15 s, the pump time in step 2 was 10 s. For the water in step 3 the pulse time was 0.025 s with a pumping duration in step 4 of 10 s again. With a deposition rate of 0.105 nm per cycle, a ZrO_2 film of 42 nm was deposited with 400 cycles.

On this 42 nm zirconia film Pt was also deposited by ALD. The precursor for this deposition was methylcyclopentadienyltrimethyl-platinum ($MeCpPtMe_3$, see Figure 3.3

right) as first reactant and oxygen was the second reactant. The corresponding reaction is [46]

$$3O_{ads} + 2\,CH_3C_5H_4Pt(CH_3)_3(g) \rightarrow 2(CH_3C_5H_4Pt(CH_3)_2)_{ads} + CO_2(g) + CH_4(g) + H_2O(g)$$

$$2(CH_3C_5H_4Pt(CH_3)_2)_{ads} + 24\ O_2(g) \rightarrow 2Pt_{surface}\text{-}3O_{ads} + 16\,CO_2(g) + 13\,H_2O(g)$$

for the first and third step respectively. The precursor temperature was 70 °C with a sample temperature of 270 °C. With changes to step 3 lower sample temperatures could be used but special equipment would be required [47]. The pulse times are higher compared to the zirconia deposition with 1 s for step 1 with the Pt precursor and 2 s for step 3 but the pumping time in both pumping steps was only 3 s. The number of deposition cycles was varied for different samples to create a "bridge" from Pt nanoparticles to bulk surfaces. The selected numbers of deposition cycles were 5, 10, 50, 125, 250 and 750. Corresponding TEM images will be shown in the next section, except for the 750 cycle sample. As will be shown later, the 250 cycles already feature a closed thick film. Furthermore, using deposition rates from literature [48] we can estimate the film thickness of the 250 cycle films being 10 nm and the 750 cycle film being 30 nm. Below 250 ALD cycles, a (homogeneous) thickness calculation by deposition rate is meaningless, since to the island nucleation density is unknown.

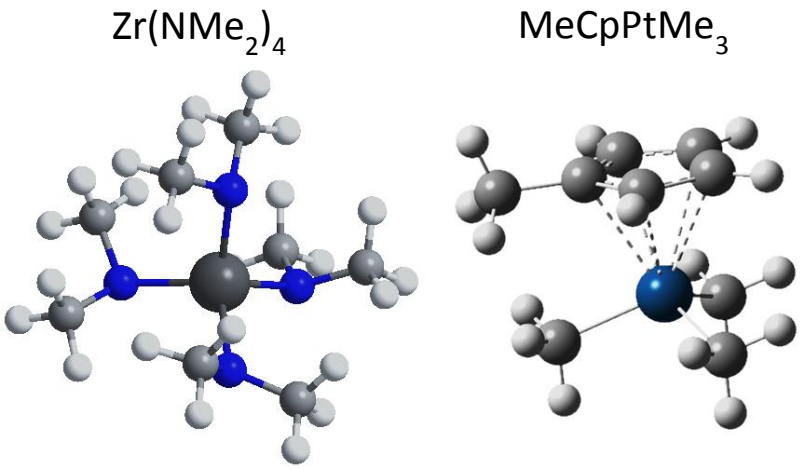

Figure 3.3: Metal precursors for the ZrO_2 and Pt deposition. Left: Tetrakis-dimethyl-amido-zirconium. Right: Methylcypclopentienyl-trimethyl-platinum

3.3 Characterization of ALD Model Catalysts

After designing model catalysts by ALD, a detailed characterization is needed prior the surface science experiments. This is necessary to understand the correlations between surface structure and observed catalytic properties. In the following results of transmission electron microscopy (TEM), x-ray diffraction (XRD) and x-ray photoelectron spectroscopy (XPS) measurements are shown. They characterize the amount and structure of Pt but also yield information on the underlying support material.

3.3.1 X-ray diffraction

For a full characterization of the model system, especially concerning the support, bulk techniques need to be applied. X-ray diffraction provides information about the crystallinity of materials. For our system, we use it to determine crystal lattice structures, lattice constants, preferred lattice directions and estimated crystallite sizes.

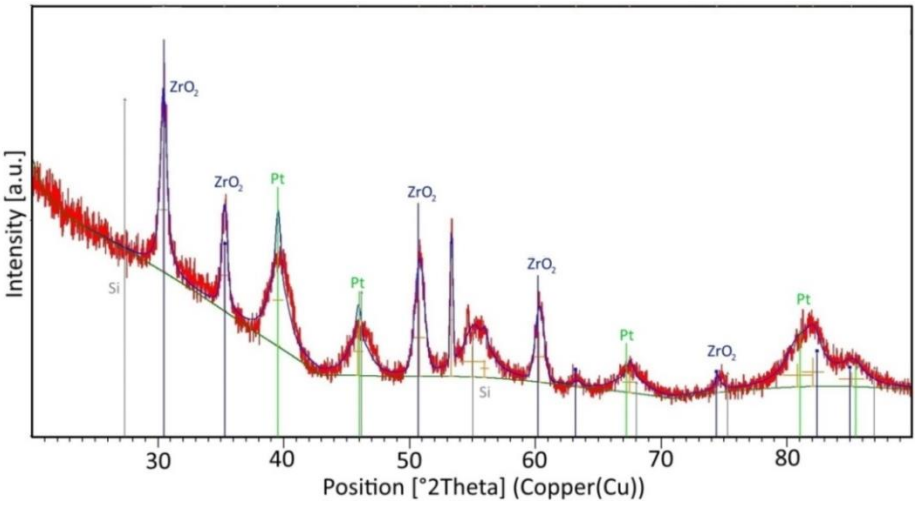

Figure 3.4: XRD pattern of the model catalyst with 50 deposition cycles. Peaks corresponding to cubic ($Fm\bar{3}m$) ZrO_2 are marked with blue lines; peaks corresponding to cubic ($Fm\bar{3}m$) Pt are marked with green lines.

Figure 3.4 and Figure 3.5 show the XRD data of two selected samples with 50 and 250 deposition cycles of Pt, respectively (ZrO_2 was, as stated before, deposited over 400 ALD cycles). The first interesting characteristic is the existence of a large number of peaks that appear on the same positions in both cases but with differing intensity. The spectrum gives evidence on the polycrystallinity of the sample as all powder diffraction peaks are visible. For single crystals (or crystallites with preferential growth direction) only selected peaks lie within the one measurement plane and only sample plane

rotation could bring out all peaks. For the polycrystalline spectra the peaks could be assigned to crystal structures of ZrO_2 and Pt using XRD libraries.

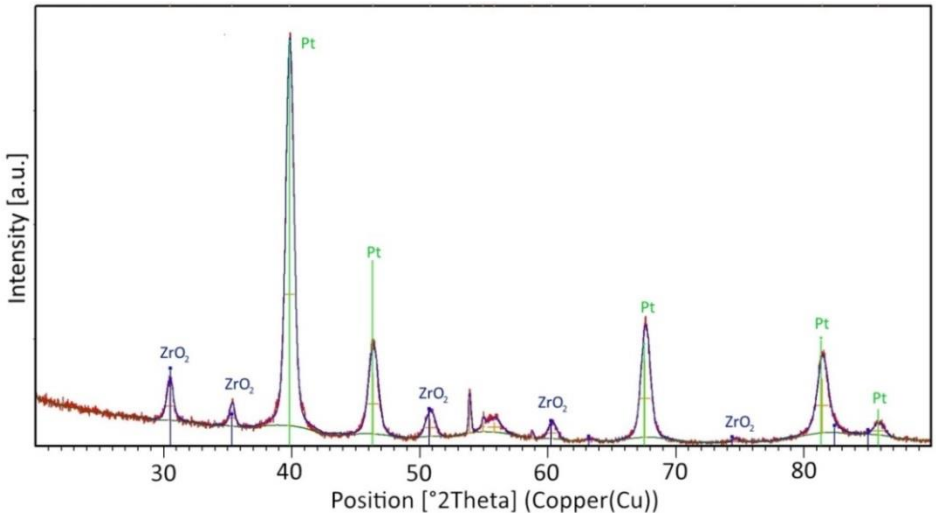

Figure 3.5: XRD pattern for the model catalyst with 250 deposition cycles. Peaks corresponding to cubic (Fm3̄m) ZrO_2 are marked with blue lines; peaks corresponding to cubic (Fm3̄m) Pt are marked with green lines.

Table 3.1 shows the best fitting data set for the zirconia support peaks from the XRD database. It corresponds to a cubic lattice with space group Fm3̄m and a lattice spacing of a=b=c=5.11 Å [49]. Table 3.2 shows the best fitting data set for Pt, which is also in both cases a cubic Fm3̄m lattice with spacing of a=b=c= 3.92 Å [50]. Furthermore, the large lattice mismatch does not facilitate a preferential growth of the Pt crystals on the zirconia.

Table 3.1: Best fitting dataset for the ZrO_2 peaks

h	k	l	d [Å]	2θ [°]	I [%]
1	1	1	2,95026	30,270	100,0
2	0	0	2,55500	35,094	19,4
2	2	0	1,80666	50,474	51,5
3	1	1	1,54072	59,995	31,5
2	2	2	1,47513	62,959	4,5

Table 3.2: Best fitting dataset for the Pt peaks

h	k	l	d [Å]	2θ [°]	I [%]
1	1	1	2,26500	39,764	100,0
2	0	0	1,96160	46,244	53,0
2	2	0	1,38730	67,456	31,0
3	1	1	1,18260	81,289	33,0
2	2	2	1,13250	85,715	12,0

As expected, the intensity of the platinum peaks on the 250 cycle film was much higher than for the 50 cycle film, due to its more numerous and larger Pt crystal grains. The zirconia signal is comparable in intensity for both samples. It is also important to point out that the standard peak fits are not matching the peak shape of the Pt features on the 50 cycle film. They are very wide, hinting to additional peak broadening (e.g. from disorder). Accordingly, the peak width values (full width at half maximum, FWHM) denoted in Table 3.3 for the 50 cycle ALD Pt film are too small as the FWHM is taken at a higher position than the actual peak shape requires. Another interesting observation is the large peak height of the [111] peak compared to the [200] peak for the 250 cycle film. It indicates that, while there is no single crystalline character of the sample, it seems there is still a slightly preferred lattice direction for the Pt crystallites.

The XRD measurements can also be used to calculate estimates of the lower size boundary of Pt crystallites. For this estimate the Scherrer equation [51] (Formula (26)) was used with L denoting the lower boundary of the grain size.

$$L = \frac{K \cdot \lambda}{\sin(\Theta) \cdot \Delta(2\Theta)} \tag{25}$$

K denotes the Scherrer factor, which is determined empirically to be roughly 0.9. λ is the wavelength of the x-ray source, in this case copper kα = 1.54 Å. Θ is the position of the respective peaks and Δ(2Θ) is their full-width-half-maximum in radians. The measured quantities and calculated L values are denoted in Table 3.3.

The mean of the calculated crystal grain sizes was 13±3 nm for the ZrO_2 substrate of the 250 cycle sample and 12.5±2.4 nm for the 50 cycle sample. As expected the values are comparable as the ALD process of Pt should not have a great influence on the ZrO_2 film, nevertheless L_{ZrO2} is slightly lower for the 50 Pt cycle sample. One has to keep in mind that the Scherrer formula is only a size boundary estimate. For Pt crystallites, the mean L value was 11.0±0.9 nm for the 250 cycle Pt film and 9.8±1.4 nm for the 50 cycle Pt film. It is surprising that the values are again very close although the amount of Pt differs by a factor of 5. On one hand this may be an indicator that the Pt film keeps its granular structure even at higher thickness. On the other hand one has to keep in mind that the used FWHM values for the 50 cycle film are smaller than the actual values due to the peak fit mismatch with the actual peak shape. As the FWHM is in the denominator, a larger FWHM would lead to a lower value of the size boundary.

Table 3.3: XRD peak positions, peak width, peak area and calculated grain size by using the Scherrer formula for the measurements shown in Figure 3.4 and Figure 3.5.

250 cycle ALD	2Θ[°]	Δ(2Θ)[°]	Area[a.u.]	Calc. grain size[nm]
ZrO_2	30,4702	0,5968	189,01	13.8
ZrO_2	35,3251	0,4773	78,41	17.5
Pt	39,8160	0,7321	2034,06	11.5
Pt	46,3512	0,8689	544,07	9.9
ZrO_2	50,8028	0,8455	137,40	10.4
ZrO_2	60,3038	0,7873	82,73	11.7
Pt	67,5916	0,8219	656,96	11.6
50 cycle ALD	2Θ[°]	Δ(2Θ)[°]	Area[a.u.]	Calc. grain size[nm]
ZrO_2	30.4168	0,6304	273,16	13.1
ZrO_2	35,2644	0,5426	114,83	15.4
Pt	39,5174	0,8056	355,45	10.5
Pt	45,9070	0,8149	184,89	10.6
ZrO_2	50,7618	0,8868	175,03	9.9
ZrO_2	60,2857	0,8022	98,71	11.4
Pt	67,4814	1,1600	117,69	8.2

3.3.2 Transmission electron microscopy (TEM)

As a microscopic technique, TEM is a suitable method to determine the film character of Pt on the surface. TEM and scanning electron microscopy (SEM) images were acquired at the USTEM facility of the TU Wien. In Figure 3.6 an SEM image of the 250 cycle Pt surface shows that the film is homogeneous from top view with a slight hill structure. As this top view does not yield much information about the morphology of Pt, cross sectional cut samples were used in TEM to show the zirconia support and illustrate the different film structures of Pt.

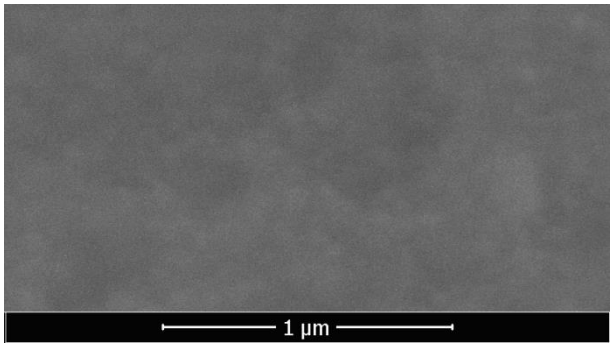

Figure 3.6: SEM image of a continuous 250 cycle ALD Pt film.

The TEM images for films with 400 deposition cycles of zirconia and 5, 10, 50, 125 and 250 ALD cycles of Pt are depicted in Figure 3.7 to Figure 3.11. The supporting zirconia films consist of two discernible parts. The oxide was not deposited in one ALD session of 400 deposition cycles, but in two sessions of 200 cycles each. The thickness of each zirconia layer is constant and the surface smooth and homogeneous. Concerning the crystallinity, large crystallites can be observed as areas of different brightness. The crystallites are in several places connected across the separately deposited layers.

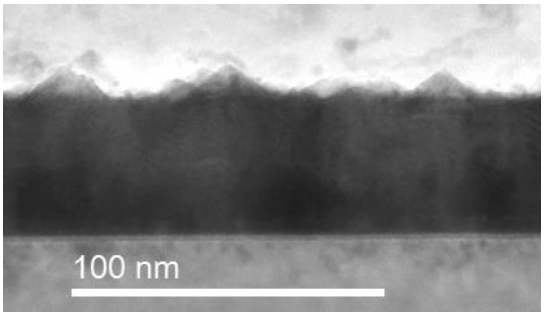

Figure 3.7: 5 cycle ALD Pt sample. The deposited Pt forms individual particles on the surface.

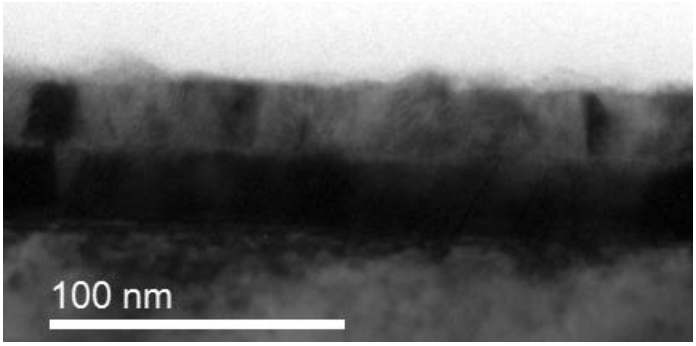

Figure 3.8: 10 cycle ALD Pt sample. The deposited Pt forms individual particles on the surface. Due to the cross sectional preparation the Pt is less visible than for the 5 cycle ALD sample, but the visible Pt directly at the zirconia interface are slightly broader and almost cover the whole surface.

For the two samples with the least amount of Pt on the surface (5 & 10 cycles) the Pt forms nanoparticles. Their shape appears to be half spheres with a slightly pyramidal distortion. For the "ticker" film with 50 deposition cycles the nanoparticles have a more spherical shape and already start to build overlaps, forming island structures. Therefore, the amount of open interfaces between Pt and support is lower than for the 5 and 10 cycle films.

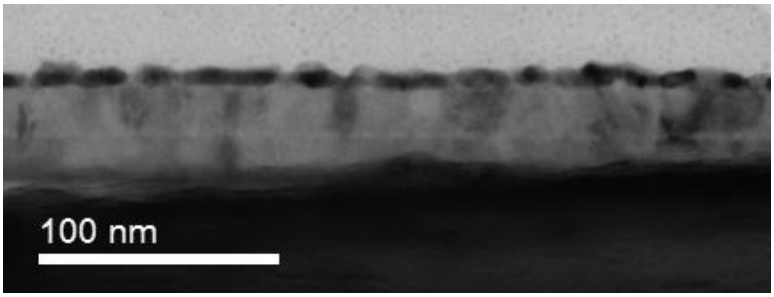

Figure 3.9: 50 cycle ALD Pt sample. The Pt film consists of particles that start to merge into a continuous film.

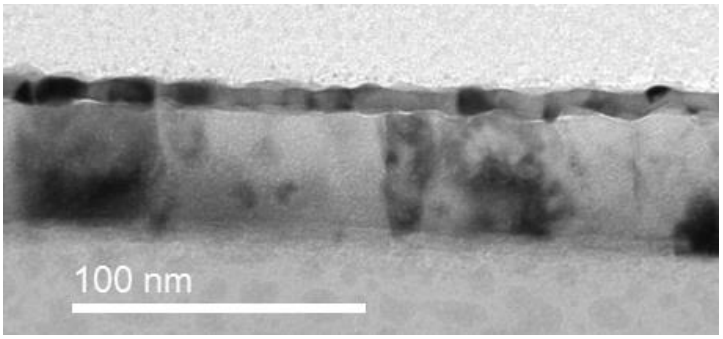

Figure 3.10: 125 cycle ALD Pt sample. The Pt forms a closed layer but still shows a granular structure of merging particles.

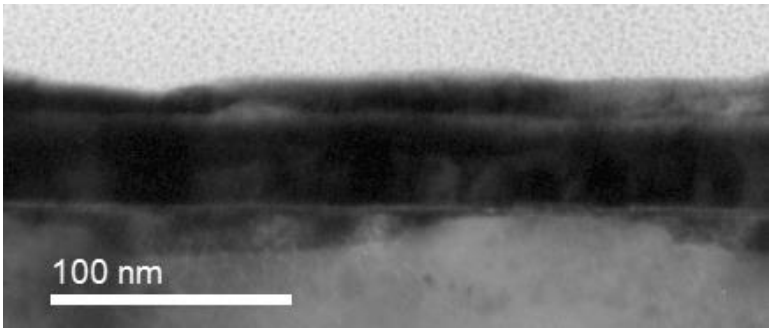

Figure 3.11: 250 cycle ALD Pt sample. The Pt forms a closed, thick layer.

The images of the 125 and 250 cycle model catalysts show closed Pt surfaces. The Pt is smoothing out the particle character with increasing numbers of deposition cycles. The continuous film "shuts off" the Pt-support interfaces from the gas phase, except on the sample sides. The smoothed Pt film of the 250 cycle sample is expected to behave like standard bulk Pt.

TEM can also be used to complement the crystallinity measurements of XRD. Images at high resolution can directly show the crystallinity of particles. Examples can be seen in Figure 3.12 and Figure 3.13 for 10 and 125 deposition cycles, respectively. In Figure 3.12 the polyhedral shape of the nano particle for films with few deposition cycles is visible. It has a slightly pyramidal shape with a blunt tip and its crystallinity is visible. For the

continuous surface of the 125 cycle sample in Figure 3.13 the crystallinity of Pt is also directly observed. The connected particles can still be distinguished. They appear to have grown individually until they reached a common height.

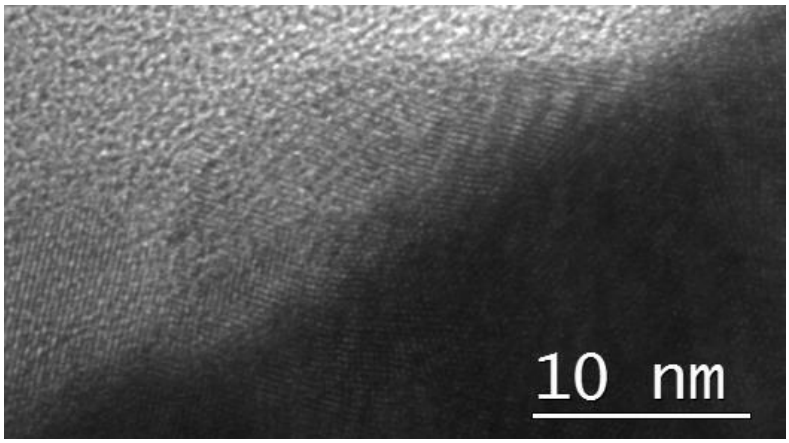

Figure 3.12: Nano particle prepared with 10 ALD cycles.

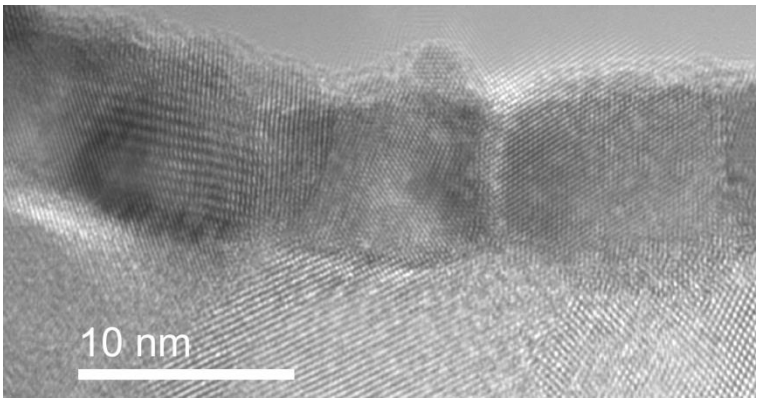

Figure 3.13: Connected Pt nanoparticles prepared with 125 ALD cycles.

To determine the crystal grain size one can use dark field TEM. Therefore, the direct transmission is blocked and an aperture is used to only observe electrons diffracted in a special direction. This allows the observation of crystals with a lattice orientation matching this diffraction (crystals with selected orientation are bright in the images). The dark field measurements are also well suited to compare the surface structures.

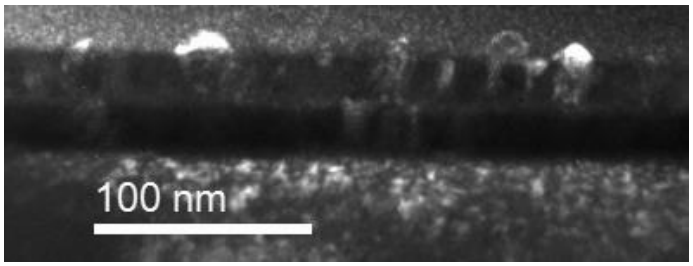

Figure 3.14: Dark field TEM of 10 cycle ALD Pt sample. Small nano particles on the surface are assumed to be small single crystals. Only two of the observed crystallites have the same orientation.

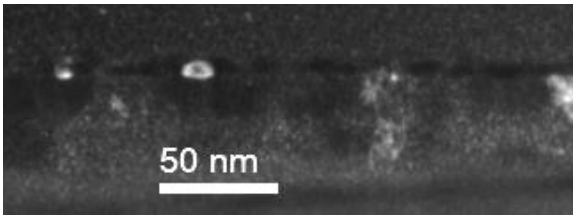

Figure 3.15: Dark field TEM of 50 cycle ALD Pt sample. Crystallites have about the same size as on films with fewer deposition cycles but are surrounded by more Pt particles on the surface (dark black shapes).

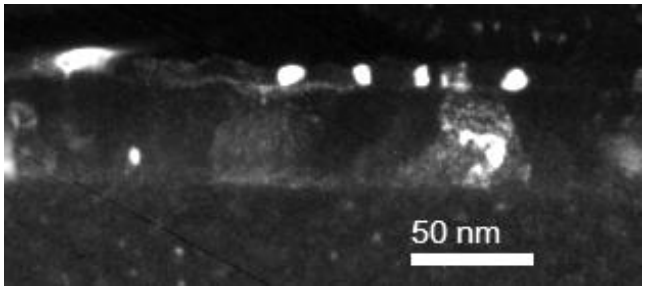

Figure 3.16: Dark field TEM of 125 cycle ALD Pt sample. Most crystallites are still small like they are on films with fewer deposition cycles but also larger crystal grains are forming. In addition, one of the much larger zirconia crystallites lighted up in this image.

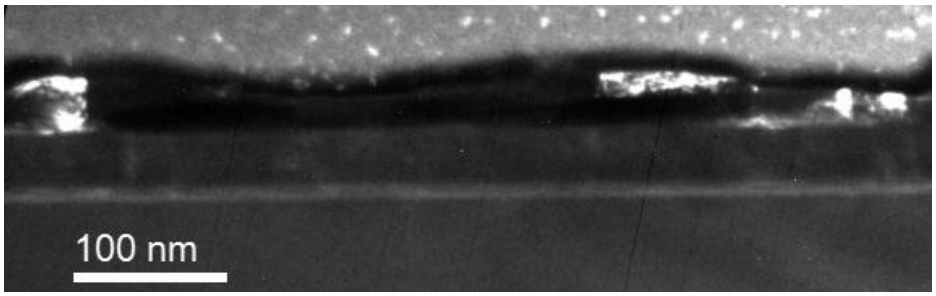

Figure 3.17: Dark field TEM of 250 cycle ALD Pt sample. Some crystallites are much larger than those of the films with fewer deposition cycles. Apparently, crystallites grew together.

The dark field images, shown in Figure 3.14 to Figure 3.17, illustrate very nicely the evolution of the Pt surface with increasing numbers of deposition cycles from small separate single crystalline nanoparticles over a polycrystalline granular film to a smoothed film with larger crystalline structures. These images also confirm that the Pt crystallites on the surface do not have the same azimuthal growth direction or there would have been more crystallites that light up for one setting (coherent centers).

3.3.3 X-ray photoelectron spectroscopy

Finally, the samples were characterized by XPS, which can be used to check for impurities, determine the oxidation state of Pt (or in this case the nano particle character) and to verify that the Pt film is continuous (when the Pt layer is thick enough that it shields the Zr signal).

These following XPS spectra were taken with a laboratory XPS system. For the samples with 5 to 250 Pt deposition cycles survey spectra and the C1s, Pt4f and Zr3d core levels were measured. Figure 3.18 and Figure 3.19 show the results combined for all samples for C 1s and Pt 4f/Zr 3d, respectively. The spectra were calibrated for graphitic carbon as visible in Figure 3.18.

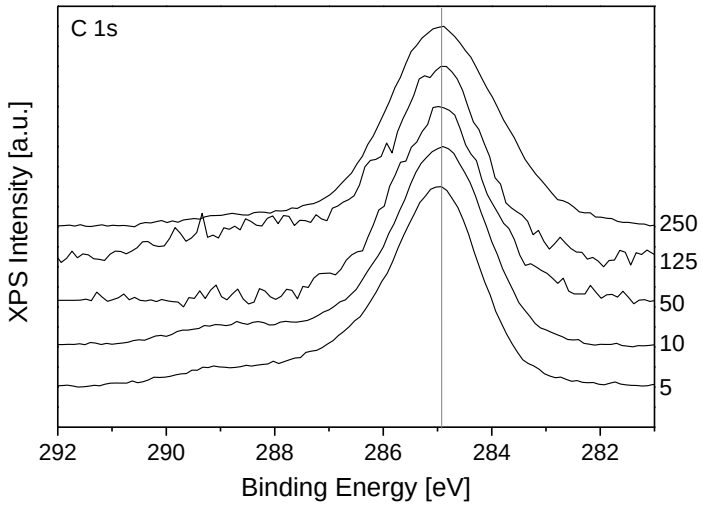

Figure 3.18: Intensity-normalized C1s spectra of all five samples. The graphitic carbon peak maximum (at 284.9) was used for energy calibration of the spectra.

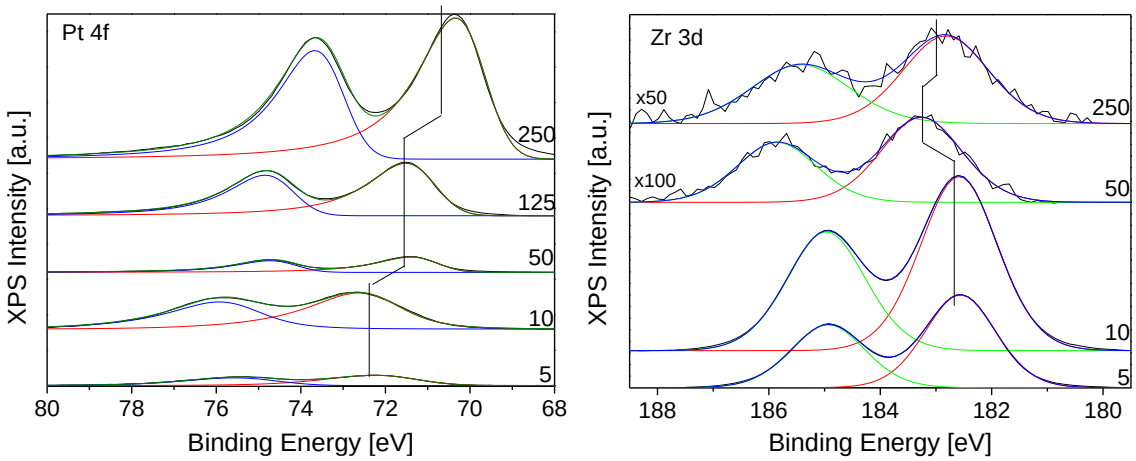

Figure 3.19: Pt 4f and Zr 3d spectra of the different samples. The Pt deposition cycles are denoted on the side. The Zr 3d for 125 cycles is not shown, as it was zero.

Contrary to expectations (the thicker films should shield the Zr 3d signal better), the "thickest" film yielded a signal for Zr 3d that was not visible for the 125 cycle film. This is due to prior treatment of the 250 cycle ALD Pt sample and the absence of a replacement. The measured 250 cycle sample was previously sputtered for SFG measurements in Trieste and in addition some beam damage (from the high power IR radiation in that setup) of the sample surface could be observed by the naked eye. It is expected that a fresh sample with 250 cycle Pt deposition does not yield a Zr 3d signal. It is also worth mentioning that a shift in the binding energy of Pt was observed for the different samples. For those with fewer ALD cycles the Pt was shifted to higher binding energies. This is a typical phenomenon for metal nanoparticles, thus correlates well with our expectations from the other characterization measurements. It was not possible to calculate absolute amounts of Pt on the samples from our measurements, as there was no reference signal to quantify the XPS intensity (which can vary strongly with tilt and distance of the sample to the analyzer). In addition, varying amounts of surface carbon prevents a direct comparison. Nevertheless, in Table 3.4 the peak areas and deduced ratios between Pt and Zr signals are denoted for basic comparison. For the two samples with least deposition cycles a two-fold increase for the Pt/Zr peak area ratio matches the actual increase in surface Pt as, due to its separated particle structure, the Pt did not diminish the Zr signal at this point. For the 50 cycle sample the ratio is much higher than five times the ratio of the 10 cycle film as the Pt actively diminishes the Zr signal. The Zr signal of the 125 cycle film is then not observed anymore due to the thick continuous Pt film and the 250 cycle film shows, as mentioned before, only a Zr signal because of the surface alteration.

Table 3.4: Peak area of Zr 3d and Pt 4f and the ratio of Pt- /Zr-area for the different samples.

	Zr Area	Pt Area	Ratio Pt/Zr
5	32459	4081	0,125
10	66067	16089	0,243
50	339	4913	14,492
125	-	17874	-
250	753	48240	64,06

We also measured O1s spectra in our lab and at the BESSY II synchrotron facility. The O1s signal was expected to have one feature from the oxygen in the zirconia support (for the samples that had visible the zirconia peaks). Interestingly, apart from oxygen corresponding to zirconia, a second feature at higher binding energy was observed with

relatively high intensity. Figure 3.20 shows a survey as well as O 1s and C 1s of a pristine, clean 750 cycle Pt film at 600 °C in UHV (BESSY II). The small feature at 529.2 eV belongs to oxygen of the zirconia support. The origin of the peak at 531.6 eV is not related to the zirconia as it was very intense also for thick Pt films. To check if the oxygen was an adsorbed surface species, the sample was heated in 10^{-8} mbar vacuum to 600 °C, an environment where surface oxygen should have desorbed from Pt. Nevertheless, as seen in in the bottom left of Figure 3.20 the feature at 531.6 eV was still visible. Only at even higher temperatures (700°C) the peak disappeared. Following the disappearance of the 531.6 eV peak, the 529.2 eV feature increased strongly, which indicated that some zirconia was not covered by Pt anymore. These observations led to the conclusion that the high binding energy oxygen signal originated from oxygen trapped within the Pt bulk. This was caused by the ALD process, with the alternating $MeCpPtMe_3$ and O_2 cycles and some incomplete reactions. Heating to high enough temperatures allowed the oxygen to leave the bulk, while influencing the Pt film morphology (without changing the chemical state) and uncovering parts of the zirconia support.

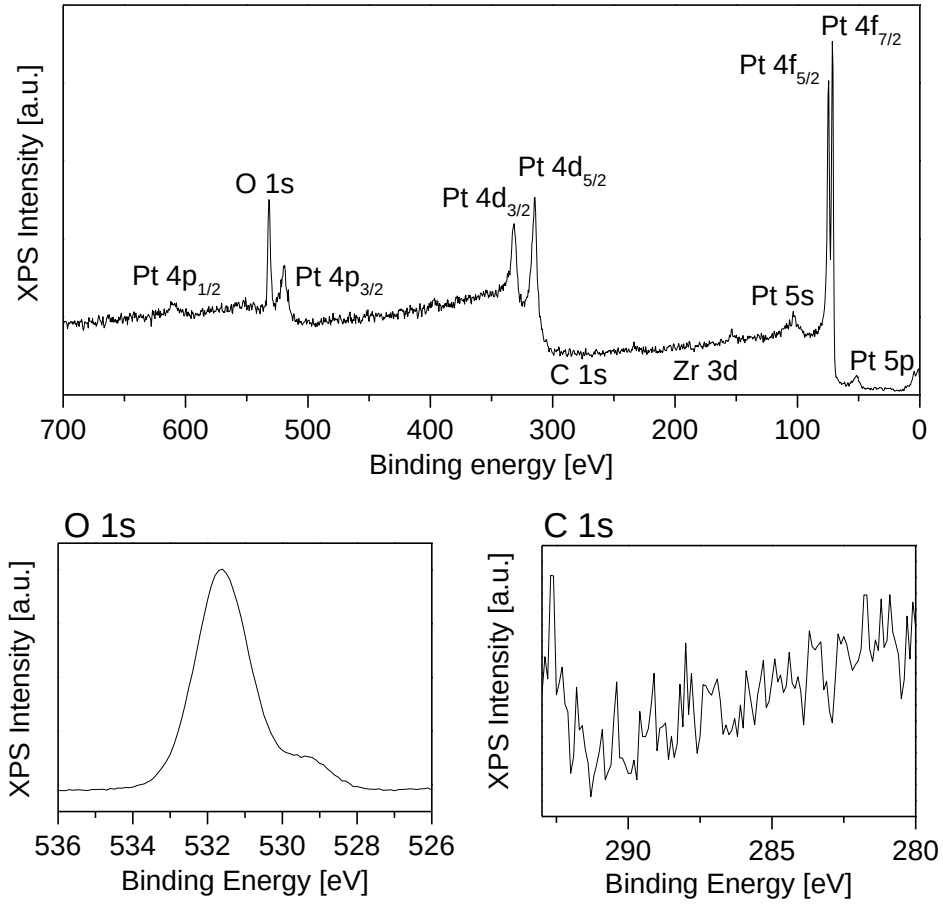

Figure 3.20: Survey, O 1s and C 1s spectrum of pristine 750 cycle Pt film at 600 °C, measured at BESSY II. A large oxygen peak at 531.6 eV can be observed in addition to the small 529.2 eV peak of oxygen in zirconia.

SEM images after the high temperature measurements showed that the Pt formed a meandering structure with exposed zirconia areas, as seen in Figure 3.21.

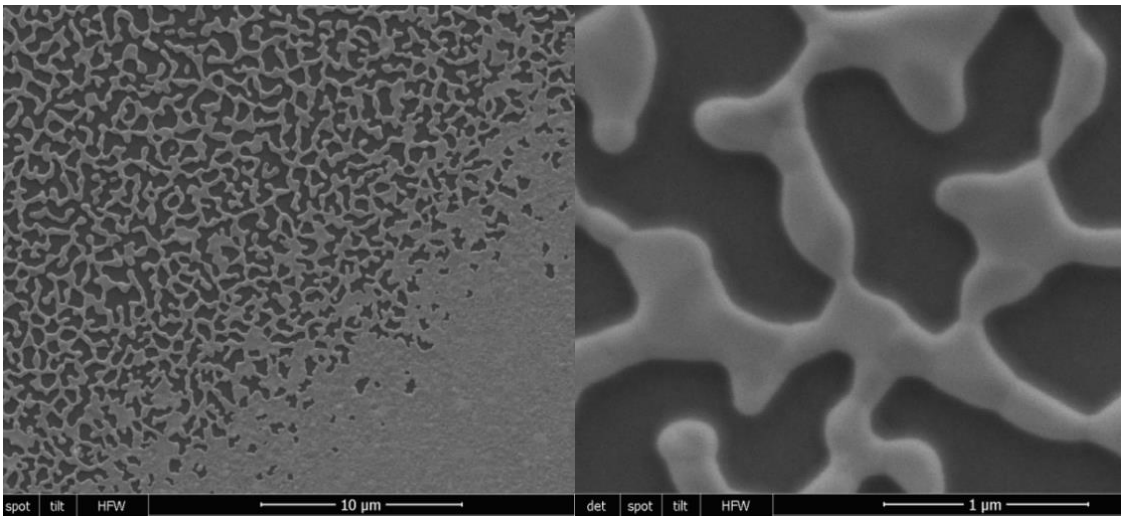

Figure 3.21: SEM images of thick 750 cycle Pt film after heating to 700 °C in UHV. The left panel shows the transition between laser heated part (upper left) and pristine surface (lower right). The right panel shows a magnification of the meandering Pt with exposed zirconia.

3.4 Model Catalysts with Sputter Deposited Pt

In addition to the model catalysts prepared exclusively with ALD, we also used some samples with the Pt added through sputter deposition onto an ALD zirconia film. The thickness of these Pt films was estimated based on sputtering time and deposition rate to be 2, 5, 10 and 30 nm. These samples should be roughly correlating to the films with 50, 125, 250 and 750 ALD deposition cycles.

Contrary to the ALD samples we did not perform the same extensive characterization of the sputter deposited samples. Prior to basic characterization we performed CO adsorption measurements on all samples. These measurements will be shown in chapter 5 for the ALD and sputter deposited samples. The sputter deposited Pt films exhibited strange behavior and after measurements showed surface changes in terms of dark colored spots. These spots are due to surface damage by the high power IR radiation of the SFG experiments. To investigate these changes we performed XPS measurements in the XPS center of the TU Wien, enabling a spatial resolution of 80 micrometers.

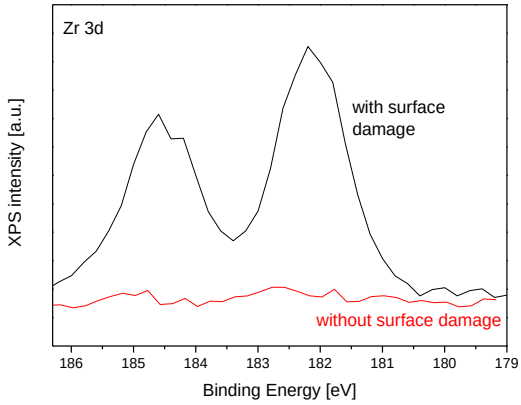

Figure 3.22: Zr 3d signal of damaged and as prepared sputtered Pt film of 10 nm nominal thickness. For the damaged surface a Zr 3d signal was observable. This is an indication that the Pt coverage of the surface must have changed.

The XPS measurements in Figure 3.22 clearly showed that zirconia was uncovered by the SFG measurements. This may have been due to Pt agglomeration. To get a better impression we also took scanning electron microscopy (SEM) images. Figure 3.23 shows three spots on the surface of the 5 nm Pt film. On the left the pristine sputter deposited Pt is shown. Some surface irregularities were observed in form of brighter spots (surface roughness). The middle and right SEM images show that for the sputtered samples the Pt peels away from the zirconia support upon IR radiation in the SFG process. This behavior of the surface would have compromised any characterization or catalytic reactivity measurements. Therefore, we did not perform further characterization or reaction measurements on the sputter deposited Pt films. The adsorption measurements in pure CO environment will be shown in chapter 5.3.

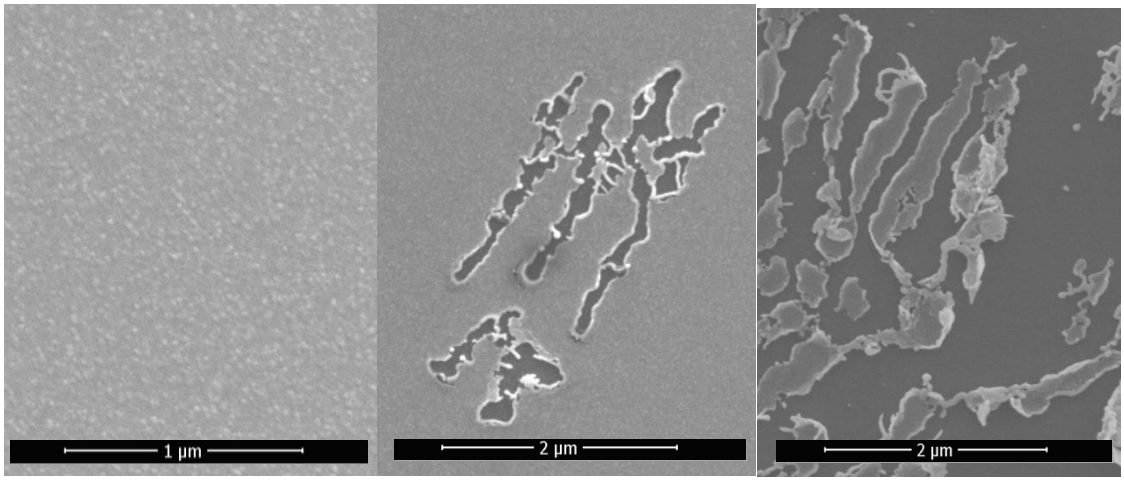

Figure 3.23: SEM images of 10 nm sputter deposited Pt film. Left: the film as prepared, middle: start of surface damage, right: Pt curled up with large uncovered zirconia surface.

4 SFG Setup and Reference Measurements

The complex process described above requires a sophisticated setup. Pulsed lasers are required for the non-linear process, because the electric field $\vec{E}$ needs to be strong for the second order term to become significant. In addition, the number of SFG photons is still low requiring a sensitive detector. The experimental geometry of the sample stage must then comply with the specifications of the SFG process. The resulting setup will be discussed in the following paragraphs.

4.1 Laser System

The SFG process requires two input beams. One is chosen as visible light and one is scanning IR for vibrational spectroscopy. We used a system from EKSPLA [52], which generates both beams from one initial laser. This initial laser is a diode laser that is amplified with Nd:YAG laser crystals in two stages. The Nd:YAG crystals are pumped by flashlamps. The first amplification state is an amplifier cavity, where the number of roundtrips can be chosen depending on the desired amplification. The second stage is a single reflectance path, where the delay between pump pulse and laser pulse can be chosen. As a result of using Nd:YAG crystals the first stage of the laser system generates a 1064 nm beam with up to 25 mJ beam energy at a repetition rate of 50 Hz and 25-30 ps puls length with a beam diameter of roughly 8 mm.

After splitting off part of this beam, the remaining light is fed through a KDP crystal for frequency doubling (SHG) to generate 532 nm visible light. Part of the frequency doubled visible beam is used directly for the SFG process, the rest is used for the generation of scanning IR light. The VIS beam used for the SFG process has a maximum power of 2 mJ but is always used with reduced energy in experiments.

The previously split off 1064 nm light and part of the 532 nm light are further used for a difference frequency generation (DFG/ optical parametric amplification, OPA) stage. Both beams have roughly 5 mJ. The green light is fed through BBO crystals for parametric generation (OPG) and the resulting light is wavelength selected with a diffraction grating. Then it is mixed with the 1064 nm light in a $AgGaS_2$ crystal. The resulting beam can have a wavelength from 2.3 to 10 µm (wavenumber of 4000 to 1000 cm^{-1}) and is p-polarized with a varying power of several mJ with minima at 4000 and 1000 cm^{-1}.

The VIS beam requires a waveplate-polarizer cube arrangement to tune the beam intensity and a $\lambda/2$ waveplate after the polarizer cube to get the desired polarization for the measurement. It is also important to add an adjustable delay path for the VIS beam (as its optical path is usually shorter than the path for generating IR light) to ensure that laser pulses are temporally overlapped for the SFG process.

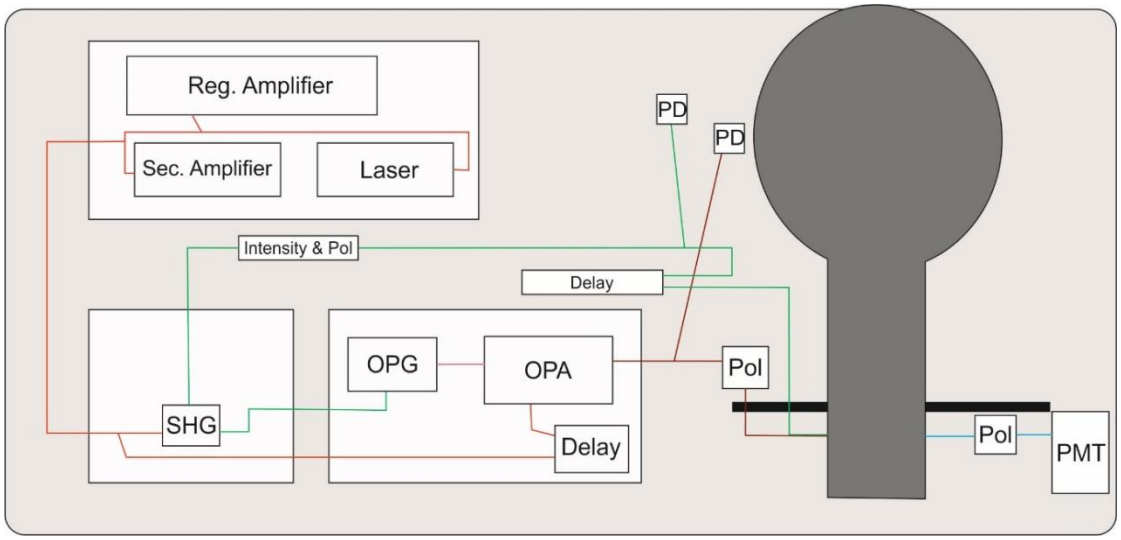

Figure 4.1: Top-view of setup and beam paths of the measurement system. A primary pulsed laser is frequency doubled to 532 nm in the SHG unit. The green beam is split, one beam directed at the measurements cell, the other one used for optical parametric amplification to generate tunable IR light. VIS and IR beams are used to generate SFG light that is detected by a PMT detector.

The beams are then optimized for a horizontal sample surface. The incidence angles are 45° and 59° for the IR and VIS beam, respectively. After the sample the green beam is partially blocked by an iris diaphragm to reduce green stray light in the detector. The SFG beam is further modified by a polarizer to select s or p polarization and an edge filter to reduce influence of green light. It is then detected with a photon multiplier tube (PMT) to count the low number of SFG photons. A schematic overview of the whole setup is shown in Figure 4.1.

4.1.1 Measurement chamber

The sample stage for SFG measurements is strongly depending on the investigated surfaces/interfaces. Possible sample stages can be movable bowls for liquid/gas, Langmuir Blodgett troughs for SAMs/gas, coated prisms for liquid/solid interfaces and various others. In our case a closed cell is required to provide reaction environment for catalytic measurements. This was achieved with a high pressure cell that could also be pumped to low vacuum pressures, desirably down to 10^{-8} mbar. A schematic of the

design of our initial simple cell is shown in Figure 4.2. Such a setup can be improved by connecting it to a large UHV chamber for surface preparation and characterization, as described before ("Rupprechter Design") [18, 53, 54].

A new combined, modified and upgraded setup was constructed as part of the PhD thesis of Matteo Roiaz and is described in detail in reference [55]. The high pressure cell features two windows matching the incidence and exit angles of the SFG beams. The windows are made from CaF_2 to enable high transmission of the IR light. Gases can be dosed via a leak valve and a standard gas dosing valve. The chamber can be pumped down to $5 \cdot 10^{-9}$ mbar and gases can be dosed up to 1.1 bar. In addition, the gas phase composition can be detected with a mass spectrometer to check the purity of gases and follow catalytic reactions by using an additional leak valve. In the first setup one single sample stage was fixed inside the chamber with resistive heating to 550 °C and a thermocouple inside the stage. For the new setup the sample can be mounted on two different stages. One sample stage can be heated resistively by an integrated heating coil. Depending on the gas environment it can reach 700-800 °C. This stage is preferable for thin samples that can be clamped to the surface. The second stage is designed for single crystals. There heating is achieved be running a high current through the wires that hold the single crystal (many single crystals have a groove on the side to facilitate mounting). With this stage temperatures to above 1000 °C can be achieved.

The new chamber has, however, two drawbacks. The first one is that of beam angles are fixed. The SFG intensities may strongly depend on the experimental configuration. Without being able to change the incident angles it is possible that in several cases only suboptimal results are achieved. The second drawback is the IR adsorption of the gas phase inside the reaction chamber. The SFG intensity is directly proportional to the IR and VIS intensity. Thus, absorption of IR light by gas molecules needs to be considered in the spectra. For this purpose a photodiode is monitoring the IR intensity, which is placed prior to the cell. It allows compensation of IR absorption from molecules in surrounding air, but not absorption from the gas phase inside the chamber. In comparison, monitoring the IR light after the cell would include the additional path through the gas phase after the sample, also impractical for normalization. A possibility to counter the influence of absorption would be a recessed incidence window that is closer to the sample (as used in refs. [18, 53-55]), which would further restrict the beam paths and require specific components to fit the windows. It is more feasible to use reference measurements with a non-centrosymmetric material and the gas phase in question to calculate compensation factors for spectra at different pressures.

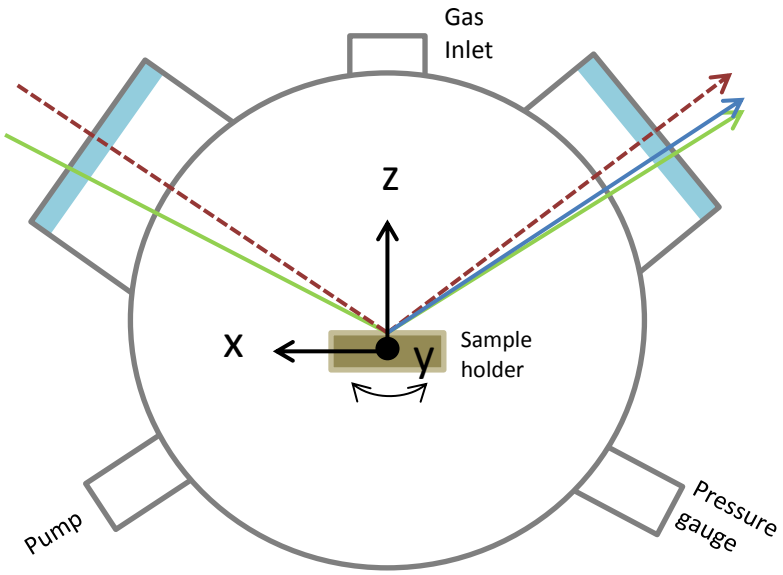

Figure 4.2: Layout of first measurement chamber. CaF_2 windows allowed the beams to enter and exit the chamber. The sample holder could be adjusted in x,y and z direction and tilted. Additional flanges were used to change and check the gas atmosphere.

The SFG beams are adjusted for a fixed height horizontal surface. Sample surfaces are often slightly tilted and samples can strongly vary in thickness. Therefore the sample stage is mounted on a manipulator that can be shifted in all three spatial directions and it can be tilted along the plane of incidence of the beams. With this setup it is possible to adjust samples of different height to intercept the SFG beams where they spatially overlap. It can also be used to compensate surface tilt in direction of, but not perpendicular to the beams. Samples have to be installed accordingly as the only possibility to change the tilt in the other direction would be to tilt the mounting of the connected high pressure and UHV chambers (which is rather impractical).

4.1.2 Add-ons: Pump-Probe

One of the advantages of SFG in comparison to other surface IR techniques like PM-IRAS is the possibility to measure time dependent processes. While the pulsed lasers require a quite extensive installation they also come with advantages. For a pump-probe system a pump is applied to trigger an action of the sample and a probe is used afterwards to monitor the temporal evolution. The pump can for example be a heat pulse or molecule excitation. In these cases the probe is used to monitor the heat dissipation or coupling of molecular transitions.

For our SFG setup the standard SFG process is used as probe. A pump pulse can be generated directly at either 1064 nm or 532 nm. Depending on the system it is most

likely used as heat pump but for some surfaces may be used to drive transitions [56]. The temporal resolution is limited by the pulse length. In our case the pulse length is rather long for pump-probe systems with 25 ps. Heat dissipation through electronic effects cannot be observed with this time scale and would require fs pulses [57]. Nevertheless, mechanical heat dissipation can be observed as well as temperature dependent adsorption and desorption effects [58, 59]. It is also possible to investigate effects that need high fields by temporal overlap of pump and probe pulses (adding an excitation).

To use the 1064 nm light as pump laser a second waveplate and polarizing beam splitter (there is already a set to split off light for the DFG) would be required in a very tight space. The benefit of integrating this beam is the splitting inside the SHG box with a shutter for the pump beam. To use the 532 nm beam a waveplate and polarizing beam splitter are required outside the SGH box as there is not enough space inside. In addition, there are no mirrors for beam positioning of this beam prior to the intensity and polarization adjustment stage, thus a beam splitter can have a huge negative impact on the alignment. The beam path for a 532 nm pump beam integrated in the standard setup (as already realized in our setup) is shown in Figure 4.3. All other pump setups would need an additional laser as source and would be harder to integrate as the pulses need to be coordinated and the remaining work space is quite limited.

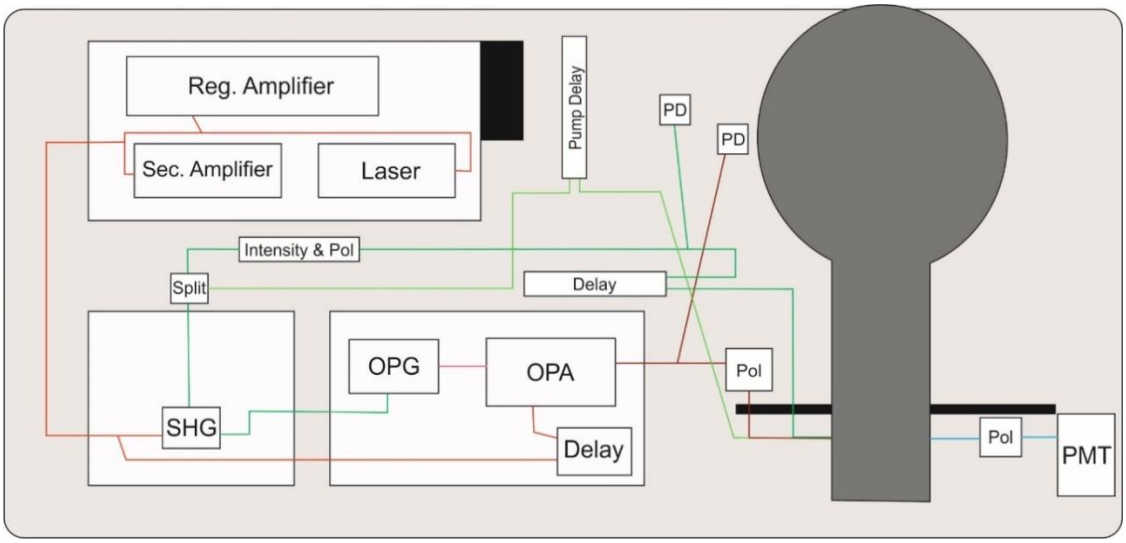

Figure 4.3: Top view of pump laser added to SFG setup. The light green colored beam path belongs to the 532 nm pump. It is split off using a $\lambda/2$ waveplate and polarizing beam splitter. A motorized delay line is used to control the temporal offset of pump and probe.

4.2 Adjustment and Maintenance

4.2.1 Heating of the sample

In the first measurement chamber, where most of the adsorption and oxidation measurements were performed, the thermocouple was positioned inside the sample stage. To ensure that the logged temperature were correlated compared to the actual sample temperature, a measurement was performed with a second thermocouple fixed to the surface of a sample. Temperature was ramped up to 500 °C. Higher temperatures were not investigated as the sample stage could not be used at higher temperatures due to the temperature limitations of the ceramic feed through. The results are plotted in Figure 4.4, where the red dotted line shows the optimum correspondence of temperatures and the black squares show the measured values. While a small difference emerges at higher temperatures, the divergence is insignificant with 10 °C difference at 500 °C. Most measurements only use temperatures up to 450 °C and the temperature steps do not require adjustment.

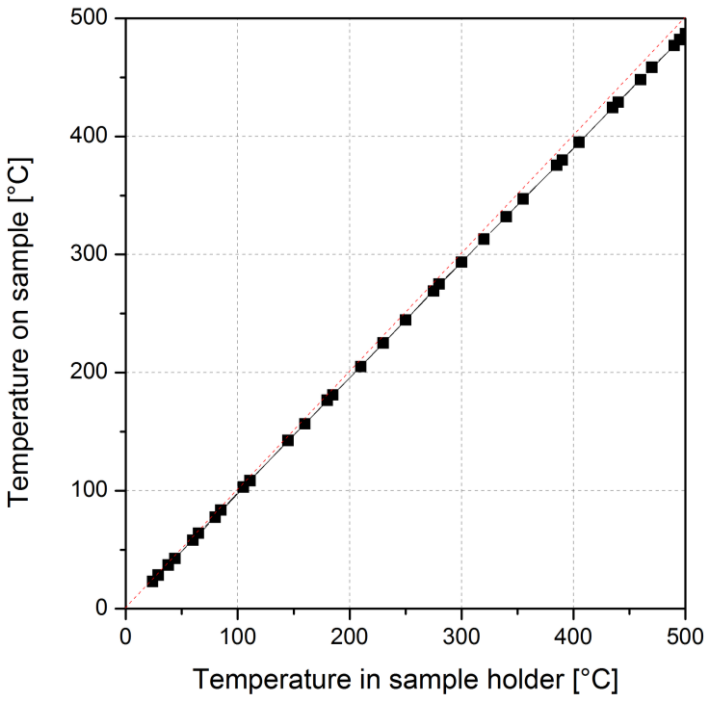

Figure 4.4: Comparison of temperature in sample stage and on sample surface. The diagonal red dotted line denotes the optimum correlation.

In the new improved measurement chamber the thermocouple is (for the ALD samples on the resistive sample holder) pressed to the sample surface by the wire grid that is also used to fix the sample on the holder. Thus, the thermocouple is measuring the temperature directly at the surface and no comparison/correction is required.

4.2.2 SFG reference spectra

To evaluate the SFG system, selected parameters for beam output and alignment have to be obtained. The output power of the first and second stage of amplifiers has to be recorded to monitor the overall performance of the laser. The power of the green frequency-doubled beam directed to the chamber is used to check the SHG-crystal alignment. To survey the alignment of the OPG unit one has to consider that the output power is different for every wavelength, depending on the grating and crystals used for frequency mixing.

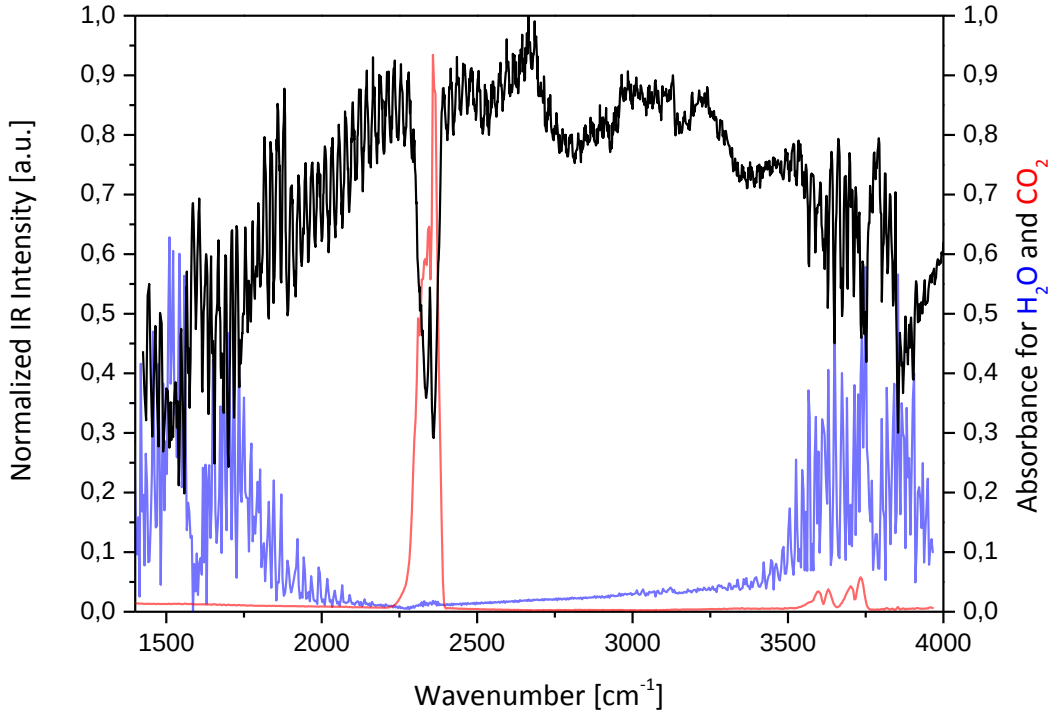

Figure 4.5: Measured SFG Infrared intensity (black) between 1400 and 4000 cm^{-1} compared to H_2O and CO_2 absorption spectra in gas phase (blue & red, respectively) taken from NIST [60]. The IR intensity is breaking down due to absorbance of H_2O and CO_2 in air. In addition, oscillations can be seen due to interference at the photo diode.

Figure 4.5 shows a curve of infrared beam power with respect to infrared wavelength. This curve also explains some of the dips seen in IR intensity by absorption in air. Gas phase water shows huge IR absorption between 1300 and 1800 wavenumbers, generated by H-O-H bending as well as at higher wavenumbers starting around 3500 cm^{-1}, arising from O-H stretch vibrations. CO_2 causes a strong signal decrease between 2300 and 2400 cm^{-1} due to C-O stretching. The reference spectra are shown in Figure 4.5, with data taken from NIST [60]. The blue curve is corresponds to H_2O and the red curve to CO_2. The additional oscillation of the IR curve over the whole plotted range

is attributed to the measuring photo diode because its surface causes interference effects with no influence on the actual power of the beam. By using a Fourier band block filter from 0.04 to 0.058 Hz the interference oscillations can be squelched and the resulting curve is suitable for normalizing the SFG signal.

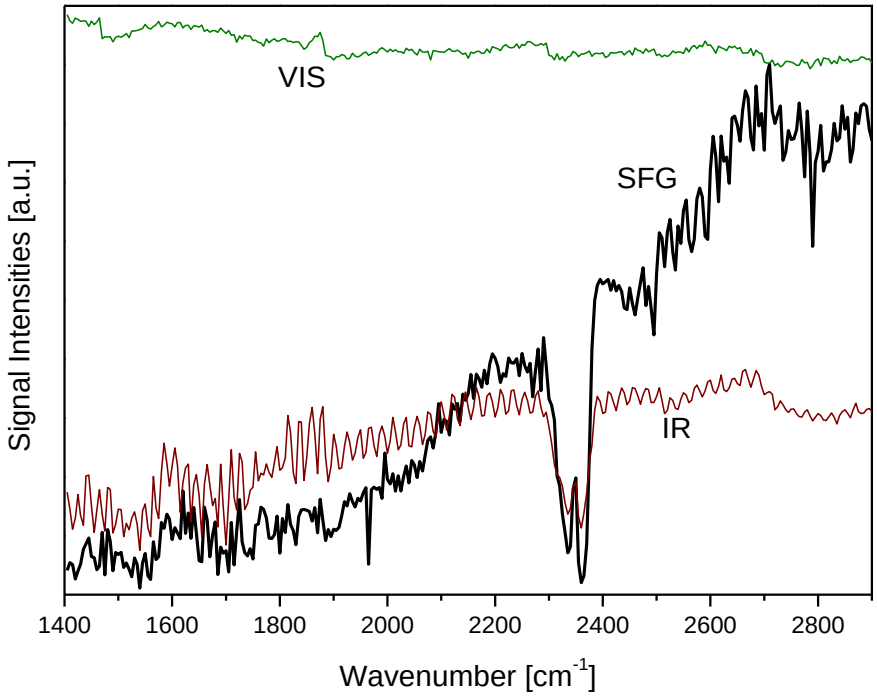

Figure 4.6: Signal intensities of incoming beams and of SFG signal of GaAs, in dependence of wavenumber. The intensity of the IR beam depends on air absorbance as described before. The green light is only influenced by temporal laser instabilities. The SFG signal is influenced by the IR and green beam intensities as well as by the GaAs, where the SFG signal is generated.

After characterizing the beams directed to the sample, special materials can be used to generate SFG signals over a large range of wavenumbers or very distinct resonance peaks due to high grades of molecular ordering. Examples are GaAs or ZnSe for generating high SFG intensity over large range and quartz or ethanol for exhibiting pronounced resonances. Thus, after overlapping the focus of the beams with the correct angles of incidence these materials can be used to find and optimize the SFG signal after roughly setting the mirrors to the right angles with a pilot beam (red diode laser). A suitable wavelength is chosen and the mirrors directing the beam at the photon multiplier are adjusted to maximize the SFG signal. It is also possible to change angle of incidence and position of the infrared beam to obtain a better overlap with the green beam, but this procedure can change the angles of incidence to less suitable values and should only be performed when the SFG signal strength is monitored. A spectrum of a

reference measurement on GaAs is depicted in Figure 4.6, including the measurements of the green and IR laser beam intensities. These can be used to normalize the signal. Normalization is done by dividing the SFG signal by the intensities of the incoming laser beams. The resulting normalized SFG intensity should only depend on the material specific nonlinear susceptibility $\chi^{(2)}$ and, in the best case, show no influence of the IR gas phase absorption.

Nevertheless, despite the normalization, most measured signals still show a significant feature caused by the CO_2 absorption as seen in Figure 4.7, where the black curve is the normalized GaAs spectrum. The orange curve in the same graph shows the normalized intensity of our second commonly used reference material ZnSe. To determine why the normalization with the IR beam does not eliminate the CO_2 intensity loss we measured the pathway of the IR beam through atmosphere for the beams used in the SFG process and the IR measurement (i.e. from the OPA to the chamber and to the photo diode, respectively). The difference in path length is roughly 15 cm. At a total path length of 50 cm this difference is significant and explains why our normalization does cancel the influence of CO_2 in air, but with the limited available space it is not possible to move the photo diode 15 cm farther away to improve the normalization.

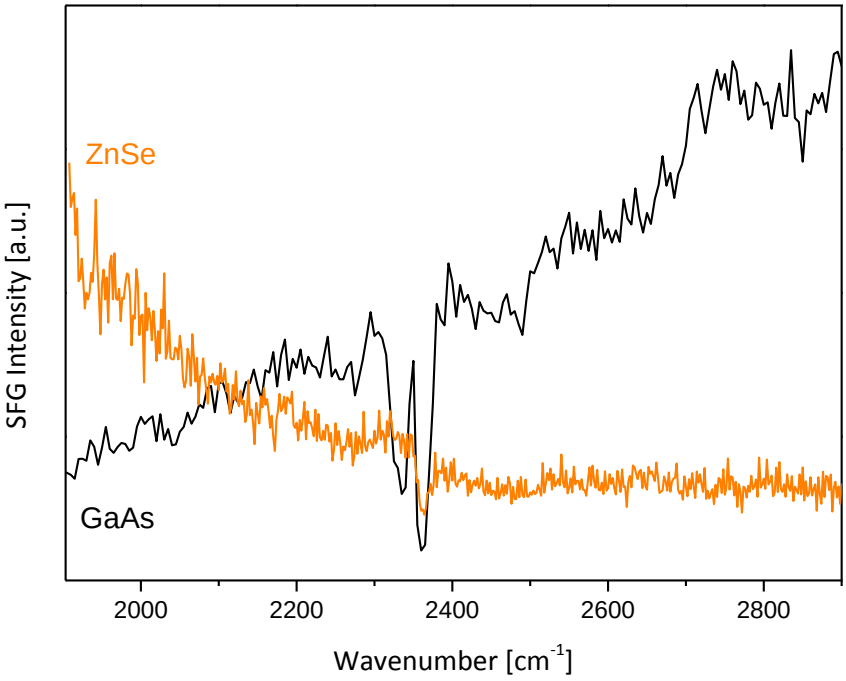

Figure 4.7: Normalized spectra of GaAs (black) and ZnSe (orange) around the CO_2 absorption dip. Even with normalization by dividing through IR and green beam intensities the dip cannot be eliminated.

The log of the visible signal also shows some intensity changes over time. Therefore, we took a time dependent spectrum of the visible, IR and SFG intensities, shown in Figure 4.8. We can see that the visible signal is the most stable, which is expected as it is the first beam generated from the 1064 nm Nd:YVO_4 beam. The infrared is directly dependent on the noise of the green beam as this is part of the difference frequency generation (DFG) used to produce the tunable infrared light. In addition small fluctuations are added to the infrared beam, most likely an error propagation caused by the non-linear crystals used in the DFG. In comparison to the rather low noise of the incoming beams, the SFG signal shows large oscillations. This is on one hand due to the energy threshold of the non-linear effect but the noise does not seem to be fully correlated with the noise of the incident beams. Thus, we think that additional vibrations of the first sample holder (or chamber) played a role in developing the oscillations of the SFG signal.

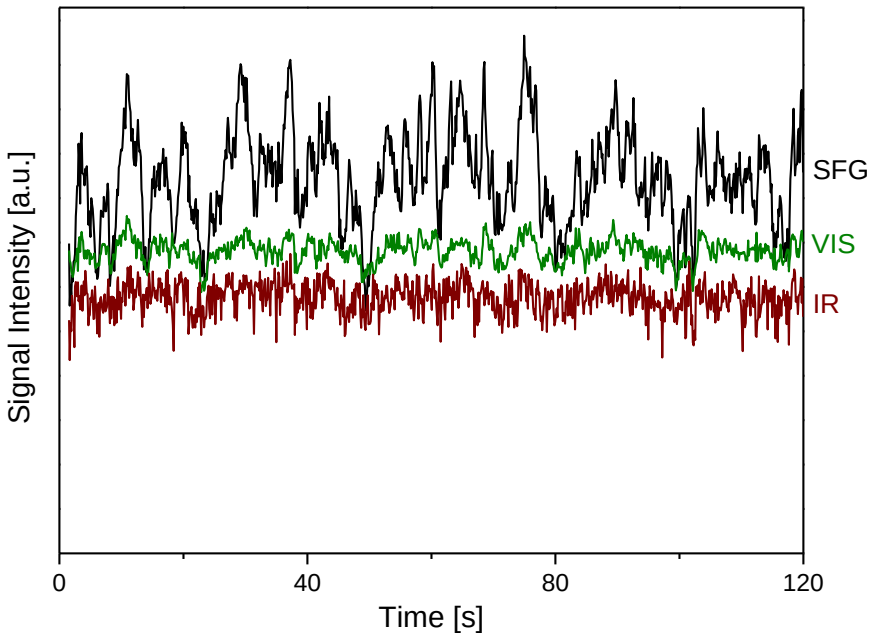

Figure 4.8: Time dependent measurement of intensities of visible, SFG and IR beams on GaAs. The noise of IR and green beams is low in comparison to the noise of the SFG signal.

To finish the measurements on the influence of incoming beams on the SFG signal a measurement was performed to check the proportionality of the SFG signal to the incoming beam intensity. For this measurement we tuned the intensity of the green incoming beam with time while staying at the same wavelength. The green beam was used because the IR beam cannot be tuned in intensity without changing the intensity of the Nd:YVO_4 laser output. The curves for the green and SFG signal as well as the normalized SFG signal are shown in Figure 4.9. Comparing the green and SFG curves the

signals look quite similar, but if they would be directly proportional the resulting normalized curve for dividing the SFG by the green should be a straight line, which is not the case. Apparently when going to low green intensities, the drop in SFG signal is too high. This might be due to a threshold for the non-linear effect generating the SFG photons.

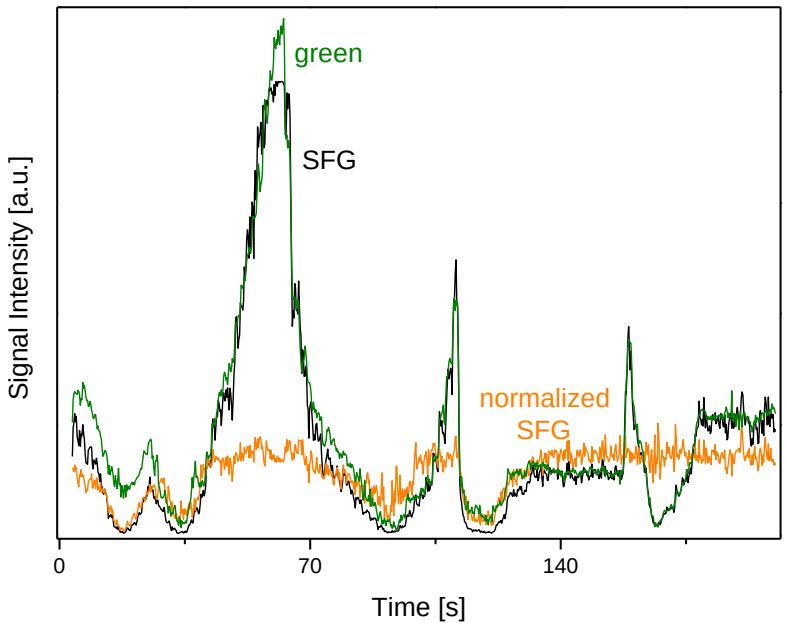

Figure 4.9: Time dependent measurement of green and SFG signal to test proportionality. The normalized signal should be a straight line in case of linear proportionality but instead shows signal dips hinting to a problem like a threshold for the SFG process.

The following experiments were performed at different CO partial pressures. Similar to CO_2 CO absorbs IR light in the gas phase. To rule out that signal of adsorbed CO is decreased or shifted due to the gas phase CO absorption, we performed measurements on GaAs and ZnSe for increasing CO pressures. Figure 4.10 shows data obtained for different CO pressures with ZnSe. Up to 200 mbar no significant loss of SFG signal intensity could be observed. At 200 mbar, the second peak of the gas phase CO absorption could be seen slightly in the red curve. For higher pressures, absorption of the IR light was significant in our small chamber and caused a drop in SFG signal intensity. These measurements showed that we did not have to take this effect into account as the used CO pressures were far below 200 mbar. As the design of the new chamber was analogous to the old chamber, the path length through the gas phase is comparable and the reference spectra are still valid.

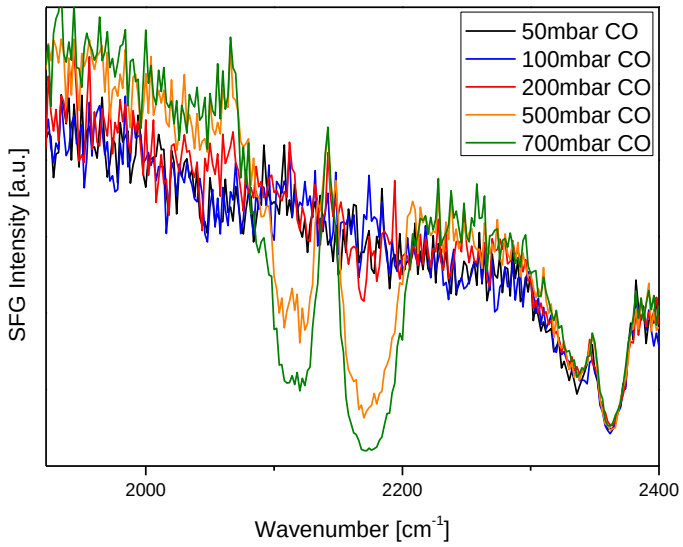

Figure 4.10: ZnSe SFG spectrum in different CO pressures influencing IR incoming beam. Up to 200 mbar CO pressure no influence on the SFG signal could be observed.

5 CO Adsorption

To understand the interaction of reactants with the catalyst surface under reaction conditions, first a basic knowledge of the interaction of each individual reactant with the catalyst is required. This can, for example, provide information on adsorption sites and adsorption strength. This thesis concentrates on the CO oxidation reaction. Therefore, the adsorbates may be CO, oxygen and CO_2. It is known from the literature that CO adsorbs well on Pt and has high coverages at room temperature [61]. In addition, the vibrational frequency of C-O stretching vibrations of CO adsorbed on Pt is located between 1800 and 2150 wavenumbers, well inside the range of our SFG setup (1000-4000). In comparison the O-O and Pt-O stretching vibrations are located below 1000 wavenumbers [62] making it impossible to observe oxygen on our samples directly with our SFG setup. Therefore, the first part of SFG measurements was dedicated to CO adsorption on our model catalysts and some reference single crystal surfaces.

CO resonance positions have already been investigated for Pt single crystals with SFG [53, 63-68]. In comparison to standard IR spectroscopy, the intensities of bridge- and hollow-bonded CO features are reduced. This is of no concern as the strongest CO signal on Pt under regular conditions is on-top CO anyway. Therefore, we are only focusing on the on-top resonances in the following SFG spectra.

5.1 Cleaning Procedure

Model catalysts are, as mentioned before, used to directly relate adsorption/reaction results to specific surface structures and compositions. It is important that there are no impurities hindering CO adsorption. In our case, these might include remains from the ALD process or transport packaging, apart from the standard contamination from air (mainly carbon and water).

For single crystal measurements, the preparation is rather simple [53]. The sample surface is sputtered by argon (by accelerating it towards the sample to kick out surface atoms). Depending on sputtering time and acceleration voltage several surface layers can be removed to ensure that no contaminations remain. Impurities inside the single crystals may remain. The sputtering process leaves the surface in a very rough state due to the ion bombardment. Therefore, surface sputtering is followed by annealing to high temperatures (for Pt around 800-900 °C). The heat allows atoms to move, smoothing the surface again.

The ALD model catalysts also need to be cleaned from surface impurities but sputtering is not a feasible technique. Removing several layers of Pt from a film that only consists of few layers would strongly influence the Pt film or even remove the entire Pt from the surface, especially if the cleaning procedure has to be applied for several measurements. Thus a different approach had to be found. In industrial catalysis the activation of catalysts is often accomplished by applying oxidation and reduction cycles. The oxidation cycles are in general well suited to remove carbon contaminations from the surface of the ALD samples. Based thereon, we tried heating in O_2 to 300 °C to remove carbon and water contamination and successive heating in UHV to 550-600°C to ensure that there was no PtO_x on the surface. Following this, CO adsorption experiments did not yield good spectra (either no CO visible or strongly red-shifted peaks with very low intensity). After several tests the best preparation method for CO on the Pt models was to first heat in O_2 (in our case 5 mbar) to 300°C for 10 minutes, then switch to a 1:1 CO/O_2 mixture (5 mbar) and heat to 250 °C for 15 minutes. The O_2 ensures that the adsorption sites are free for the CO molecules to adsorb on the surface. It seems that the $CO\text{-}O_2$ atmosphere is more capable of cleaning and populating the surface with CO than heating in pure O_2 with successive gas switching. For the adsorption measurements the sample was cooled down in the gas mixture and after reaching room temperature the mixture was exchanged to pure CO.

5.2 Adsorption of CO on ALD Pt Samples

The CO adsorption studies again started with ALD Pt films. We knew that with different numbers of cycles the surface was either more particle-like or smoothed out. For the thicker films with 750 and 250 deposition cycles, the highest ALD smoothness was achieved and with these numbers of layers the support should not influence the adsorption on the Pt surface. We can thus assume that these Pt films were, to some extent, comparable to single crystal measurements. This allowed us to focus our measurements on the known frequency region with some buffer to include background from 2000 to 2150 wavenumbers.

The adsorption spectra were acquired at a gas pressure of 10 mbar CO, which was dosed with the rough dosing valve. The ALD model samples had not been investigated by SFG before, therefore the first step was to check if the surface was flat enough for the technique and if spectra with different polarizations could be obtained. In Figure 5.1 three spectra of on-top CO for a 250 cycle Pt sample are shown. This film is "bulk-like" Pt and should have a smooth surface. The three spectra differ in the used beam

polarizations. The upmost one (green) was measured with p(SFG)p(VIS)p(IR) polarization (standard measurement setting) – the polarizer before the PMT was selecting only the p-polarized part of the SFG light and both incident beams were set to p-polarization. The red and black curves were measured with the polarizer before the PMT selecting s-polarized SFG light. The red one with s(SFG)p(VIS)p(IR) and the black one with s(SFG)s(VIS)p(IR). The peaks were fitted with standard SFG fitting described in chapter 2.1 with functions

$$I_{SFG} = \left|\chi^{(2)}_{eff}\right| \cdot I_{VIS} \cdot I_{IR} \tag{26}$$

and

$$\chi^{(2)}_{eff} = A_{NR} e^{i\phi} + \sum_n \frac{A_n}{\omega_n - \omega_{IR} - \Gamma_n}. \tag{27}$$

The fits are shown as lines in Figure 5.1. With these fits the peak positions could be obtained, which are located at 2080 and 2079 cm^{-1}. A shift of one wavenumber is within the measurement accuracy of the laser setup and in addition the signal to noise ratio is very poor and decreases fit fidelity. Therefore, it is safe to state that all peaks are at the same position as expected for measurements performed on the same system.

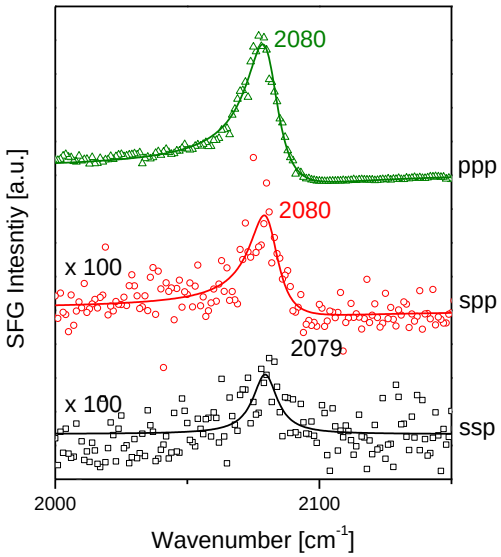

Figure 5.1: Comparison of SFG measurements with different polarizations for 10 mbar CO on 250 cycle ALD Pt. ppp-polarization signal is 100 times higher than those of the other polarizations.

The main difference between the three curves is the intensity. The ppp spectrum has roughly 100 times higher intensity than the other two polarization combinations. This is mainly due to the orientation of the molecular bonds. As described in chapter 2.1.4, the

signal in ppp configuration is in general highest for bonds orthogonal to the surface and is reduced for bonds tilted from the surface normal. In turn, a signal increase for tilted bonds is observed in the ssp signal. Thus, the intensity in this case confirms that the microscopic surface facets are parallel to the macroscopic sample surface with CO bonds aligned with the surface normal. Signals in other polarization combinations are always present to a small extent [69, 70], but may be increased by (tilted) CO bound to step edges. Yet in that case the peaks should be red shifted to lower wavenumbers because CO is bound stronger to step edges [40].

The results also showed a peak asymmetry for two of the measurements. The asymmetry is caused by the phase between resonant and non-resonant parts of the signal. This phase shift should be approximately equal for all CO on Pt systems in different measurement arrangements. The symmetry of the ssp signal is not due to a different phase shift but from the low background. If the non-resonant signal is sufficiently small the asymmetry is not visible regardless of the phase shift. An example for the influence of background intensity is given in Figure 5.2. Simulated SFG peaks with different ratios between resonant and non-resonant amplitude (A_r and A_{nr} respectively) with the same resonance position are put on top of each other. For low non resonant background (e.g. green curve) the peak is almost symmetrical with the highest point at the resonance center. For higher backgrounds the asymmetry gets more and more pronounced.

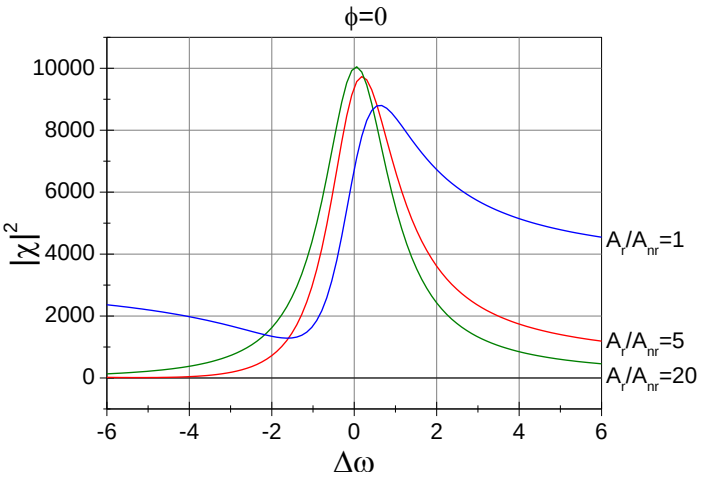

Figure 5.2: Simulation of difference in line shape with constant phase ϕ=0 by changing the ratio between resonant and non-resonant amplitude.

The peak position observed on the clean Pt surface was at 2080 cm^{-1} (obtained from the fit). Only the peak fit of the ssp measurement showed a different peak position, which is most likely due to measurement or fit uncertainty. The peak position corresponds to on-

top CO. Hollow and bridge CO could not be observed and respective regions are therefore not shown. This matches results from single crystals reported in the literature [71-74]. In addition, comparing to single crystal results, the peak position of 2080 cm^{-1} corresponds to roughly 30 % surface coverage. The low surface coverage was most likely related to a shorter CO/O_2 heating stage during the preparation of this sample and could be increased by heating for longer times in CO/O_2 or by repeating the preparation cycle.

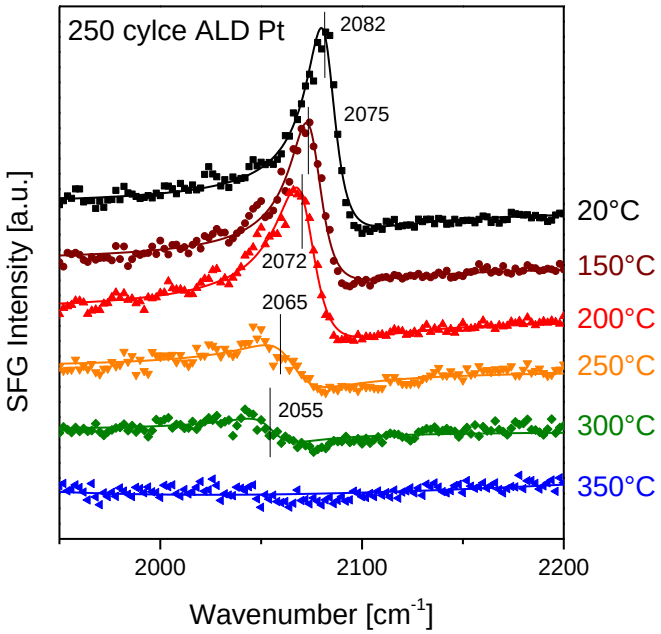

Figure 5.3: Temperature dependent CO adsorption spectra on 250 cycle ALD Pt by in situ SFG. The gas environment was 10 mbar of pure CO. Starting from room temperature the temperature was increased stepwise for each spectrum until the CO signal mostly disappeared.

After the initial tests, the next step in our measurements was a comparison of the temperature dependence of CO adsorption on bulk like 250 cycle ALD platinum, and using a platinum single crystal (Pt 110) as reference. Accordingly, the temperature was increased first from room temperature to 150 °C, followed by stepwise increase of 50 °C. SFG spectra were recorded at each step. The resulting data is plotted in Figure 5.3 and Figure 5.4 for the ALD prepared platinum film and the platinum single crystal, respectively. The collected spectra were again fitted with formula (26) to find intensity, resonance position and phase. The fits are shown as lines in all plots. The resonance position of the low temperature curves (≤200 °C) was similar for the ALD sample and single crystal within measurement accuracy. This indicates that both samples have a comparable binding strength of CO to the surface.

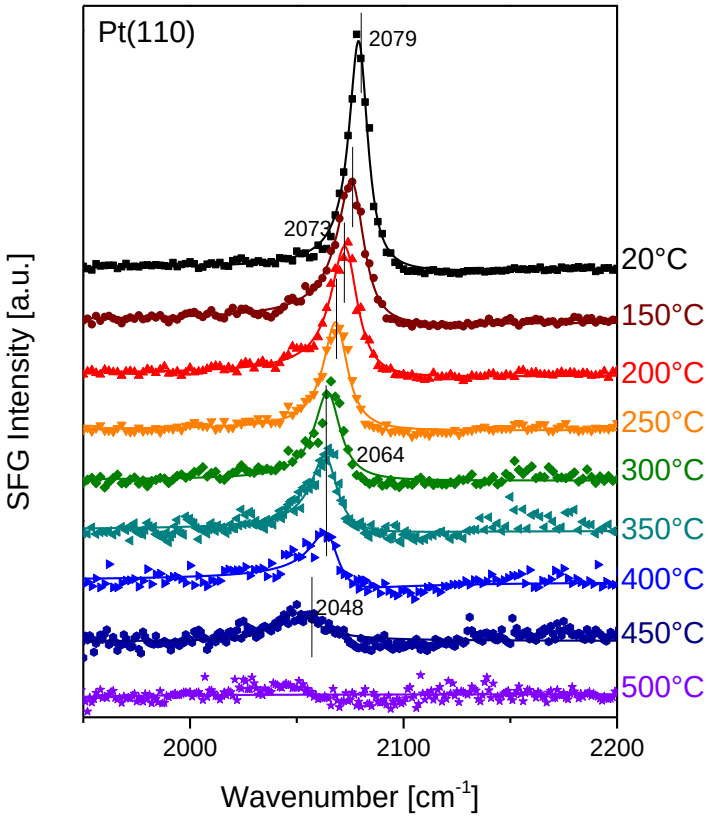

Figure 5.4: Temperature dependent CO adsorption spectra on Pt(110) single crystal by in situ SFG. The gas environment was 10 mbar of pure CO. Starting from room temperature the temperature was increased stepwise for each spectrum until the CO signal disappeared.

For higher temperatures (above 250 °C) larger differences could be observed. The peak intensities and shapes on the ALD film changed dramatically and a shift in resonance position was visible, while there was almost no change for CO on Pt (110) at higher temperatures. This may be due to different reasons. A strong decrease in intensity combined with a red shift in wavenumbers is in many cases an indicator of reduced surface coverage. While CO desorption can be expected for increasing temperature, the temperature for CO desorption on ALD Pt should not differ significantly from desorption on single crystals. This reason is therefore unlikely, as the binding energies for the bulk Pt are similar (peak positions were almost the same for lower temperature spectra).

Another possibility is that a chemical change of the surface took place. For example CO is known to transfer Ni from stainless steel tubing (in form of Ni carbonyls) to the reaction chamber [75, 76], which could have contaminated the surface. This is rather unlikely because it should also affect the single crystal, which was measured in the same chamber, but cannot be excluded as the experimental parameters may differ to a minor

extent. Another possible (chemical) explanation is CO dissociation, which could have taken place on the ALD sample. This could have been caused by the different microscopic roughness of ALD samples compared to single crystal. The ALD sample has a higher surface roughness and therefore could induce CO dissociation. The single crystal had been annealed at a high temperature after previous cleaning procedures and is expected to have a very smooth surface. It would also be possible that some other contamination was present, as our first setup could not reach low 10^{-9} mbar UHV pressures and we could not ensure a highly clean measurement environment. It is also possible that the difference was due to a strong metal support interaction (SMSI) effect [77, 78]. For several material combinations a mechanism was observed in which support materials started covering the surface of metal particles and/or changing the adsorption properties.

To ensure that the problem was not contamination of any kind due to our first simple chamber, the experiments were repeated in Trieste in collaboration with the group of Erik Vesselli [79]. Due to differences in the setup and mounting, the sample preparation was changed from heating in CO/O_2 mixture (for surface cleaning) to a preparation more comparable to the standard single crystal procedure, at the same time limiting the number of possible measurements. The surface was cleaned by sputtering at 1kV acceleration voltage in 10^{-6} mbar Ar background pressure. The sputter time needed to remove approximately two layers was calculated to less than 2 minutes using the formula given by Specs for the sputter rate z/t [80] as

$$\frac{z}{t} = \frac{M}{rN_A e} S\, j_P,$$

where M is the molar weight, r the density of the material, N_A the Avogadro constant, e the electron charge, S the sputtering yield [81] and j_P the primary ion current density (1 mA). Sputtering with afore mentioned values equals a sputtering rate of roughly 1.5 monolayers per minute for the setup in Trieste. With this procedure 3 samples, selected for their significance, were prepared by sputtering for 2 minutes; namely, Pt(111) single crystal as reference, 250 cycle ALD Pt film as bulk sample and 50 cycle ALD Pt film as particle-like sample. In addition, the Pt(111) was annealed to 800°C according to the common cleaning procedure of Pt single crystal surfaces mentioned before. The thin films were not annealed because the oxide support layer might have been altered by such high temperatures e.g. SMSI effect or generation of oxygen vacancies.

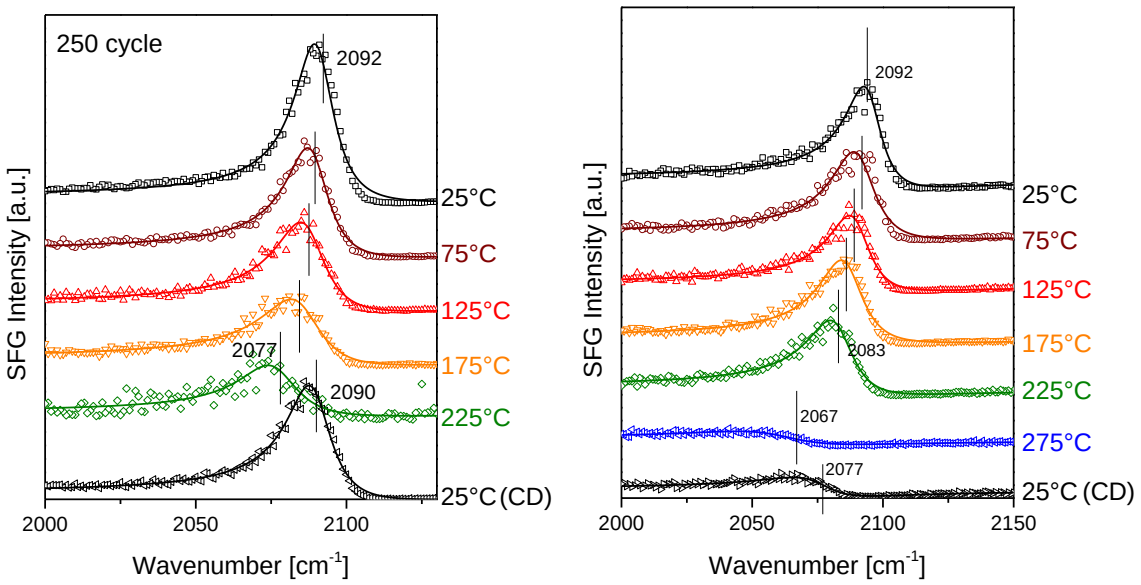

Figure 5.5: Temperature dependent in situ SFG spectra in 10 mbar CO on 250 cycle ALD Pt. The spectra on the left side were measured for temperatures below the strong change in line shape at 275 °C. The spectra on the right side were measured up to one higher temperature step at 275 °C. The bottom spectra (black) are the final cool down spectra after each cycle (in CO).

Measurements of the 250 cycle ALD Pt film in 10 mbar CO are shown in Figure 5.5. Two temperature series were recorded. One with heating up to 225 °C (temperature before the drastic line shape change took place) and one heating up to 275 °C (temperature beyond the drastic line shape change). The bottom spectrum in each graph was taken after subsequent cool down to room temperature in CO. Again, the change was observed after reaching the 275 °C temperature threshold and the second room temperature spectra show that this change was irreversible upon cool down. If we stayed below the critical temperature of 275 °C, the adsorption was fully reversible.

The values for resonance position, resonance width and the phase difference to non-resonant background for line fits of the temperature series to 275 °C are given in Table 5.1 to elaborate the changes. Especially comparing the starting room temperature measurement to the one after cool down shows significant changes. The resonance center was red shifted by 17 wavenumbers hinting to a change in binding energy [82], change in coverage [71] or chemical change as mentioned above. The resonance width increased, so the resonance seemed to be less localized (e.g. through more variation in adsorption sites) and the phase difference to the non-resonant background got larger (hinting at a change in localization of electrons near the surface).

Table 5.1: Position, FWHM and phase of the CO resonances in the temperature series to 275 °C on 250 cycle ALD Pt

250 cycle ALD	25 °C	75 °C	125 °C	175 °C	225 °C	275 °C	25 °C CD
Ω (cm^{-1})	2094	2092	2089	2086	2083	2067	2077
FWHM (cm^{-1})	8.2	9.1	9.4	10.2	10.6	21.5	14.3
Φ (rad)	6.16	6.14	6.15	6.12	6.27	6.86	6.58

Simple desorption of CO was already rendered unlikely, due to comparison between single crystal and ALD samples in our lab. The irreversibility upon cooldown is an additional argument to rule out CO desorption as cause for the signal change. As the CO pressure in the chamber was not changed throughout the measurement, CO would have adsorbed again when the sample was cooled and the initial peak would have been recovered. It is also unlikely that contamination of the surface was the reason for the change as we measured in Trieste at a chamber base pressure of 10^{-8}-10^{-9} mbar. For a clean experimental environment and initially clean Pt surface two scenarios are left: either the surface structure/composition was altered, or CO decomposed to form a carbon layer hindering the CO adsorption. The wavenumber shift (after cool down 2077 cm^{-1}) could also be an indicator for creation of $Pt(CO)_x$ complexes [83], either due to surface restructuring or observed as an intermediate step in CO decomposition. Apart from that, there is still the possibility of an SMSI effect with zirconia covering the Pt surface and drastically reducing the number of adsorption sites. This effect is, however, very unlikely for a fully covering Pt layer and also unlikely at the rather low temperatures.

The same series of measurements was performed for the 50 cycle ALD film, depicted in Figure 5.6. The asymmetry of the peaks at low temperature is slightly different in comparison to the 250 cycle film. This may have two main reasons: On one hand the phase can be different for lower film thickness (giving rise to electronic effects of thin film geometry or support interaction), on the other hand, the peak intensity can be diminished while the non-resonant background stays the same, thus only the line shape would be changed due to the X_R/X_{NR} ratio (compare Figure 5.2). Similar to the 250 cycle sample this sample showed a line shape change at 275 °C, but it was less pronounced. This is due to the lower peak intensity prior to 250 °C and the larger asymmetry. Still the change was distinct and at the same temperature step. Furthermore, the change was again irreversible with temperature on cool down, as seen in the bottom black curve in Figure 5.6.

The fit values for the 50 cycle ALD film temperature series are shown in Table 5.2. The phase difference was comparable to the 250 cycle film while the resonance width was lower for values below 225 °C. The most unexpected finding was the resonance position which should have been red shifted for the rougher sample. The high wavenumbers are maybe due to the sputtering surface preparation used in Trieste, as opposed to our standard preparation, as the sputtering alters the surface structure. We observed the same trends as for the 250 cycle ALD Pt film for resonance width and phase difference with increasing temperature. However, the change in resonance position was almost negligible compared to the 17 cm^{-1} on the 250 cycle film. This is possibly again due to the surface structure influence of sputter preparation. The short sputtering is not that problematic for the 250 ALD cycle sample, as there is a thicker layer of Pt and after sputtering the sample is still similar. For the 50 ALD cycle sample sputtering has a more drastic effect due to the nanoparticle structure.

Table 5.2: Position, FWHM and phase of the CO resonances in the temperature series to 275 °C on 50 cycle ALD Pt.

50 cycle ALD	25 °C	75 °C	125 °C	175 °C	225 °C	275 °C	25 °C CD
Ω (cm^{-1})	2096	2095	2094	2093	2090	2086	2095
FWHM (cm^{-1})	5.1	4.9	6.0	7.9	9.1	16.2	14.4
Φ (rad)	6.14	6.09	6.40	6.5	6.5	6.82	6.82

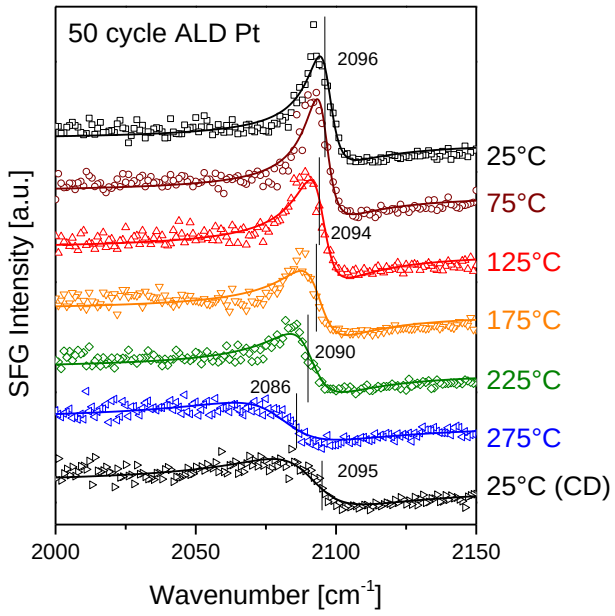

Figure 5.6: Temperature dependent in situ SFG spectra of the 50 cycle ALD Pt film. The gas pressure was 10 mbar pure CO. At the step from 225 °C to 275 °C a change in line shape for the CO was visible again. The bottom curve (black) was taken after cool down in CO showing the irreversibility of this feature.

This measurement was a first indicator that no SMSI effect was responsible for the signal changes as related effects should have been much stronger on the thinner film. Still the change seemed less pronounced on the 50 cycle film. Other explanations like CO dissociation on rougher films should also cause a stronger change on this thinner and (as seen in the TEM images) more particulate film. Nevertheless, the surface sputtering might have changed the structure of this particle film to cause this unexpected behavior.

To verify that the repeated observations are due to surface roughness and not caused by SMSI we prepared a roughened single crystal surface, i.e. we sputtered Pt(111) without the following annealing. The sputtered surface was prepared with the same sputter parameters as the ALD films. In Figure 5.7 the temperature series from room temperature to 275 °C is shown for this surface (left, defective) and for the same single crystal annealed at 800°C in UHV after sputtering (right, smooth). The curves show various differences, starting with intensities and peak asymmetries. Still, most important are the spectra at 275 °C, where the peak chance is observed for the roughened surface but not for the smooth surface.

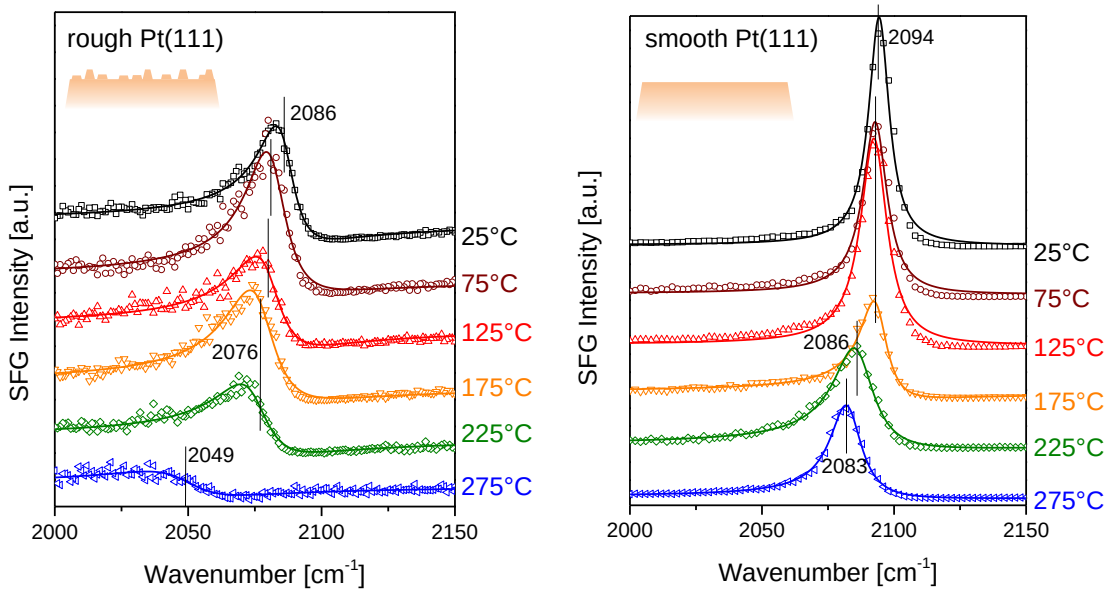

Figure 5.7: In situ temperature series to 275 °C on Pt(111) in 10 mbar CO. The left panel shows a freshly sputtered, therefore rough, surface; the right panel an annealed, therefore smooth, surface. The rough surface shows the strong change in line shape encountered with the ALD samples, while the peak on the smooth surface shows a typical behaviour of reduced coverage at higher surface temperature.

Table 5.3: Resonance position, width and phase of CO adsorbed on rough sputtered and smooth annealed Pt(111) surface for temperature series to 275 °C. in 10 mbar CO

Sputtered Pt(111)	25 °C	75 °C	125 °C	175 °C	225 °C	275 °C
Ω (cm^{-1})	2086	2081	2080	2077	2076	2049
FWHM (cm^{-1})	7.8	8.9	9.9	10.7	11.2	17.4
Φ (rad)	6.67	6.1	6.74	6.34	6.69	6.38
Annealed Pt(111)	25 °C	75 °C	125 °C	175 °C	225 °C	275 °C
Ω (cm^{-1})	2094	2093	2093	2093	2086	2082
FWHM (cm^{-1})	4.7	5.5	6.1	6.2	9.2	7.2
Φ (rad)	5.02	5.54	5.03	6.35	6.43	6.36

In Table 5.3 the resonance positions, widths and phase differences for the temperature dependent spectra of the rough and smooth surface are shown. The peaks on the rough surface are like the ALD samples rather asymmetric in comparison to the annealed surface peaks. This is like for the other samples due to different ratio in non-resonant background to peak intensity and different phase. The resonance width is also narrower on the smooth single crystal surface, showing that the CO adsorption layer is better ordered. As mentioned above, the most important finding was the recurring change in peak shape for the rough surface when heating to 275 °C, which was not present for the smooth surface. Therefore we conclude that this effect was indeed promoted by roughness and the ALD films exhibit natural roughness due to their particulate structure. As the Pt(111) is a single crystal, SMSI effects could be excluded after these measurements and the changes were attributed to CO dissociation, which has been reported in the literature for other stepped single crystals like Ru [84] and Ni [85], but which has been controversially discussed for Pt.

The goal of the discussed CO adsorption measurements was a better understanding of the basics of the CO oxidation reaction (i.e. the importance of adsorption properties of the surface). Therefore, it is crucial to know if the observed changes to the CO resonance have any influence during the actual CO oxidation reaction. As the reaction environment consists of a CO/O2 mixture like the one used to clean the samples after preparation, we tried heating in the same mixture after the change in line shape (i.e. after surface passivation by carbon from CO dissociation). For this, 20 mbar O_2 were added to the atmosphere of 10 mbar CO to get the same ratio that was used for most of the oxidation measurements shown later. With this gas environment the same temperature series was measured as with pure CO.

Figure 5.8 shows the temperature series up to 275 °C in CO/O_2 mixture on the used/C-poisoned 250 cycle ALD Pt sample, with the parameters described above. This

experiment was performed directly following the measurement shown in Figure 5.5 (temperature series in 10 mbar CO to 275 °C). The room temperature spectrum was not altered by the addition of O_2 to the gas atmosphere and the spectra did not change significantly from room temperature to 125 °C. Exceeding that temperature resulted in visible changes. At 175 °C a blue-shift and increased intensity could be seen for the CO resonance, indicating carbon oxidation. Further increase of the temperature changed the peak shape dramatically compared to the regular shape of CO resonances on Pt. The intensity was increased significantly and the phase difference changed. At the end of the experiment the signal was very similar to the initial CO signal in terms of line shape and intensity. The spectrum was also similar to CO adsorbed on the annealed Pt(111) single crystal at this temperature. In Table 5.4 the fitted resonance positions, widths and phases are displayed. All values were quite constant for the measurements up to 175 °C, where a slight increase of resonance position (3 cm^{-1}) could be found. A change could also be observed for phase and resonance width, both decreasing, as an ordered CO adsorption pattern was established (above 175 °C).

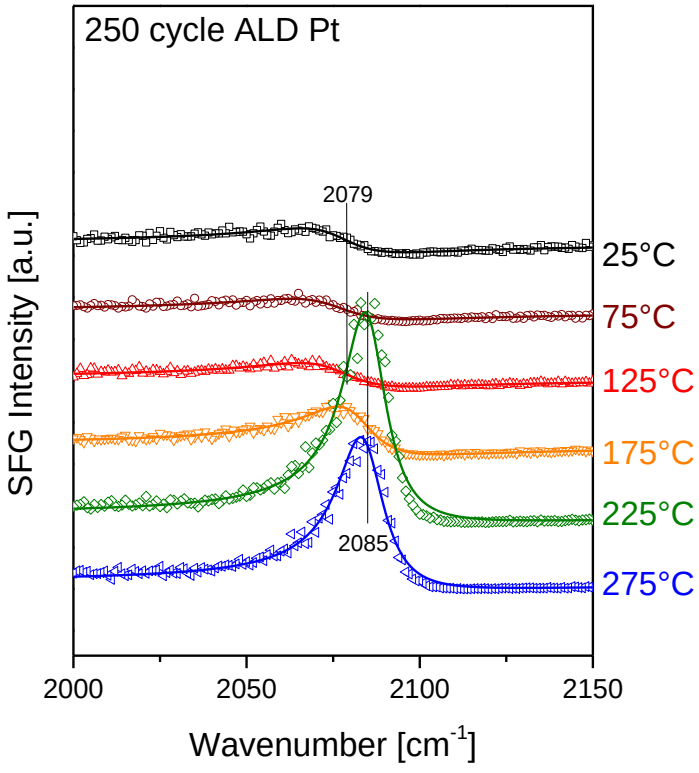

Figure 5.8: In situ temperature series in 10 mbar CO/ 20 mbar O_2 mixture on 250 cycle ALD Pt up to 275 °C, after heating in pure CO to 275 °C. Curves above 125 °C show a change back to regular CO on Pt resonance shape.

Table 5.4: Resonance position, phase difference and width for on-top CO on the 250 cycle ALD Pt film. Measurements performed in a CO/O_2 1:2 mixture with 30 mbar total pressure after previous heating in pure CO to the same temperature.

250 cycle ALD	25 °C	75 °C	125 °C	175 °C	225 °C	275 °C
Ω (cm^{-1})	2079	2079	2079	2082	2085	2085
Φ (rad)	6.69	6.79	6.71	6.38	6.0	6.13
FWHM (cm^{-1})	14.7	16.6	15.6	11.5	7.7	8.2

These measurements showed very well that we could recover the peak for CO adsorbed on the 250 cycle ALD Pt film. Comparing the measurements at 225 °C in pure CO and in CO/O_2 mixture showed that the peaks were very similar, with slightly lower linewidth and higher wavenumber. This indicates a slightly higher CO coverage of the surface in CO/O_2 mixture at this temperature.

The same heating measurements in CO/O_2 after the observed changes in pure CO were also performed for the used 50 cycle ALD Pt film and the used roughened single crystal. The spectra are plotted in Figure 5.9 and the fitted values of position, resonance with and phase difference are shown in Table 5.5. As before, a change back to a standard on-top CO on Pt resonance could be seen starting at 175 °C. The 50 cycle Pt film resonance did not shift much in the CO adsorption experiments and had therefore also almost no change in position for the CO/O_2 measurements. Only a slight increase in intensity connected with a decreasing resonance width and lower asymmetry were indicators for the recovery of the initial on-top CO peak. In comparison, the roughened Pt(111) single crystal resonance showed a stronger red shifted at the beginning and therefore also a stronger blue shift with increasing temperature could be observed. Furthermore, the change in phase difference was much stronger for the roughened single crystal surface. Again comparison with the respective measurements at 225 °C showed that the resonance was better localized (lower resonance width) in the CO/O_2 mixture. The results showed that O_2 promotes the adsorption of CO at temperatures below CO oxidation. The oxygen has a cleaning effect, freeing adsorption sites that are taken up by CO as these conditions favor adsorption of CO over oxygen. Furthermore, oxygen then inhibits spreading of carbon from dissociated CO from steps to terraces, stabilizing the CO coverage on terraces.

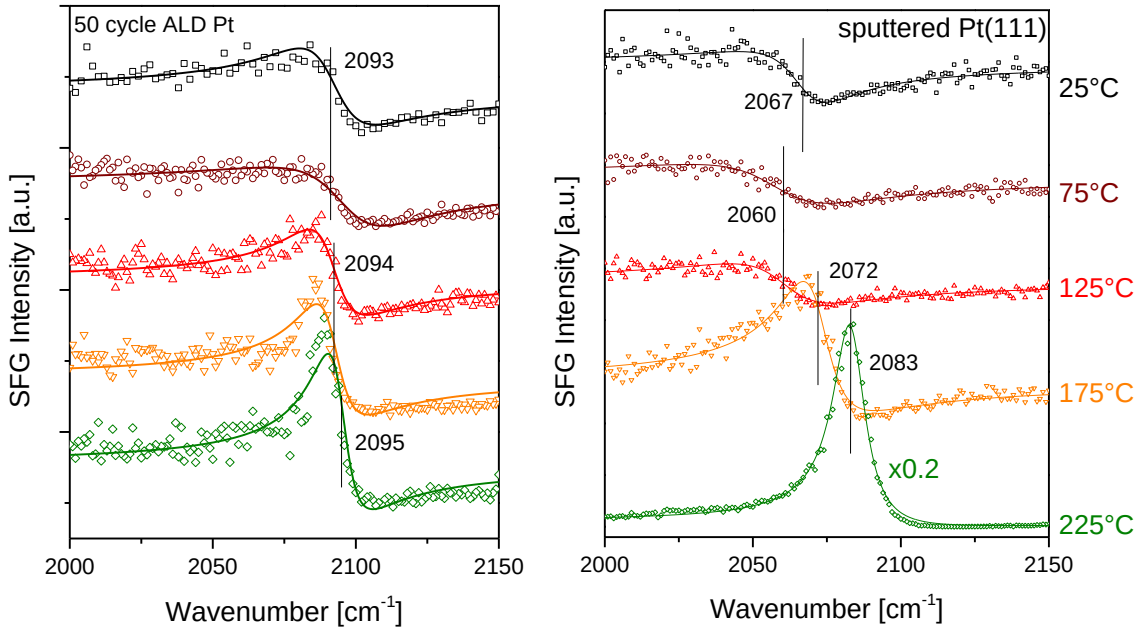

Figure 5.9: In situ temperature series from RT to 225 °C in CO/O_2 1:2 mixture (30 mbar total) for the 50 cycle ALD Pt film (left) and the roughened single crystal surface (right) after heating in pure CO to 275 °C. Above 125 °C again a change back to regular CO on Pt line shape can be observed.

Table 5.5: Resonance position, phase difference and width of CO in a 10 mbar CO/20 mbar O_2 mixture for the 50 cycle ALD Pt film and the rough single crystal surface after heating in pure CO to 275 °C.

50 cycle ALD	25 °C	75 °C	125 °C	175 °C	225 °C
Ω (cm^{-1})	2093.1	2093.6	2094.0	2094	2095
FWHM (cm^{-1})	12.8	18.9	9.8	8.5	6.4
Φ (rad)	6.70	6.82	6.73	6.78	6.38
Sputtered Pt(111)	25 °C	75 °C	125 °C	175 °C	225 °C
Ω (cm^{-1})	2067	2063	2060	2072	2083
FWHM (cm^{-1})	13.1	17.5	17.3	11.5	6.6
Φ (rad)	7.08	7.02	6.87	6.25	5.84

After systematic studies to unravel the reason for the strongly different temperature characteristic of the CO adsorption measurements in our lab we can reason that the change was CO dissociation. An SMSI effect can be ruled out as the effect was also present on a roughened single crystal. Surface contamination could be excluded by measuring on a different setup and by measuring single crystals, which showed a reversible behavior. Different desorption temperatures would not cause the irreversibility upon cooldown. CO decomposition in comparison would lead to the formation of a carbon layer, hindering standard CO adsorption and persisting upon cooldown on the metal surface. Such a layer can be removed by the addition of O_2 as

observed in the follow up measurements. It is possible that with the recovery of the CO peak CO dissociation is not influencing oxidation. The peak change was only observed in pure CO environment and the counteracting cleaning effect took over in the presence of O_2 already at temperatures below oxidation. Alternatively, the formed C may be rapidly reoxidized under reaction conditions.

5.3 CO Adsorption on Sputter Deposited Pt Samples

A second set of samples contained sputter deposited (SD) Pt on zirconia. These samples also featured different nominal thickness of 10 nm, 5 nm, 2 nm, 1 nm, and 0.7 nm. The amount of Pt should thus be comparable for the 10 nm SD and the 250 cycle ALD film.

A survey spectrum of the 2 nm SD film (Figure 5.10) was used to show that no significant contamination was present on the sample surface. The most prominent peaks belonged to the Pt binding energies of Pt 4f and Pt 4d electron shells. The zirconia support caused several Zr (3d, 3s) and an O 1s peaks. A distinct signal could also be seen for the carbon peak, which is the most common surface contamination of Pt [86]. In addition, a small peak at 400 eV is visible. This would most likely correspond to nitrogen, which may be a contaminant from storage in atmosphere. The survey did not reveal any other larger contaminations so the sample seemed well suited for the adsorption measurements.

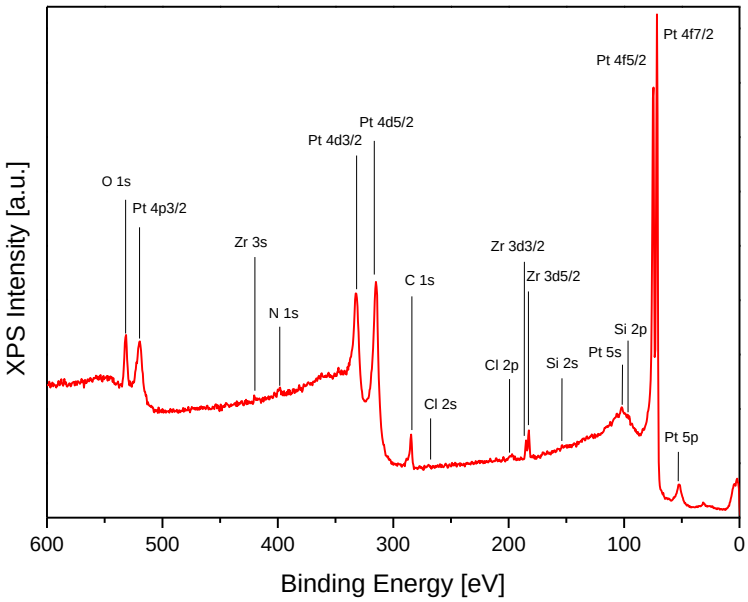

Figure 5.10: XPS-Survey of the 2 nm SD Pt film. Pt, Zr, O and Si are expected in the spectrum as they were part of the sample. C and N as well as part of the O-peak are contaminants from exposure to air.

For the SFG adsorption measurements the SD samples were pretreated in the same way as the ALD prepared samples. First oxidation in 5 mbar of O_2 at 300 °C, then change of gas environment to 5 mbar of 1:1 CO/O_2 mixture and cool down in this mixture to allow the adsorption of CO on the surface cleaned by the addition of oxygen.

Subsequently, measurements in 10 mbar CO were conducted. Depicted in Figure 5.11 are two measurements on the 2 nm SD Pt film (roughly correlating to the amount of Pt on the 50 cycle ALD film). The green spectrum was obtained first and showed an unexpected broad feature around 1950 cm^{-1} so a second spectrum (black) was acquired. The second spectrum did not show the feature at 1950 cm^{-1}, only the much narrower resonance at 2046 cm^{-1} that belongs to on-top CO. Compared to the resonance position of on-top CO on the ALD samples (around 2090 cm^{-1}) the peak position is strongly red shifted (implying adsorption at very low coordinated Pt sites) and the intensity is very low (poor signal to noise ratio). The broad peak in the first measurement is located in the bridging Pt region but the large FWHM of the feature hints to a very heterogeneous source. Its total absence in the second measurement might have been induced by the laser beam, as darker spots were found at the measurement locations (see Figure 5.11, right picture).

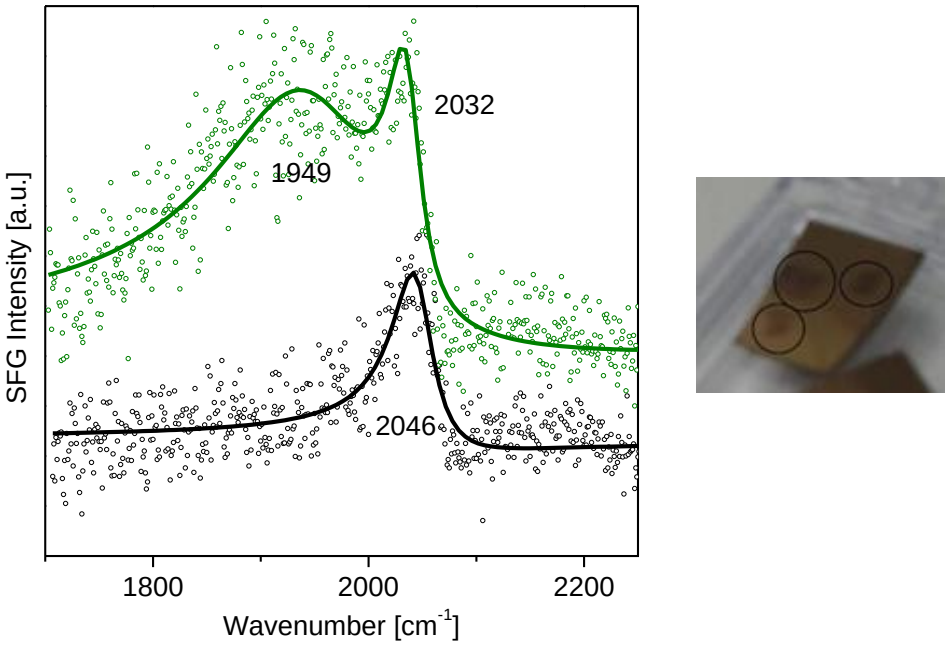

Figure 5.11: Room temperature SFG spectra of CO on 2 nm SD Pt film in 10 mbar CO. Green spectrum was taken after fresh preparation; black spectrum was taken directly after the first spectrum. On the right side a photo of the 2 nm sample with 3 damaged spots, highlighted by circles, is shown. The spots look darker than the pristine film.

CO adsorption was also investigated on a second sample, the 5 nm SD Pt film. Two spectra of this sample are shown in Figure 5.12. The back one is shortly after dosing 10 mbar CO and shows a large on-top CO peak, a second spectrum, in red, is after two hours of waiting time in CO environment. The lasers were turned off during this waiting time to rule out further influence from beam damage. The CO peak in the second spectrum is strongly diminished in intensity. A significant intensity loss was observed on the ALD samples when CO dissociation contaminated the surface. It is possible that CO dissociation also caused the change in signal of the SD Pt sample over two hours, as the peak position of 2071 cm^{-1} can be assigned to rough Pt and the results on our ALD films showed that rough surfaces promoted CO dissociation.

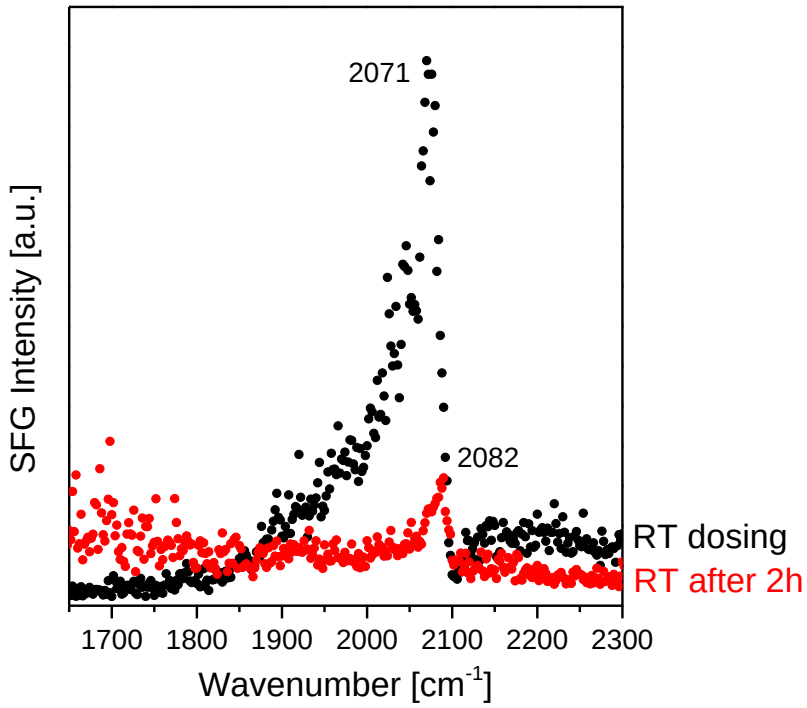

Figure 5.12: SFG measurement on the 5 nm SD Pt film in 10 mbar CO. The black curve is after CO dosing at room temperature, the red curve after 2 hours waiting time (without laser radiation) in the same gas environment.

Concerning the beam damage, we investigated which of the SFG beams caused the change of the sample. This was done by separately shining either visible or IR laser on the sample. This showed that the damage was induced by the infrared laser, which was already used with the lowest beam power possible. Some precautions had been taken prior to the measurements to prevent damage by the IR beam by moving the focus point 5 millimeters away from the sample surface and using relatively low laser amplification, risking power instability, so the beam damage could not be prevented by adjusting the beams. Still, we had not expected beam damage as there were no signs on the ALD

prepared samples of all thicknesses. Next, we investigated the damaged areas to determine sample usability for further measurements. SEM images of the samples were acquired with Karin Whitmore from the USTEM, and XPS studies were performed at the analytical instrumentation center of the TU Wien by Anette Foelske-Schmitz.

Figure 5.13 shows SEM images of the 2 nm SD Pt film. The left panel shows a region outside the damaged spot (pristine film), while the right panel shows the region inside the damaged spot. The pristine 2 nm SD film looked very uniform, while the damaged part had distinct bright and dark patches. There are different reasons for brightness in SEM. The strongest influence comes from the atomic number of the monitored elements and morphology [87]. Elements with high atomic number yield more secondary electrons and the coefficient for back scattered electrons is increasing almost monotonically with the atomic number. The morphology is important as it changes the trajectories of electrons, influencing their path to the detector. For surfaces tilted in the direction of the detector the brightness is generally higher, for surfaces tilted away from the detector the brightness is generally lower. The bright spots in our SEM image could therefore be due to higher accumulations of Pt and the dark spots are either regions without Pt or tilted away from the detector. We assume that the dark areas were uncovered zirconia with a far lower average atomic number than Pt, while the bright areas were Pt agglomerations. The Pt areas were very uneven causing additional contrast through topological changes. For better resolution an image with higher magnification was required but this was not possible for this sample due to focusing (charging) issues.

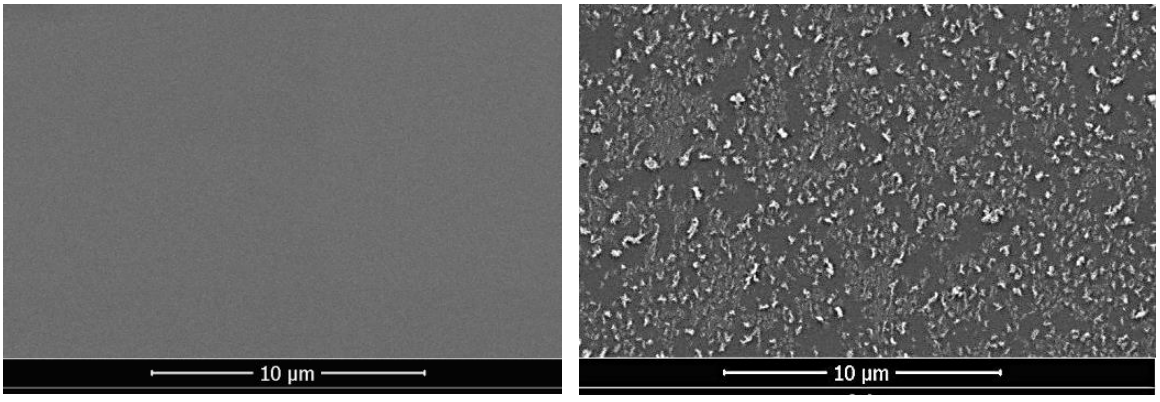

Figure 5.13: SEM image of the 2 nm SD Pt film. On the left side an area without beam damage is depicted featuring a uniform Pt film, on the right side an area with beam damage is depicted with very agitated coloring that hints to changes in the structure of the Pt film exposing the zirconia support.

Nevertheless, the same beam damage also occurred on the 5 nm SD Pt film (used in the SFG measurement shown in Figure 5.12). Thus this film was analyzed with SEM and the thicker Pt layer yields enough conductivity to circumvent the charging issues. Figure 5.14 depicts the damaged area at the magnification as for the 2 nm film. Again, structured Pt somehow agglomerated uncovering the darker zirconia. It looked like the Pt film was peeling off the surface in ribbons. The brightest parts of the image were curled up sides of the remaining Pt sheets. This explains the patterns observed also for the 2 nm SD film with small curled up Pt parts that uncovered dark zirconia patches. The features were smaller on the 2 nm Pt film because the Pt film was thinner.

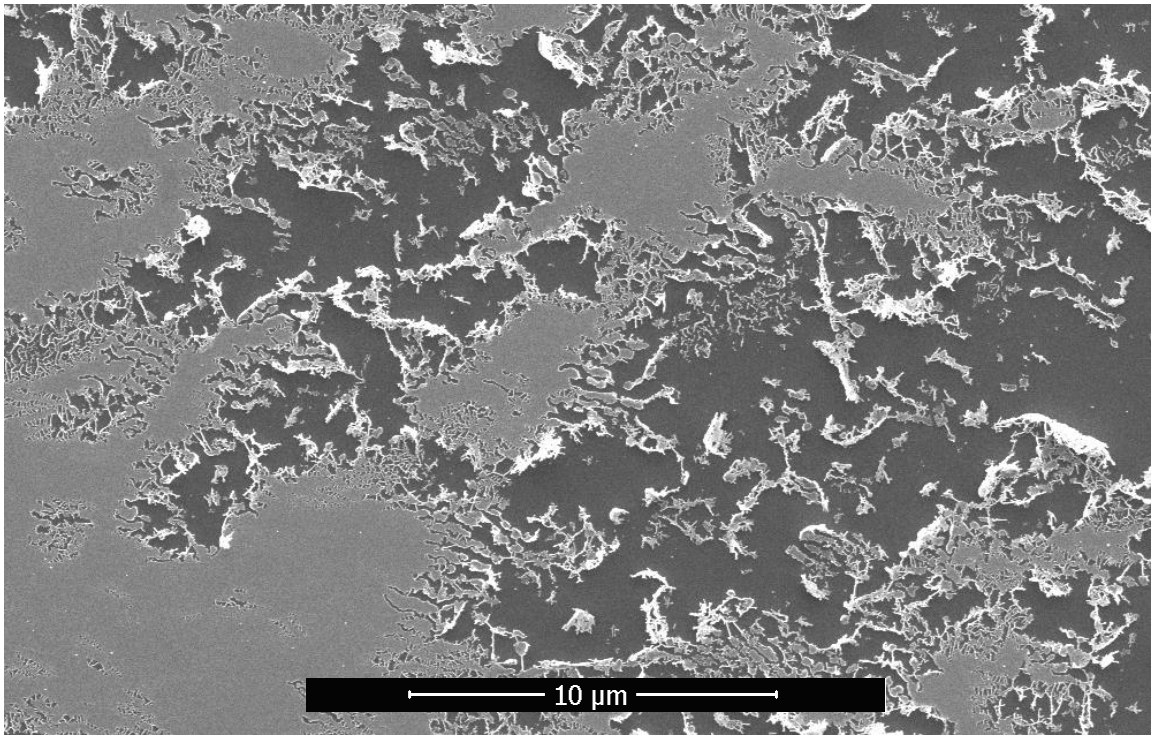

Figure 5.14: SEM image of the 5 nm SD Pt film. The brighter structures correspond to the Pt while the darker uniform part is the zirconia support. Pt seems to curl up in ribbons.

Due to the good conductivity of the 5 nm SD sample we could use higher magnification. The results are shown in Figure 5.15 for the pristine film (left) and the damaged area (right). The pristine Pt looked uniform with brighter and darker spots corresponding to a particle/grain-like structure with small height differences and tilted surface facets. The damaged area showed bright Pt flakes and strings on dark zirconia. Brightness changes within the Pt structures are mainly from topological changes. This detachment of Pt from the support indicates insufficient sticking of Pt to the zirconia support material.

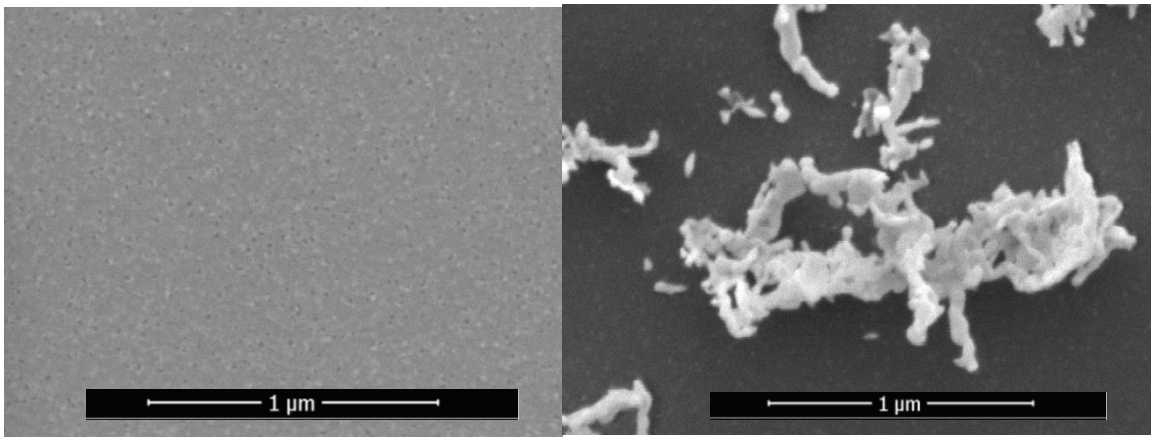

Figure 5.15: SEM image of the 5 nm SD Pt film. On the left side the pristine Pt surface is shown with grain structure. On the right side a damaged spot after SFG measurement can be seen with Pt curling up.

To supplement the SEM images, spatially resolved XPS spectra were acquired. At the analytical instrumentation center of TU Wien, it is possible to perform area resolved XPS for a spot of 2 µm diameter using a monochromatic Al Kα source. The area resolved measurements allowed us to compare the damaged spot to the undamaged film. Additionally, angle resolved detection allowed depth profiling. The XPS analyzer was therefore equipped with a lens to only measure electrons from specified exit angles over a range of 60 °. Depending on the mean free path of the electrons in the sample, angle dependent measurements are more or less surface sensitive. Large angles to the surface normal increase the path the electrons have to travel through the material. It is therefore less likely that electrons from lower layers leave the material and such measurements are more surface sensitive.

Figure 5.16 shows Zr 3d spectra of the 2 nm SD film from angle resolved XPS measurements. The left panel shows spectra on the pristine film while the right panel shows spectra on the damaged part. We evaluated the binding energies of the Zr peaks. For pure metallic Zr the binding energy would be 179 eV for $3d_{5/2}$ [88]. In comparison, we had Zr $3d_{5/2}$ at 182.2, which perfectly correspond to ZrO_2 [88, 89]. For depth profiling we used the capability of the analyzer to measure different escape angles between 20 and 80 °. The black curves correspond to the smallest angle to the surface normal (20°), i.e. electrons have the shortest path through the sample, and the green curves correspond to the largest angle (80°). Spectra in-between change by 15° per measurement. The first difference between the two measurement spots was the poor signal to noise ratio for zirconia below the pristine SD Pt. This was due to the very low signal intensity because the zirconia was fully covered with Pt. This became especially clear with the high angle measurements as for very surface sensitive spectra the

zirconium signal vanished. The zirconia peaks of the beam-damaged area were only slightly decreasing proving that our assumption with curled up Pt and uncovered zirconia from the SEM images was correct. In addition, a slight shift of the peak positions could be observed but this was most likely due to the insulating nature of ZrO_2, which could have led to sample charging effects [43].

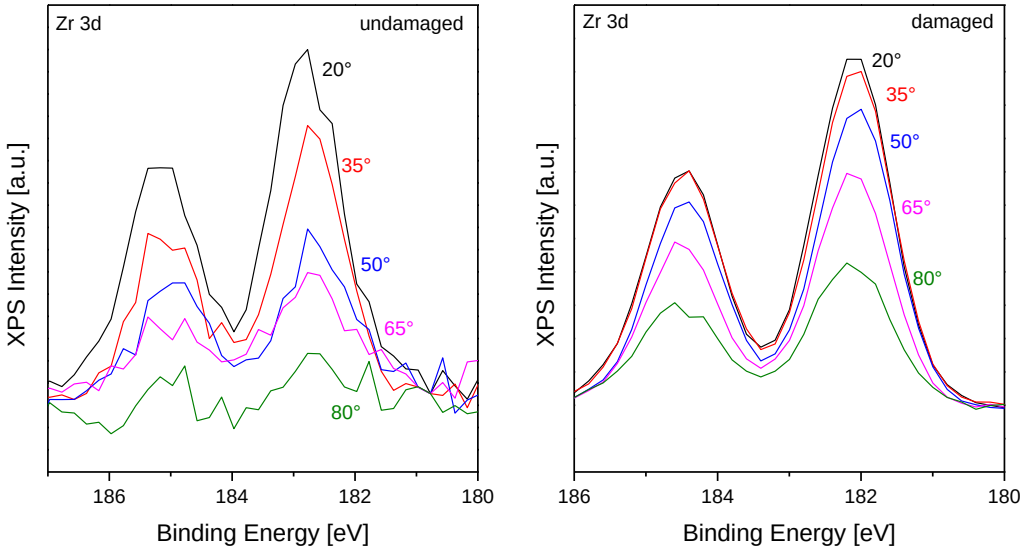

Figure 5.16: XPS measurements of Zr 3d in UHV of the 2 nm SD sample. The left panel shows angle resolved measurements on the undamaged film, while the right panel shows angle resolved measurements on a beam damaged spot. For the undamaged part the Zr 3d intensity was lower because the Pt film was covering the zirconia, causing a signal near zero for the most surface sensitive measurement. For the damaged film the peaks are much more intense because the Pt film exposed zirconia. Even the more surface sensitive measurements still showed distinct peaks.

Figure 5.17 shows the C 1s spectra for the measurements at 20° for the damaged and undamaged surface after CO adsorption. The peak at 284.8 eV (blue) is the standard peak for graphitic carbon [90]. The peak at 286.5 eV (red) is from adsorbed CO [91, 92]. The feature at 288.5 eV (orange) belongs to some higher oxidized compounds, explaining the large linewidth. Most noticeably, on the damaged film an additional peak is required to fit the XPS spectra located at 285.3 eV and the intensity of the CO peak is strongly diminished. The lower CO signal correlates well with our SFG results.

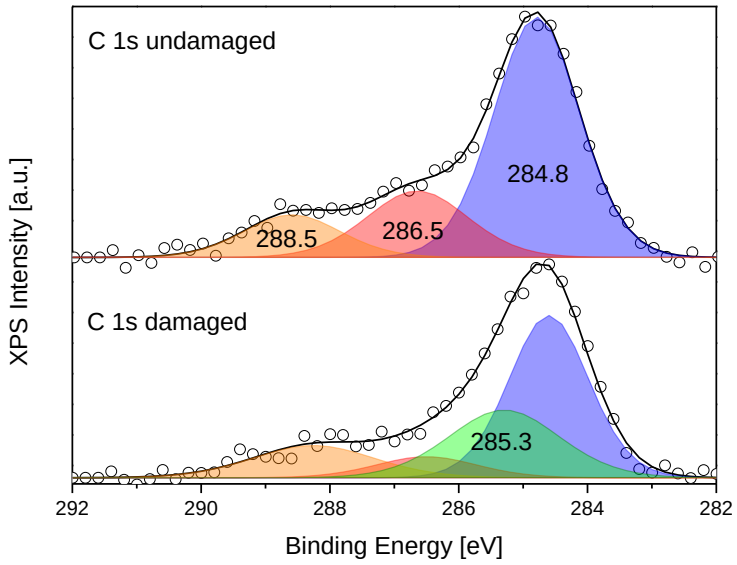

Figure 5.17: XPS measurement of C 1s core level. Comparison between un-damaged and damaged area on 2 nm ALD sample is shown. The red peak at 286.5 corresponds to adsorbed CO and has much less intensity for the damaged spot.

In summary, combining SEM and XPS measurements we found that Pt was not properly sticking to the ALD zirconia substrate upon Pt sputter deposition. The IR beam of the SFG process locally heated the surface and Pt detached from the zirconia and agglomerated. This effect renders these samples unsuitable for model catalyst measurements, as the model catalyst structure needs to be homogeneous and controllable/predictable. We also wanted to design model catalysts to investigate metal/support interaction, which is impossible if the metal detaches. Furthermore, future experiments should focus on nano particle structured metals, which are not stable due to the agglomeration of Pt observed for the SD films. These samples were therefore not investigated further and CO oxidation measurements were only conducted on the ALD prepared Pt films.

5.4 Polarization Dependent Spectroscopy of CO Adsorption

A powerful feature of SFG is the possibility to carry out polarization dependent measurements. In chapter 5 all spectra shown were taken in ppp polarization except for Figure 5.1, as the ppp spectra are stronger than ssp spectra for flat metal surfaces. This is due to the bond orientation of on-top CO parallel to the surface normal. The comparison between ssp and ppp signals can yield information about surface roughness, as for rougher surfaces facets should be tilted from the macroscopic surface normal and cause the respective adsorbed CO to be tilted likewise. Those CO molecules perpendicular to a facet, but tilted from the macroscopic surface normal contribute to the ssp signal (Figure 5.18).

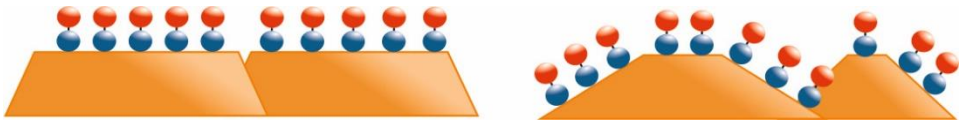

Figure 5.18: Molecule bonds are oriented orthogonal to the surface. For flat surfaces they are parallel to the surface normal, for rougher surfaces molecules are tilted with respect to the macroscopic surface normal causing an ssp signal in the SFG measurements.

To prove that the ssp spectra indeed depend on the surface roughness, different ALD samples were examined and the SFG spectra compared. The obtained spectra are shown in Figure 5.19. The curves for 750 and 250 cycle films are quite similar, with the peak positions matching within accuracy. In comparison, the 50 cycle Pt film had higher intensity and a larger peak asymmetry. Both changes hint to a difference in film structure, with CO tilted away from the sample surface normal. The increase in ssp intensity is especially noteworthy as we saw a larger decrease in ppp intensity for the 50 cycle film compared to the 250 cycle film. For the 10 cycle ALD cycle Pt film, which is not continuous but consisting of single particles, two resonances were present and the intensity was again lower. The two resonances were explained by the further structural change, offering different adsorption sites. One peak (2085 cm^{-1}) was at the same wavenumber as the resonances on the thicker films and should therefore correspond to "standard" Pt (terrace) sites. The other resonance was at much lower wavenumbers (2056 cm^{-1}) and may correspond to very low-coordinated Pt or even to Pt at metal-support interfaces. This corresponds well with the TEM results, which showed that the 10 cycle film has distinct particles, while the thicker films start to combine particles to build a closed layer. In addition, the overall ssp intensity of the 10 cycle film is again lower than the intensity of the 50 cycle film. This is due to the lower amount of Pt sites

available for CO adsorption on this particle film. The direct comparison of ppp and ssp signals for the 250, 50 and 10 cycle samples is shown in Figure 5.20. This comparison highlights the change in I_{ppp}/I_{ssp} ratio from closed film to particle film.

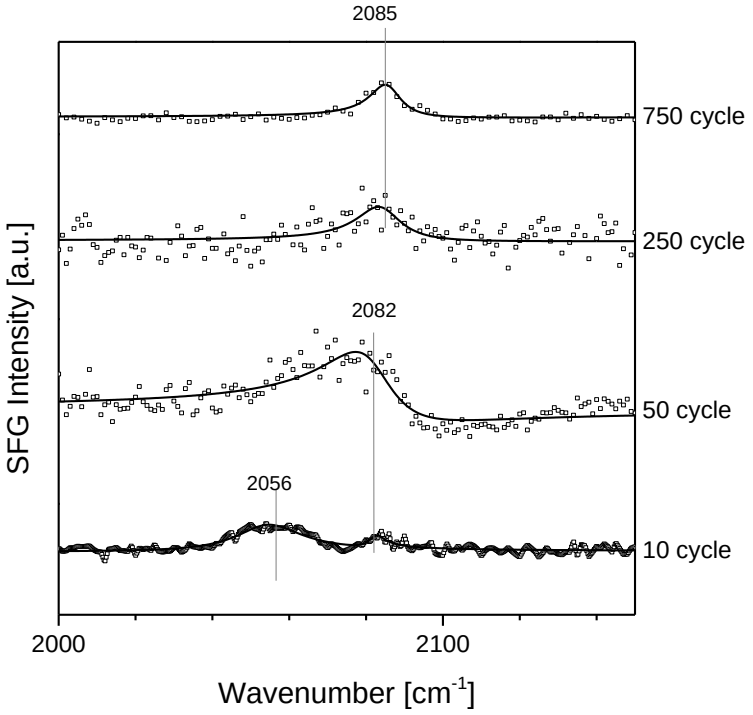

Figure 5.19: SFG spectra in ssp polarization for CO adsorption in 10 mbar CO at 200 °C on different ALD Pt samples.

Nevertheless, even for the thinnest ALD films the ppp signal was still significantly larger than the ssp signal. Concerning simulations of the I_{ppp}/I_{ssp} ratio for CO on Pt [70] the lowest ratio for angles over 80° would be roughly 2. In our case, ratios were indeed low as denoted in table Table 5.6, indicating a significant tilt of facets due to the particle structure of Pt for films with few deposition cycles. In addition, the slightly higher ratio of the 10 cycle film compared to the 50 cycle film (3.4 vs 2.4) matches the TEM images, in which the Pt particles of the 10 cycle film were shaped more like pyramids with less tilted side facets.

Table 5.6: Intensity ratio of ppp to ssp signals for the on-top CO peaks of different ALD Pt samples.

	250 cycle	50 cycle	10 cycle
Ratio I_{ppp}/I_{ssp}	17.4	2.4	3.4

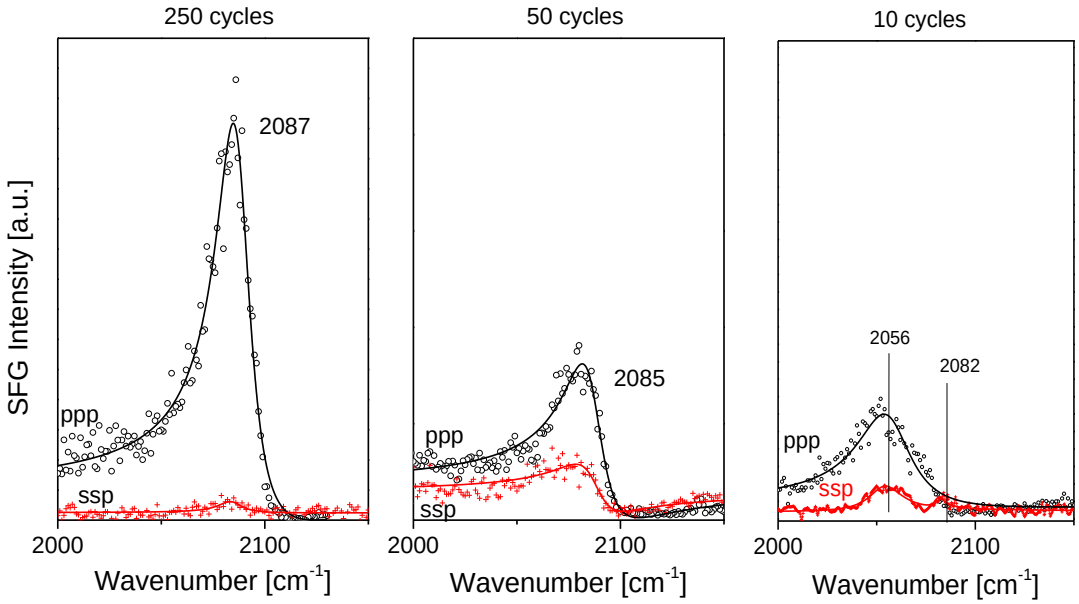

Figure 5.20: SFG spectra of 250, 50 and 10 cycle ALD Pt films for comparison of ppp and ssp signals. Measurement temperature was 150 °C for 10 mbar CO.

6 CO Oxidation Measurements

In the two previous chapters, a thorough characterization of the ALD model catalysts and CO adsorption in pure CO environment was presented. The insights gained in these studies are the basis for the interpretation of SFG spectra in mixed CO/O_2 atmosphere during CO oxidation reaction. Still, for catalytic measurements a simple study of adsorbates solely by SFG is not sufficient. To correlate spectral changes to reaction processes we need to monitor the amount of educts and products. Therefore, we used a mass spectrometer (MS) to check the gas composition during the catalytic measurements. We could then link changes in adsorbates directly to changes in the gas atmosphere. In our setup we used a mass spectrometer from Pfeiffer Vacuum with Faraday detector to monitor CO, O_2 and CO_2 to follow the reaction, and Ar to calibrate pressure and detection sensibility drifts over time. In the following part examples of MS measurements upon temperature steps for SFG spectra and the influence of partial pressure will be described. Afterwards, reaction measurements on the ALD films will be discussed, focusing especially on the 250 and 50 cycle Pt films.

SFG spectra take some time depending on the precision/resolution of the measurement. The shortest SFG scans roughly take 5 minutes, but for low signal intensities 20-30 minutes may be necessary. Related MS measurements are plotted versus time with the respective temperature steps also indicated in the same graph for better correlation. As the measurement chamber is a batch reactor, the duration of temperature steps can slightly influence the activity e.g. by changing the gas ratio and therefore the reaction equilibrium over time. Especially long SFG spectra might have an influence, thus some complementary measurements without simultaneous SFG acquisition but with a constant temperature ramp were also recorded. In that case the time could directly be converted to sample temperature and the MS signal could be plotted versus temperature.

Figure 6.1 shows an example of the correlation of reaction temperature and mass spectrometer signal for a mixture of 10 mbar CO and 10 mbar O_2. The large difference in signal intensity of CO and O_2 is apparently not due to the difference in partial pressure (as the partial pressures are the same) but indicates different detection sensitivity (partially influenced also by molecular fragmentation). For the shown system the on-set of CO_2 production started at the 250 °C temperature step, but the increase in CO_2 was almost negligible. The incline can be observed better in Figure 6.2, which is a detailed plot of the CO_2 MS signal for temperature steps of 250 to 300 and 350 °C. It highlights that with increasing temperature the material activity increased as the rise was steeper

at higher temperatures. All in all, the MS data allows following the reaction qualitatively with temperature, but for quantitative results MS detection would need to be calibrated for the different gases.

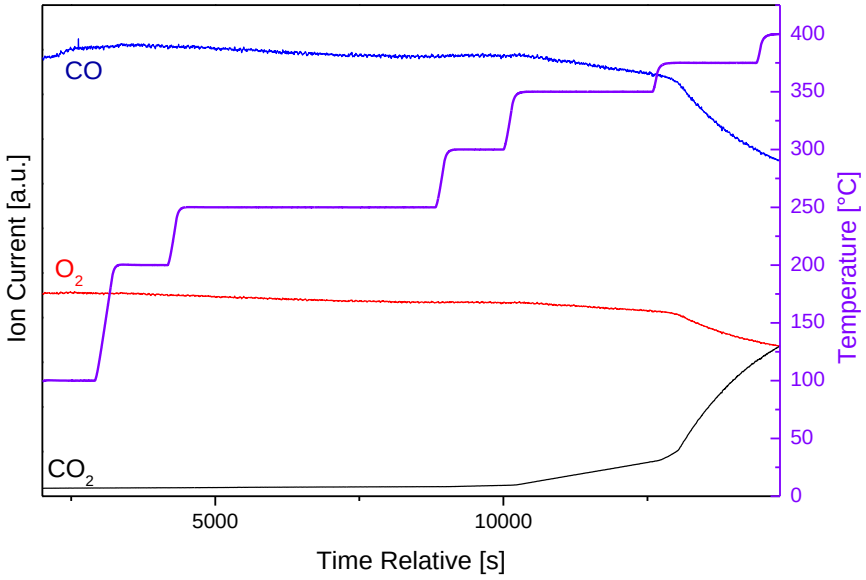

Figure 6.1: Mass spectrometer data and temperature plotted vs time for a 2 nm SD Pt film in 10 mbar CO and 10 mbar O_2 mixture. Shown are the ion currents for the educts of CO oxidation, CO and O_2, and the product, CO_2.

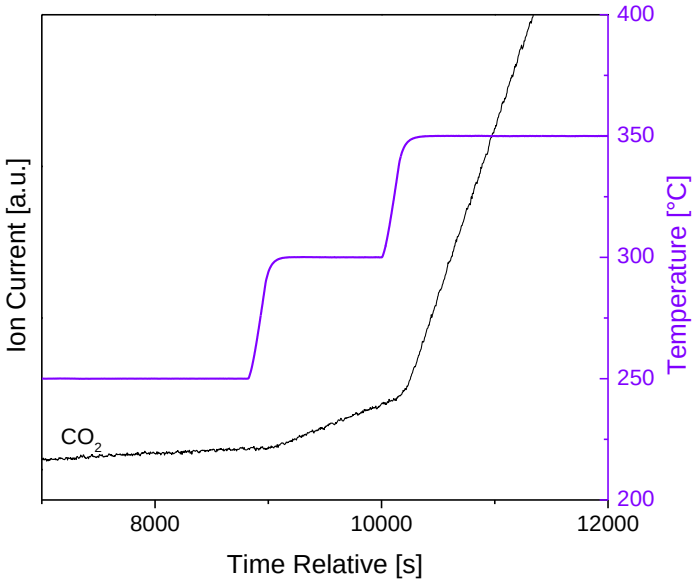

Figure 6.2: Zoom on CO_2 mass spectrometer signal between 250 °C and 350 °C for the above data. This zoom shows that already at 300 °C an increase in CO_2 can be observed.

The partial pressures of CO and O_2 are important for the catalytic reaction because they are responsible for the reaction equilibrium and surface coverage (i.e. surface poisoning by CO at low temperatures and high CO pressure [93]). Figure 6.3 shows the influence of

different ratios of CO and O_2 on the SFG spectra with the left panel displaying spectra for a 1:2 mixture of CO and O_2 (oxygen excess) and the right panel displaying a 2:1 mixture of CO and O_2 (stoichiometric mixture for CO oxidation) with a total pressure of 120 mbar. The experiments were conducted on the 750 cycle ALD Pt film (i.e. bulk sample). Heating in CO/O_2 mixture shifts the peak position due to the lowering CO coverage upon thermal desorption (as observed in CO adsorption measurements in chapter 5.2), but the surface remains CO poisoned and inactive. For the oxygen excess the wavenumbers of the CO resonance were somewhat lower than for the stoichiometric mixture, due to lower CO coverage with lower partial pressure. The most important difference is the disappearance temperature of the CO signal. At 400 °C no surface CO could be detected by SFG for the oxygen excess case while there was still CO on the surface at the same temperature for the stoichiometric mixture. To facilitate the oxidation reaction and to ensure that the surface fully changed from CO poisoning to oxygen coverage, the following experiments were thus conducted with O_2 excess mixtures of a 1:2 CO/O_2 ratio.

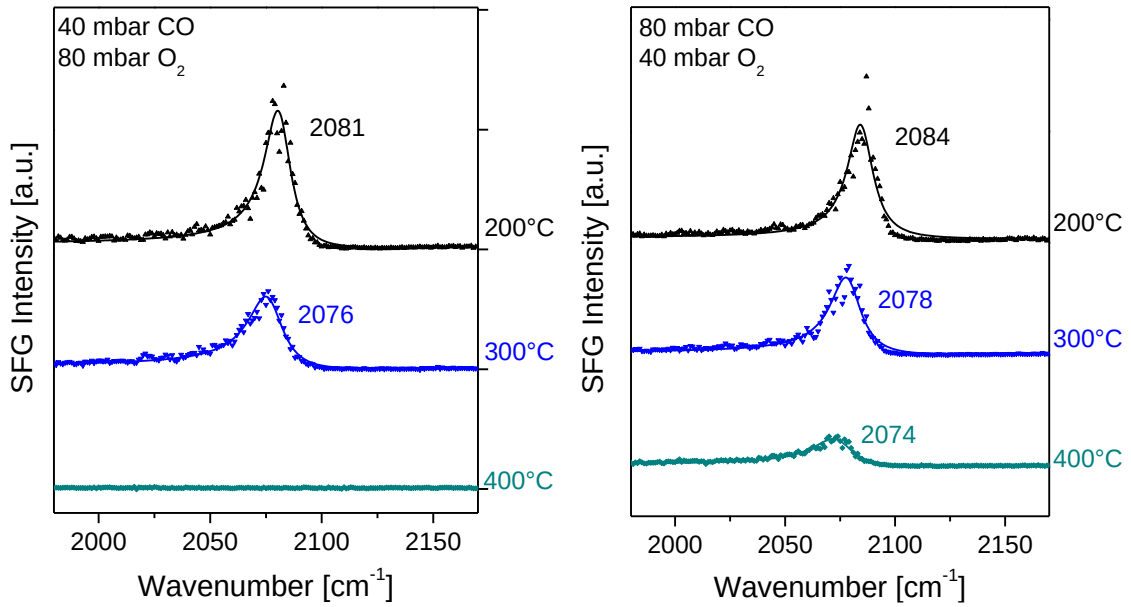

Figure 6.3: In situ temperature dependent SFG spectra for bulk like 750 cycle ALD Pt film. Left panel shows data for 40 mbar CO and 80 mbar O_2 mixture. Right panel shows data for 80 mbar CO and 40 mbar O_2 mixture. For the oxygen excess, no adsorbed CO peak can be found at 400 °C while for the stoichiometric mixture some CO remains bound to the surface at this temperature.

6.1 Operando SFG Spectroscopy

For the operando studies, which are in the focus of this thesis, the ALD films with 10, 50 and 250 deposition cycles of Pt were systematically investigated. Furthermore, some measurements on the 5 and 125 cycle samples were added to emphasize trends. All of the following SFG CO oxidation measurements were performed in an oxygen excess gas mixture of 1:2 CO/O_2 at a total pressure of 30 mbar.

Figure 6.4 shows the spectra for the 250 cycle ALD Pt film from 150 to 400 °C. Prior to the SFG measurements, several cycles of CO oxidation were performed to assure that the surface was clean and the measurements reproducible. The on-top CO peak was located at 2091 cm^{-1} for the first temperature step of 150 °C. Heating caused the resonance to redshift to lower wavenumbers. Exact values are denoted in Table 6.1. This is, as mentioned before, a sign of reduced surface coverage, which results from thermal desorption. At 400 °C, the CO resonance was not visible any more, meaning that the surface fully switched from CO coverage to oxygen coverage. CO oxidation requires oxygen coverage of the active facet, as CO poisons the surface and hinders the process [93]. The switch in coverage at 400 °C corresponded to the strong increase in CO_2 formation seen in the MS data.

Table 6.1: Resonance position and intensity of on-top CO peaks for different temperatures. in reaction mixture 10 mbar CO, 20 mbar O_2.

250 cycle	150°C	250°C	350°C	375°C	390°C
Ω (cm^{-1})	2091.3	2088.9	2081.6	2080.5	2080.1
FWHM (cm^{-1})	5.9	6.8	8.4	8.3	9.2

One big question that remained was why the CO_2 production started well below the major 400 °C step, at which CO was no longer poisoning the surface. A co-adsorption of oxygen and CO in the form of intermixed layers is not possible and oxidation only occurs after the coverage has changed. Nevertheless, a measureable increase in CO_2 was observed in the MS data already at the 350 °C temperature step, when surface CO was still present. There was also a slightly larger red shift in the SFG spectra when heating from 250 to 350 °C than for any other steps. This effect may be explained by the surface structure of the ALD film. As seen before in TEM, the film is composed of single crystal grains that grow together to form a closed film. It is safe to assume that this film consists of different facets with varying crystal terminations.

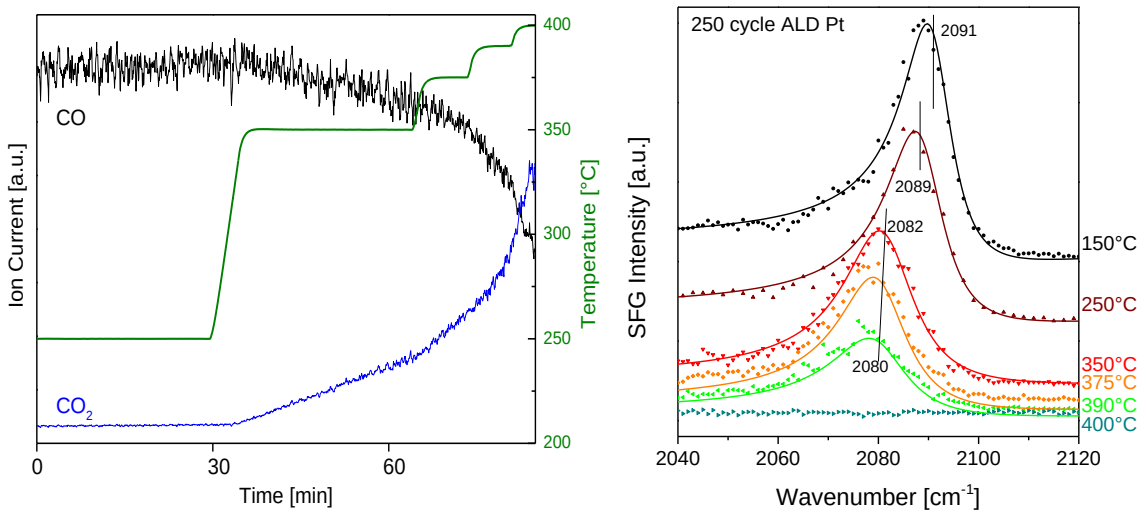

Figure 6.4: Mass spectrometer data and in situ SFG spectra of CO oxidation on 250 cycle ALD Pt in 10 mbar CO and 20 mbar O_2. The left panel shows the mass spectrometer data and temperature curve in dependence of passing time. The right panel shows the SFG spectra corresponding to the temperature plateaus. A red-shift of the peak position is seen when the first increase in CO_2 pressure is visible.

In general, different crystal terminations have different catalytic properties. CO oxidation on Pt at low pressure has been reported in the literature using photo-emission electron microscopy (PEEM) [94]. Using a polycrystalline Pt foil, it was shown that at a CO pressure of 10^{-5} mbar the temperature of switching between CO and oxygen coverage differs for almost 100 K for the 110 and 111 termination. Compared with our SFG measurements, when no CO was present above 400 °C (all facets oxygen covered) the first facets might have switched coverage already around 300 °C. These facets may have catalyzed CO oxidation at lower temperatures while the remaining CO still poisoned facets and contributed to the SFG signal. This may also be responsible for the larger red shift of the CO peak with the temperature step from 250 to 350 °C. Different facets have slightly different binding energies and the measured spectra are mostly a median of the different peaks and after some surfaces stopped contributing to the CO signal, the peak is centered more at different wavenumbers. According to the PEEM measurements, the 110 domains are first to switch coverage. Measurements on single crystals comparing the wavenumbers of adsorbed CO found that the adsorbates on 110 domains are located at the highest wavenumbers [95]. Their desorption at temperatures between 250 and 350 °C perfectly matched the overall signal red shift in our SFG results. Overall the gradual activation of different facets for CO oxidation is a suitable explanation for our results.

The same SFG temperature series has been recorded for the 50 cycle ALD Pt film, shown in Figure 6.5. For this film, the CO peaks were at lower wavenumbers than for the smoother 250 cycle film, as summarized in Table 6.2. This matches our adsorption measurements, when CO on rough surfaces (i.e. films with fewer deposition cycles) was redshifted in comparison to CO on smooth surfaces. Again, a red shift with increasing temperature was observed but contrary to the 250 cycle film, the CO peak did not vanish at 400 °C, but only at 450 °C. This indicates that the oxidation was also "delayed" as the CO poisoning persisted up to higher temperatures. The conclusion was therefore that the particle film was less active for catalyzing CO oxidation than the smoother bulk film.

Table 6.2: Resonance position and intensity for the 50 cycle ALD Pt temperature dependent spectra in oxidation environment of 10 mbar CO and 20 mbar O_2.

50 cycle	150°C	250°C	350°C	375°C	400	425
Ω (cm^{-1})	2080.9	2080.2	2076.7	2075.6	2075.5	2073.7
FWHM (cm^{-1})	10.2	10.2	9.5	9.3	8.8	9.6

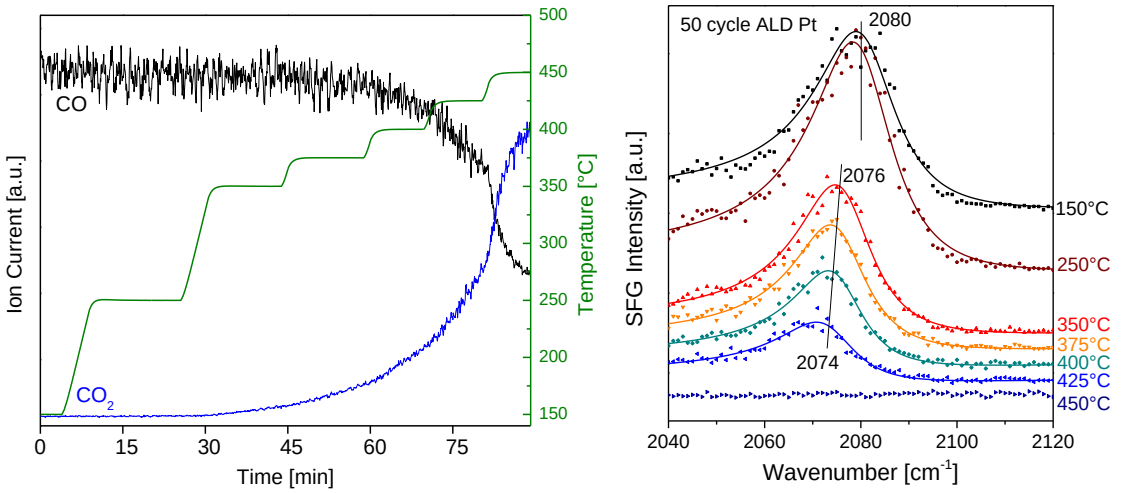

Figure 6.5: Mass spectrometer data and in situ SFG spectra for CO oxidation in 10 mbar CO and 20 mbar O2 on the 50 cycle ALD Pt film. The decrease of CO and increase in CO_2 for higher temperature is shown in the left panel, while the SFG spectra corresponding to the temperature steps are shown in the right panel. Again a red shift was observed above reaction on-set temperature. The resonances were at lower wavenumbers than for the 250 cycle film.

This finding was quite unexpected, as, for various reactions, it had been reported in the literature that smaller/rougher particles were generally more active than smoother films/bulk. The next steps were therefore to investigate if the results were reproducible

and if they were affected by the rather high laser intensity. Afterwards it was examined whether the lower activity was specific to this sample or a trend for all samples with few deposition cycles.

To confirm that the reaction results were reproducible and whether there was any influence of the laser beam, repeated measurements with linearly ramped temperature were performed. Both previously discussed samples (250 and 50 cycle) were investigated. The initial gas phase again consisted of a 1:2 mixture of CO/O_2 with 10 mbar CO and 20 mbar O_2. Alternatingly, the SFG lasers were on or off for each ramping cycle, with a ramping speed of 20 °C/min for the temperature increase. Figure 6.6 shows MS data for two temperature cycles with laser off (top 1 & 3) and laser on (top 2 & 4), both for the thicker ALD film and for the thinner film. For temperatures below ignition (seen as a kink in the spectra) the curves were identical for all cycles on one sample.

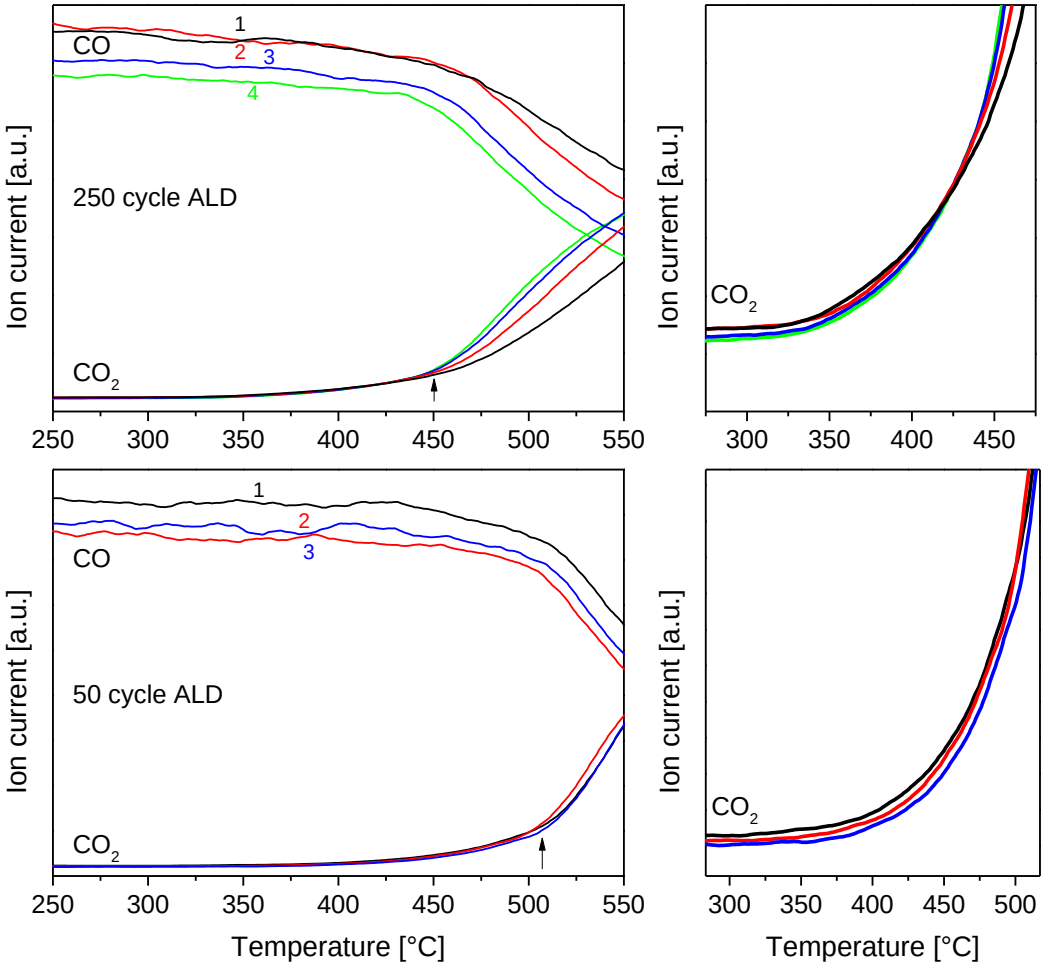

Figure 6.6: Mass spectrometer data for multiple cycles of CO oxidation on 10 nm and 2 nm ALD Pt in 1:2 mixture of CO/O_2 (total pressure 30 mbar). The right panels are zoomed on the temperature at which CO oxidation starts. The measurements are alternating between temperature ramp with SFG lasers off (1,3) and SFG lasers on (2,4).

This can be seen better in the magnified displays on the right side. For temperature above the ignition kink the curves slightly differed for the thicker sample. Apparently, multiple cycles of oxidation increase its catalytic activity above ignition. Nevertheless, the laser radiation does not seem to have any influence on the catalytic reaction. The ignition temperature remained the same for all cycles, no matter if the lasers were on or off. The change in activity for the 250 cycle sample above ignition was also visible in the third curve with radiation off. It is also important to mention that the position of the kink was at slightly higher temperatures than the disappearance of CO in the spectra. This is in part due to delayed gas information at the MS. With a ramp of 20 °C/min, a small delay can have a significant influence on the measurement. In our setup the MS is connected to the high pressure chamber by 50 cm long steel tubing and a leak valve to ascertain a maximum pressure of 10^{-5} mbar in the MS. The distance is no problem for the SFG measurements, as the measurements were started 1-2minutes after reaching the set temperature for a step. Yet, for the fast ramp the tube length may influence the correlation of data. In addition, the gas volume of the chamber is large compared to the sample. The measurements are performed without a circulation pump so the insufficient gas mixing also contributes to the time delay. Therefore it is possible that the ignition kink in the ramping experiments is actually at lower temperatures than the one seen in the MS data (comparable to when CO vanished in the SFG spectra).

The MS ramping experiments showed that the activity of the thinner rougher film remained lower than that of the smoother film. The question remains if this is a general trend for films with fewer deposition cycles or a specialty of the 50 cycle film. Therefore, the temperatures at which CO was fully removed from the surface were measured also for the 125 cycle and 10 cycle ALD Pt films. The resulting temperatures for all measurements are denoted in Table 6.3. The measurements prove that the change in temperature for CO to O coverage switching was connected with the number of deposition cycles: the fewer the deposition cycles, the higher the temperature. The main difference observed before for films with fewer deposition cycles was the higher roughness compared to the smoother thicker films. Therefore, the increased temperature was most likely linked to the higher surface roughness. More precisely, higher roughness means higher number of step sites that bind CO differently than terrace sites. The thicker films have more terrace sites where CO is weaker bound to the surface, while the thinner films with more particles have more step sites where CO is stronger bound to Pt. Terrace sites have been reported to be favored in CO oxidation [96]. So this may have some impact on our results. Nevertheless, rougher surfaces also bind oxygen stronger and are typically considered more active

Table 6.3: Temperatures of disappearance of CO resonance in SFG spectra for different film thicknesses.

ALD Pt cycles	No peak in SFG (°C)
250	400
125	425
50	450
10	475

To complement the temperature dependence table of CO disappearance, Figure 6.7 shows the CO peak positions during reaction of the various Pt ALD films for lower temperatures at 150, 250 and 350 °C. Again a monotonous behavior is observed with decreasing number of deposition cycles. The lower the amount of Pt, the larger was the red shift of the CO resonance. The films with few deposition cycles have, as mentioned before, more step sites, which bind CO stronger and cause a red shift in the resonance. In addition, the rough films do not allow adsorption of CO in a well ordered structure. This causes the CO coverage to be lower than for the smoother films also contributing to the red shift.

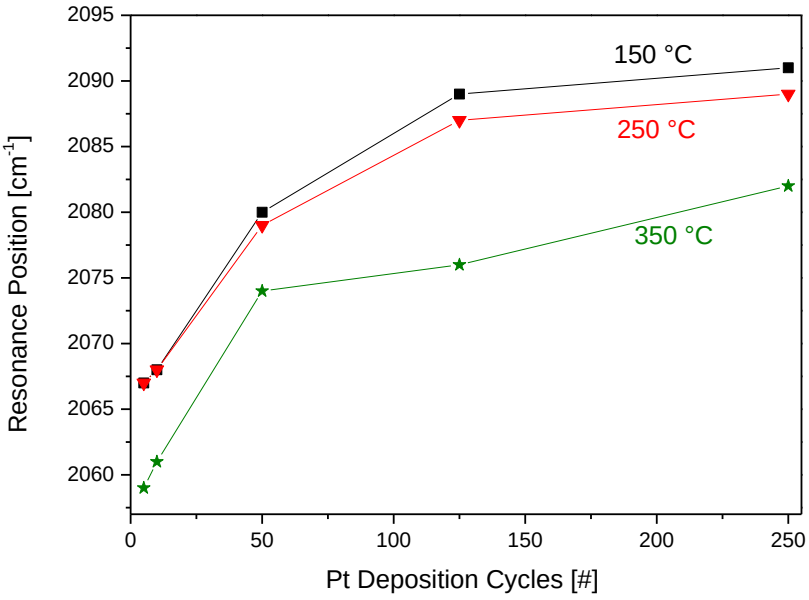

Figure 6.7: Positions of on-top CO resonances during reaction (10 mbar CO, 20 mbar O_2) for Pt films with different numbers of ALD deposition cycles. For all samples values at temperatures 150 (black), 250 (red) and 350 °C (green) are shown.

Figure 6.7 also shows that for samples with more deposition cycles the difference in peak position is smaller. Obviously, at some point the smoothness of the surface cannot be increased further by continuing deposition of Pt and the peak position stabilizes

around 2092 cm^{-1} at 150 °C. Another important finding concerns the red shift with increasing temperature. For the smoother films each temperature step causes a red shift to the resonance position due to thermal desorption of CO. In comparison, the first step shown from 150 to 250 °C does not induce any change in the resonance position of the 5 and 10 cycle samples and only a minor shift for the 50 cycle film. These results support our previous assumption that CO is adsorbed stronger on the thinner films. It is therefore more difficult to remove CO from the surface. The CO poisoning persists to higher temperatures on these rougher films and "delays" the reaction to higher temperatures.

While the trend between different numbers of deposition cycles and catalytic activity is quite clear for the SFG measurements, it is still contrary to several reports of nanoparticles being more active than bulk crystals or continuous films. To support our findings and ensure that neither our laser technique nor our chamber was responsible for the unexpected results, we decided to use a second well-established operando method.

6.2 Operando NAP-XPS Spectroscopy

The operando XPS measurements were performed at the synchrotron facility MAX IV in Lund, Sweden. The experiments were conducted on the very recently opened HIPPIE beamline, which features a UHV chamber that included a smaller chamber for operando experiments. The catalytic reactions in this setup were performed in flow mode, as the differential pumping is incompatible with a batch reactor. The gas composition throughout the reaction was again monitored by a mass spectrometer. Due to experimental limitations the maximum pressure reachable during the NAP-XPS measurements was 3 mbar (i.e. one magnitude below pressures used in SFG). Still, we used the same 1:2 ratio for CO and O_2 as in SFG.

First, spectra of the catalyst elements, Pt 4f and Zr 3d, are discussed, as XPS allows direct investigation of surface composition changes. It has been reported several times that oxidation of surface Pt may occur during reaction [97, 98]. Figure 6.8 shows the Pt 4f peaks for the 250 cycle ALD sample (top) and for the 50 cycle ALD sample (bottom) for different temperatures. The peaks are fitted with asymmetric line shapes, due to their metallic nature. In addition, some constraints can be applied to the fits as the area of 4f 5/2 is 75 % of the 4f 7/2 peak and the distance between the peaks is fixed (spin orbit splitting, 3.3 eV). It is then apparent from the fit that the peak position was the same for both samples and for all reaction temperatures: 71.0 eV for the Pt 4f 7/2. There were no

visible shoulders emerging throughout the reaction measurements. The design of the beam line did not allow the use of photon energies lower than 670 eV; this is by far higher than the binding energy of 71-75 eV and the resulting core level photoelectrons therefore have relatively high kinetic energies. For the resulting kinetic energy of 598 eV of the photoelectrons the inelastic mean free path is roughly 1.2 nm. Assuming the maximum probing depth as the depth where 95% of all photoelectrons are inelastically scattered, it can be calculated as 35 Å. Thus, the measurements are not very surface sensitive but a potential surface oxidation should still be visible as a small shoulder (but was absent).

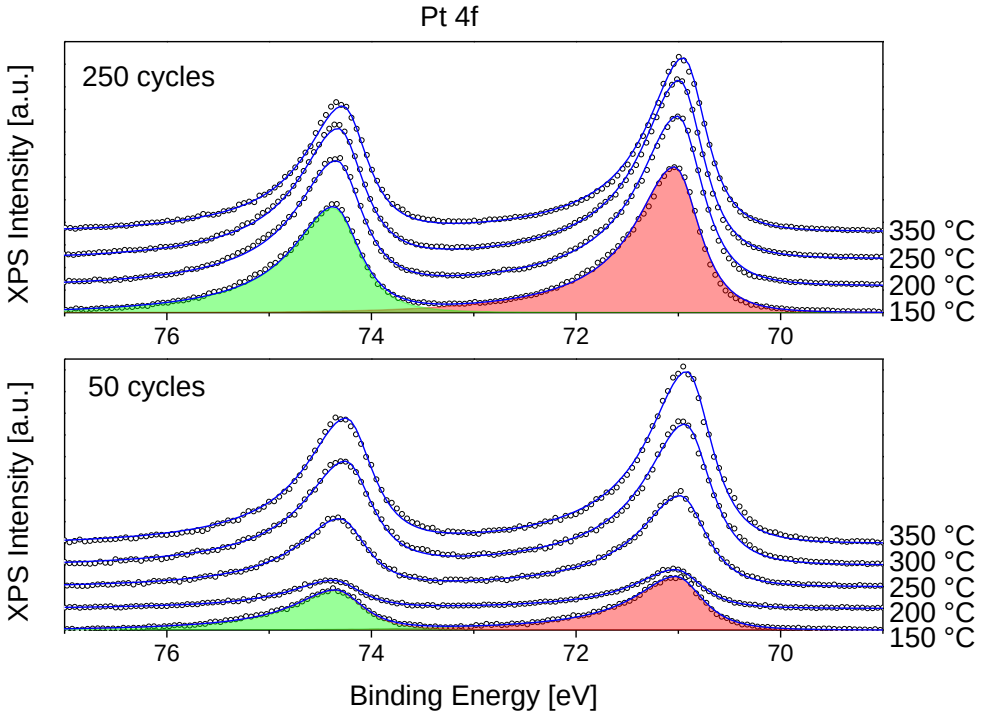

Figure 6.8: Pt 4f XPS spectra of the 250 and 50 cycle film at different increasing CO oxidation temperatures (1 mbar CO and 2 mbar O_2).

The only significant change at different temperatures was the change in intensity for the 50 cycle film. For lower temperatures, especially 200 °C the intensity of the Pt peaks was very low compared to higher temperature spectra. As the amount of Pt on the sample did not change the measurements imply that the Pt signal was somehow obscured (by something covering the surface), an effect that disappeared at higher temperatures.

Figure 6.9 shows the corresponding Zr 3d peaks for the same measurement at temperatures 150, 250 and 350 °C. The position of zirconia peaks at 150 °C was 182.7 eV for 3d 5/2 for the 250 cycle peak and 182.4 eV for the 50 cycle film. The small shift is due to the influence of the different amounts of Pt on the zirconia. At 350 °C a peak shift by

0.3 eV to lower binding energies could be observed for both samples. This is most likely due to the start of oxidation. The different surface coverage changes the surface work function and oxygen from the zirconia (at the metal oxide interface) is consumed by the reaction, lowering the oxidation state of the surrounding zirconium atoms. In addition, as seen for the Pt, the peak intensities for the 50 cycle film increased with higher temperature. This was again a sign of a species covering the surface, which was removed upon temperature increase. The zirconium peaks at higher temperatures were also much larger for the 50 cycle film than for the 250 cycle film as there is less Pt obscuring the signals. As stated before, the zirconia peaks should not be visible for a pristine 250 cycle film, but the measured sample was slightly altered by previous sputter pretreatment.

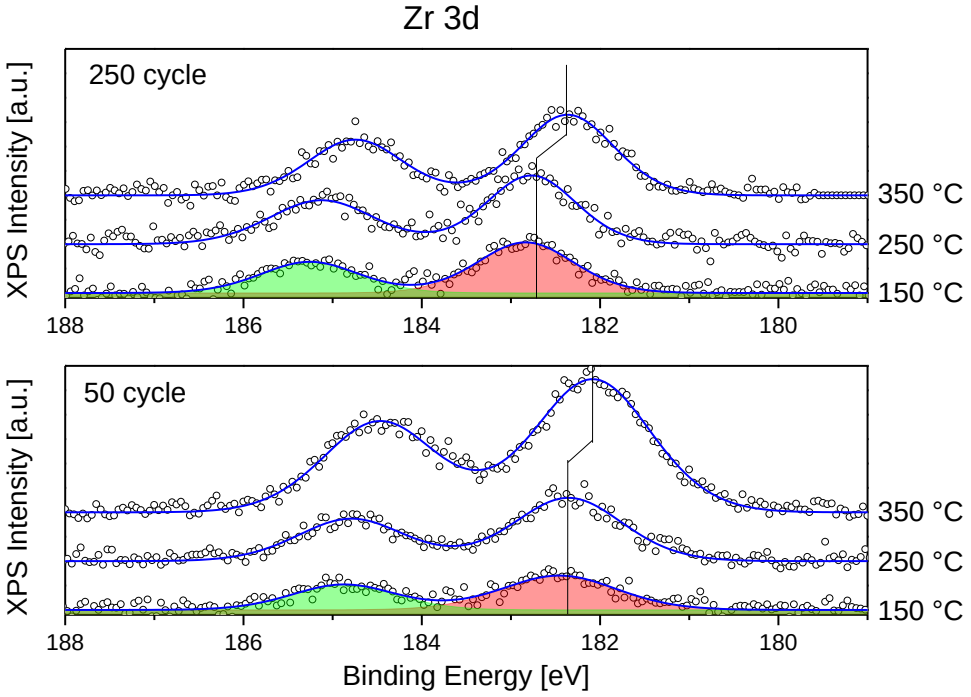

Figure 6.9: Zr 3d XPS spectra of the 250 and 50 cycle Pt film at different temperatures in oxidation mixture of 1mbar CO and 2mbar O_2.

The next step was to investigate the C1s signals of possible surface adsorbates. To ensure that all observed carbon species were due to the reaction environment and not due to adventitious carbon on the surface, the samples had first been cleaned. They were heated in oxygen and simultaneously checked by XPS measurements to guarantee that no carbon was initially present. A comparison of C 1s spectra of the clean surfaces to those during reaction is shown in Figure 6.10 for the 250 and 50 cycle ALD Pt samples.

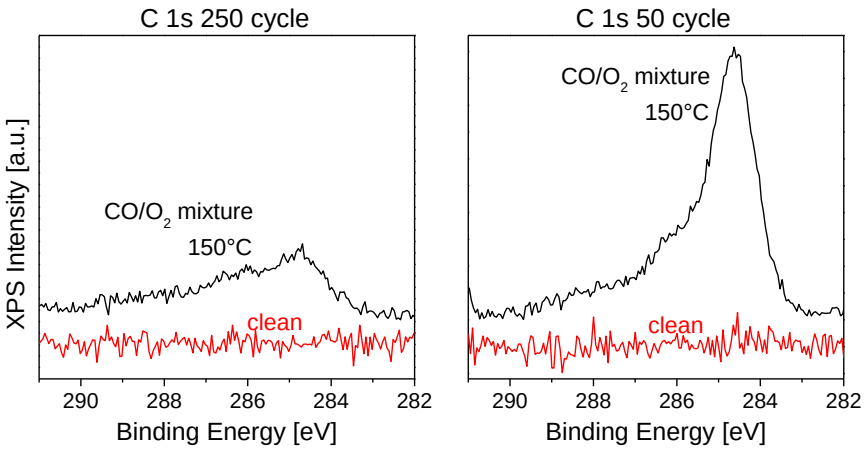

Figure 6.10: C 1s spectra of clean surface versus surface in reaction mixture (1 mbar CO, 2 mbar O_2).

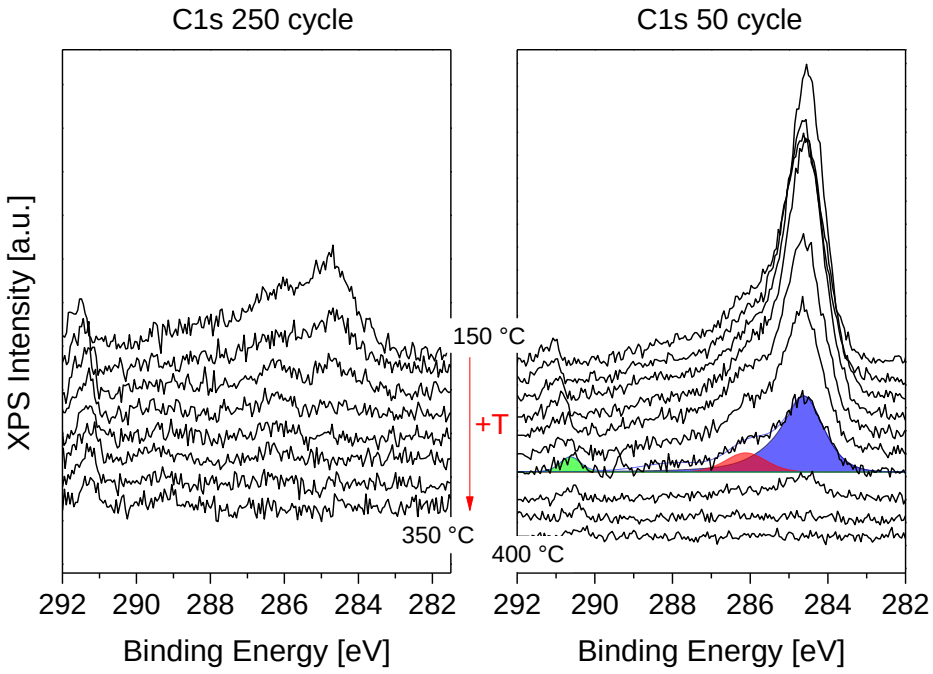

Figure 6.11: Temperature dependent C1s NAP XPS spectra of 250 and 50 cycle Pt model catalysts in CO oxidation environment. The gas pressure was 1 mbar CO and 2 mbar O_2 and temperatures are ramped from 150 °C in 25 °C steps up until no carbon features can be observed anymore.

In Figure 6.11 C1s spectra are displayed for increasing reaction temperatures for the 250 and 50 cycle film (from 150 °C in 25 °C steps up to 350 °C and 400 °C, respectively). At high binding energies a narrow peak was observed, which can be assigned to gas phase CO. With increasing temperature this gas phase peak lost intensity due to the reaction. For even higher concentrations of CO_2 a new gas phase peak would appear for CO_2. At lower binding energies a broad feature consisting of several peaks could be observed,

which corresponded to different carbon compounds on the surface. It was clearly visible that all of them disappeared from the surface at higher reaction temperatures.

A detailed plot of the different C 1s surface features can be found in Figure 6.12. The peak at lowest binding energy of 284.4 eV (blue) is due to graphitic carbon [90], which most likely originates from CO dissociation at steps. The peak at 286.4 eV (red) arises from molecular CO adsorbed on the surface [91, 92]. The small feature at 288.2 eV (orange) is broad and possibly containing several sub features that cannot be fitted separately with reliable accuracy. The position suggests carbon from higher oxidized compounds [97]. These may be found at the interface to the zirconia support, where more oxygen is available. The last feature around 291 eV (green) corresponds to gas phase CO.

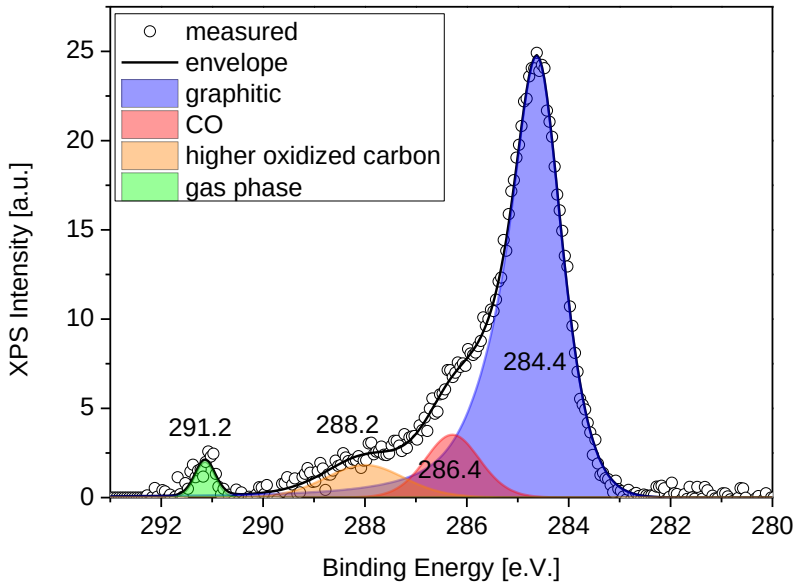

Figure 6.12: Example of a fitted C 1s NAP-XPS spectrum in CO oxidation environment. At lower binding energies several surface features can be found, while at higher binding energies a CO gas phase is visible.

It was explained before that the catalyst surface is CO poisoned as long as CO was blocking the adsorption sites for O_2. Therefore, the gas phase peak should be stable in intensity until the reaction starts/ignites. It was therefore reasonable to compare the peak intensities of adsorbed and gas phase CO. The results are shown in Figure 6.13. On the 250 cycle Pt film a slow decrease of both peak areas was observed over a larger temperature interval. The gradual change over a large temperature regime was, as discussed previously, due to the different surface terminations of different Pt crystal grains. On the 50 cycle Pt film the decrease in peak intensity of adsorbed CO from roughly 275 °C to 350 °C matched the strong decrease in gas phase CO from 300 °C to

350 °C upon reaction onset. Both samples match our expectations, still, the spectra of adsorbed CO and gas phase CO could not explain the higher reaction onset temperature for the more particle-like film.

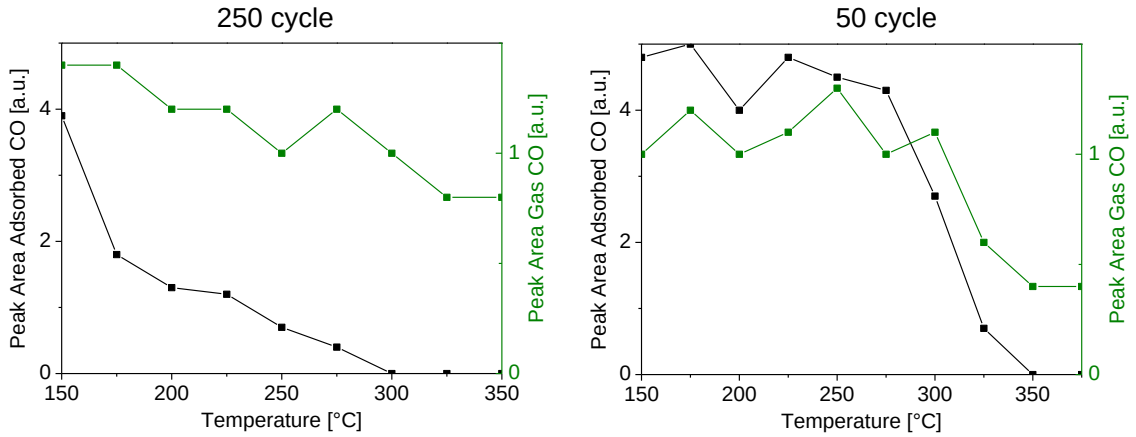

Figure 6.13: Comparison of adsorbed (black) and gas phase (green) CO peak areas. Especially for the 50 cycle ALD Pt film the temperature for the decrease in intensity of both peaks matches very well.

A possible explanation for the temperature difference in the onset of CO oxidation can nevertheless be found in the C1s spectra. The carbon signal intensity of the 50 cycle film is much larger than for the 250 cycle film. This is due to the large amount of graphitic carbon on the surface.

Figure *6.14* shows a comparison of both surface CO and graphitic carbon peak areas for the temperature dependent C1s spectra. It is obvious that the graphitic carbon peak area is not only larger for the 50 cycle film than for the 250 cycle film, it also increases for the first few temperature steps. This explains the diminished intensities of the Pt and Zr signals in Figure 6.8 and Figure 6.9 at 200 °C.

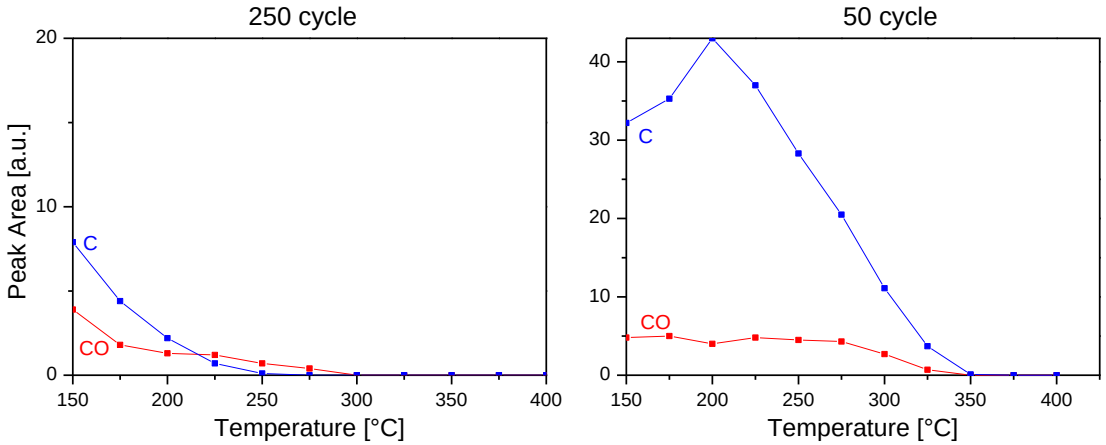

Figure 6.14: Comparison of peak areas of adsorbed CO (red) and graphitic carbon (blue) for 250 and 50 cycle ALD Pt model catalyst.

The increased amount of carbon was most likely due to higher CO dissociation probability on the rougher 50 cycle film. We have seen this already before in the SFG studies on CO adsorption; there the dissociation was dependent on surface roughness. The large amount of carbon on the surface also hinders the early switching from the CO poisoned surface to the oxygen covered reactive surface, as first the carbon has to be removed to free active sites. For the 250 cycle film the graphitic carbon was gone at 275 °C, before all CO was desorbed from the surface while for the 50 cycle film the graphitic carbon peak was still larger than the adsorbed CO peak even at 325 °C. This finding is in accordance with the trend that rougher surfaces have higher reaction onset temperatures. As CO dissociation increases with higher surface roughness this causes even more carbon contamination of rougher (thinner) films, which must be removed.

As mentioned before, the gas atmosphere was monitored simultaneously to the XPS spectra. The resulting data for the 50 cycle ALD Pt films is plotted in Figure 6.15. The different temperature steps are denoted at the visible steps of CO_2 increase in the graph. The first visible step in CO_2 could be seen at 250 °C after the amount of graphitic carbon started to decline in the XPS spectra. With higher reaction temperatures the amount of produced CO_2 increased even more at each temperature step. This is due to faster reaction kinetics at higher temperature in general, but also due to the additional switching of facets with different surface terminations and the removal of graphitic carbon.

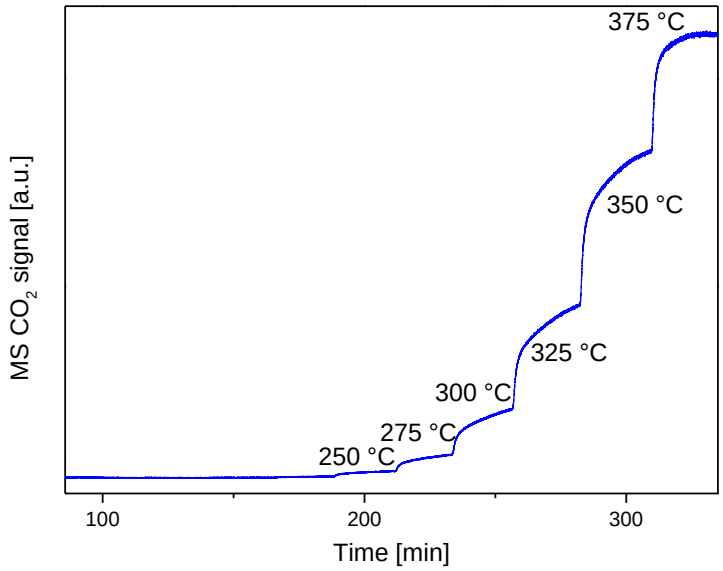

Figure 6.15: MS data for the reaction measurements on the 50 cycle sample. Temperature steps are denoted, stepwise increasing CO_2.

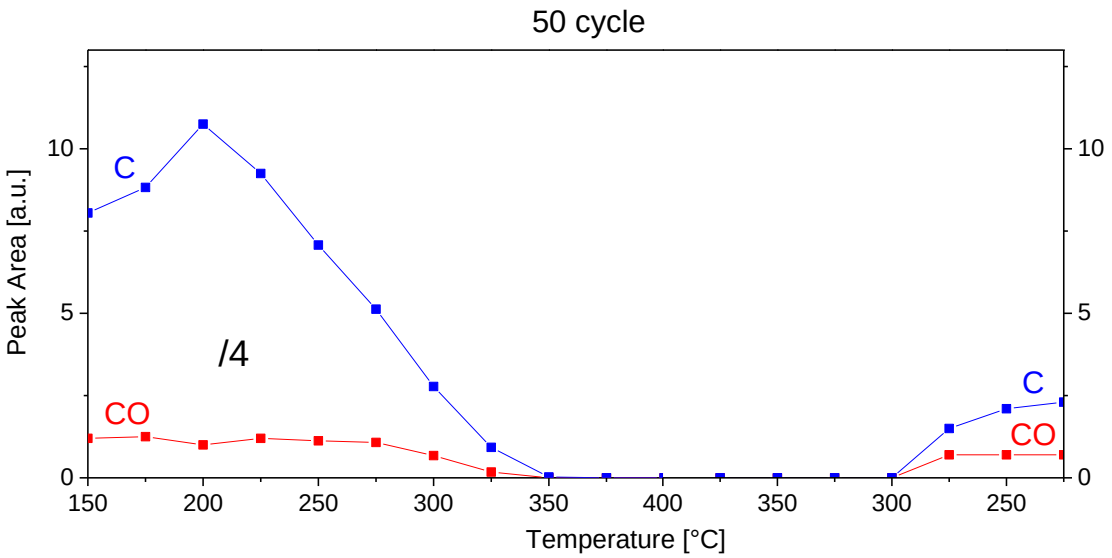

Figure 6.16: CO and graphitic C peak areas from fitted C 1s spectra at different temperatures in reaction gas mixture. The spectra were first taken while heating the sample to 400 °C, then while cooling back to 225 °C.

An additional way to show that the significant carbon contamination was responsible for the "delayed" CO oxidation onset (to higher temperatures) is to compare with spectra taken while cooling down in reaction environment. Figure 6.16 shows the peak area of surface CO and graphitic carbon for increasing and decreasing temperature on the 50 cycle ALD Pt film. The values of peak areas while heating up were divided by 4 for a better presentation. The results showed that there was a hysteresis between heating and cooling. The CO peak persisted to 325 °C while heating up but only reappeared 275 °C upon cooldown. In addition, the peak areas for both CO and graphitic carbon on the surface were much lower upon cooldown to 225 °C. Apparently, the reaction environment helped in keeping the surface clean and oxygen covered, when cooling down, until the CO adsorption and dissociation started and blocked sites again. The hysteresis as well as the stronger increase of the graphitic carbon peak even after cooldown supported the suggestion that the activity of the rough model catalyst was limited by the carbon contamination from CO dissociation.

To complete the NAP-XPS measurements, Figure 6.17 shows the C 1s spectra of the 10 cycle ALD Pt film during CO oxidation reaction (left panel) and the respective peak areas for surface CO and graphitic carbon (right panel). For this sample, the peak area of graphitic carbon was roughly twice the area of adsorbed CO at 150 °C. While this ratio is comparable to the 250 cycle ALD Pt film, the overall amount of carbon and CO on the surface was much higher. The surface poisoning persisted to an even higher temperature (375 °C). In addition, graphitic carbon stayed on the surface until the full

switch of coverage to oxygen occurred (i.e. start of the reaction on all surface terminations), as seen for the 50 cycle ALD Pt film. These results show that the carbon contamination through dissociation was again impairing the reactivity of the catalyst.

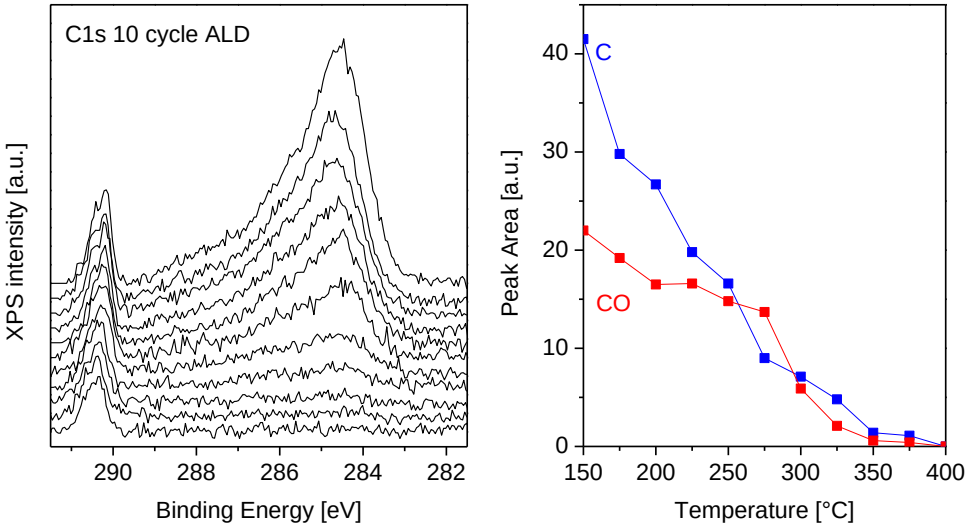

Figure 6.17: Left: C 1s NAP-XPS spectra for 10 cycle ALD Pt in reaction environment (1 mbar CO, 2 mbar O_2). Temperature was increased in 25 °C steps from 150 to 400°C. Right: peak area of adsorbed CO and graphitic carbon from fits of the temperature dependent spectra.

Compared to the SFG measurements, all desorption temperatures were lower in the NAP-XPS measurements. This was expected due to the lower total pressure of 3 mbar (compared to 30 mbar in SFG). Nevertheless, the same trends were observed. A comparison of the temperatures at which CO was no longer visible in the SFG and NAP-XPS measurements is shown in Table 6.4. For the three measured model catalysts, CO persisted to higher temperatures on samples with fewer deposition cycles. While the absolute temperatures were different (this is partly due to the different pressures but also due to different detection limits), the relative temperatures between the different samples were similar. From the 250 cycle ALD Pt island sample to the 50 cycle Pt particle sample a difference of 50 °C in the removal of CO was observed and an additional 25 to 50 °C was needed to remove CO from the 10 cycle ALD Pt sample.

Table 6.4: Temperatures of SFG and XPS spectra, for which CO first disappeared upon heating the samples.

ALD Pt cycles	No CO in SFG	No CO in NAP-XPS
250	400 °C	300 °C
50	450 °C	350 °C
10	475 °C	375-400 °C

To sum up, the trend in reaction temperature for the model catalysts was the same in SFG and NAP-XPS spectra. While SFG spectra did not yield a full explanation of the results, the measurements could easily be performed with our laboratory setup. The addition of the synchrotron based NAP-XPS measurements yielded further insight to the shift of the reaction onset to higher temperatures for rough films by highlighting that CO dissociation was also present in oxidation conditions.

7 Summary

Model catalysts: Over the course of this thesis different ALD and SD Pt/ZrO_2 model catalysts have been structurally characterized and used for CO adsorption and oxidation measurements. The samples were prepared by depositing a 40 nm ALD zirconia film as a catalyst support on a Si wafer substrate. The active metal was Pt, which was deposited on top of the zirconia by either ALD or SD with differing amounts of Pt (5, 10, 50, 125, 250 and 750 deposition cycles for ALD and 2, 5, 10 and 30 nm nominal thickness for SD). TEM and XRD measurements showed that ALD samples with more deposited Pt had an island structure, while the thinner ALD samples had a particle structure, with smaller crystal grain sizes. In all cases the zirconia was homogeneous with large crystal grains and the Pt was poly crystalline. The SD samples were not fully characterized as they showed severe surface instabilities during CO adsorption measurements. The Pt on the SD samples did not stick well to the supporting oxide. With the heat of laser radiation it partly detached from the surface in ribbons, forming large three dimensional Pt structures. Thus, SD samples were unsuitable as model catalysts and not investigated in more detail. In depth measurements solely focused on the ALD prepared samples, especially on the 250 cycle Pt film as bulk-like model and on the 50 cycle Pt film as particle-like model.

Characterization of the SFG System: The optical parameters of the SFG system in our laboratory were thoroughly characterized for the first time. Reference spectra were collected for the intensity of the IR beam over the whole measurement range and for the stability of the beam intensities over time. Spectra of GaAs and ZnSe were acquired for signal comparison after adjustment of the beam paths and the influence of gas phase absorption on the SFG signals was studied to be able to interpret SFG data correctly.

CO Adsorption: We used SFG measurements of CO adsorption for additional sample characterization and as basic reference data for the reaction studies. We only investigated the on-top resonances of CO on Pt, as signal contributions of other resonances (bridge and hollow) were too weak in SFG. For the different film structures we saw shifts in the resonance position, intensity and peak shape. The shifts were mainly due to two reasons: different binding strength (e.g. steps vs terraces) and different coverage. For the various films the peak positions depended strongly on structural differences. More particulate structure had lower amounts of terrace and higher amounts of step sites; therefore a redshift was present due to different binding strengths. For increasing temperatures the surface structure might change, but observed resonance shifts were more likely due to CO desorption. The facets of a polycrystalline

surface have different desorption properties, so desorption from one kind of surface termination causes an overall intensity change and peak shift in the SFG spectra. The difference in surface structure was also investigated using polarization dependent SFG measurements, which can distinguish between molecular bonds parallel to and tilted from the surface normal. Films with fewer deposition cycles had more adsorbates tilted to the macroscopic surface normal, implying that there were more tilted crystal facets. This was in accordance with the TEM images from sample characterization. SFG spectra of adsorbed CO can thus also be used to highlight the roughness increase for samples with less deposition cycles (more particle-like structure).

CO dissociation: An unexpected finding in the adsorption studies was a sudden peak change on rough surfaces with increasing temperature. The intensity strongly decreased and the resonance position was red shifted for temperatures above 225 °C. These changes were similar to the changes induced by desorption (red shift, intensity loss), yet desorption at this temperature should also have been observed on all samples. It was therefore assumed that CO dissociated on the steps and kinks of rough surfaces, spreading over the terraces to cause this signal change. This hypothesis was supported by measuring cool down spectra that showed that the initial CO peak was not recovered at room temperature, i.e. the change was not reversible. Furthermore, spectra in CO/O_2 mixture showed that the addition of oxygen allowed recovery of a normal CO on-top peak upon heating. Starting at 175 °C, the oxygen cleaned up adsorption sites for CO, which was still dominant in adsorption, so the surface was CO covered. Most importantly, the dissociation related measurements suggested that rougher surfaces were more prone to causing CO dissociation than smoother surfaces.

CO oxidation monitored by SFG: The central point of the model catalyst investigations were reaction studies. For the CO oxidation measurements we compared mass spectrometer data and SFG spectra for increasing reaction temperatures on the 50 and 250 cycle film. Again, the SFG spectra showed a roughness induced redshift from island to particle film, in addition to the temperature induced redshift through CO desorption. An interesting result was that CO_2 started to increase in the gas phase (i.e. start of oxidation), while the CO signal was still present. Only by increasing the temperature by another 100 °C above the reaction on-set temperature, the CO signal fully disappeared from the SFG spectra. CO on the surface "poisons" the catalyst and blocks CO oxidation so catalytic activity should only start after the CO is removed. This duality of adsorbed CO and CO_2 production at the same time was due to the polycrystallinity of the sample surface. Some crystal terminations allowed switching of surface coverage to oxygen,

starting the CO_2 production, while other facets were still CO poisoned and contributed to the SFG spectra. Furthermore, the reaction on-set temperature and the temperature at which CO was removed from the surface were higher for the Pt particle film than for the island/bulk film. While this was partly due to stronger bonding of CO to steps than terraces (i.e. harder to remove from steps), the stronger bonding of oxygen to rough surfaces and the additional oxygen provided by the zirconia support should counteract the increase in temperature. Thus, additional NAP-XPS measurements were performed to uncover the reason for the decreased activity of particle model catalysts.

CO oxidation monitored by NAP-XPS: The NAP-XPS measurements showed the same trend as the SFG measurements, to be specific, they showed that CO oxidation reaction was offset to higher temperatures for the particle like film compared to the smoother continuous film. These measurements also provided an explanation for the increased reaction temperature. On the 50 cycle film a significant amount of graphitic carbon was found blocking the active surface. For the 250 cycle film, the much lower amount of graphitic carbon was removed from the surface before complete CO desorption. The carbon contamination on the particle film persisted until the surface switched to oxygen coverage. The carbon inhibited early coverage switching, "delaying" the reaction on set to higher temperatures. It appeared to be the main limitation for CO oxidation on the 50 cycle particle film. NAP-XPS spectra on a 10 cycle ALD Pt film could show that this was a trend for samples with fewer deposition cycles, as the same carbon contamination caused the reaction on-set temperature to be even higher. In conclusion the SFG and NAP-XPS measurements correlated well and we could show that the CO dissociation observed in CO adsorption measurements also played a vital role in CO oxidation for rough model catalysts.

8 Conclusion and Outlook

The motivation for the current experiments was the design and investigation of model catalysts, to get a better grasp on surface interactions and, at the same time, to bridge the materials and pressure gaps. Overall we were successful in our design of model catalysts. While sputter deposition of Pt did not yield reliable samples, ALD proved to be a great technique for manufacturing samples with different surface structures. ALD Pt can also be deposited for industrial catalysts similarly to our models by just using a different support material, which supports the relevance of our model. The ALD models were also well suited for SFG and NAP-XPS measurements with their macroscopically smooth surfaces allowing measurements at higher pressures, i.e. bridging the pressure gap. Simultaneously, they still featured different microscopic roughness, closing the materials gap.

By comparing catalysts throughout the "bulk-to-particle" transition, we found a strong discrepancy between annealed single crystals, which were often used as catalyst models, and complex and more "disordered" model catalysts. In adsorption measurements CO dissociation was not observed on the smooth single crystal using SFG, while it was very prominent on all samples with rougher surfaces. Furthermore, CO dissociation had a lasting effect on the CO oxidation reaction on our model catalysts, affecting surfaces differently depending on microscopic surface structuring. These measurements prove that studies on too simple catalyst models may not explain phenomena seen on industrially relevant catalysts. They show that it is crucial to choose suitable models and to compare the different findings to understand what is happening at a surface during reaction and to finally implement the research in catalyst development.

With the ALD prepared Pt catalysts we found an unforeseen effect, with Pt particles requiring higher temperatures for CO oxidation than smooth bulk-like material. By combining SFG measurements on CO adsorption and oxidation with NAP-XPS measurements on CO oxidation we were able to explain the temperature difference. Smoother surfaces were CO covered and different facets switched easily to oxygen coverage at higher temperatures. Rough surfaces (comprised of particles) had high amounts of carbon contamination due to CO dissociation at steps and edges. On these particles higher temperatures are required to allow the coverage switch from CO to oxygen, therefore the reaction is "delayed". This is schematically shown in Figure 8.1.

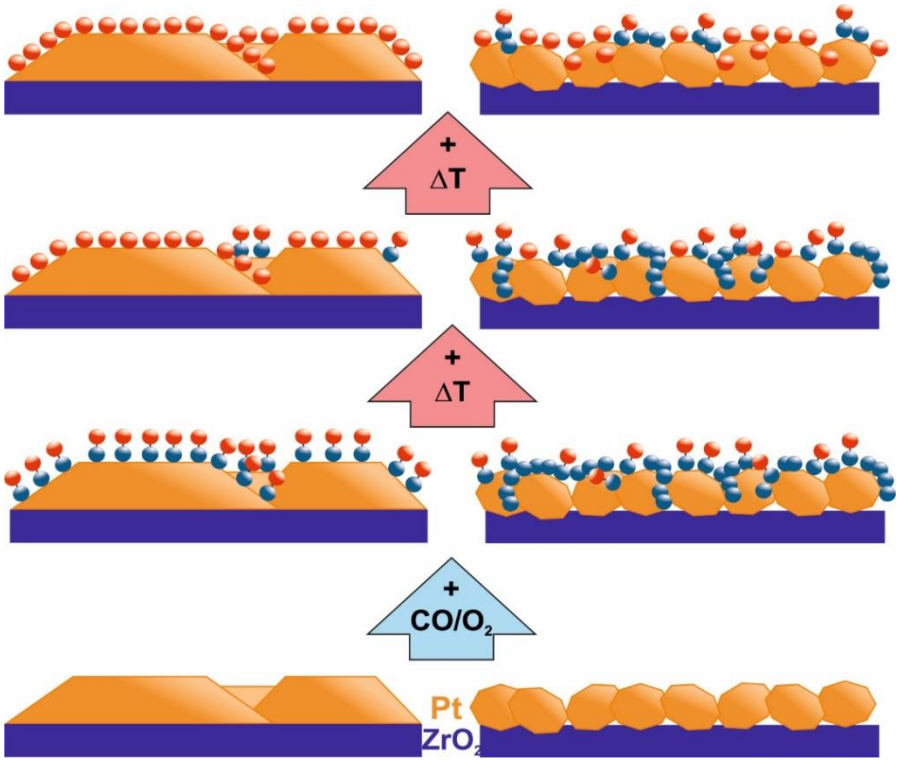

Figure 8.1: Schematic evolution of surface coverage of the model catalysts. Starting from the clean surface the addition of reaction atmosphere CO/O_2 causes surface coverage with CO on the terraces and carbon contamination from CO dissociation on the steps. Heating the sample in the CO/O_2 gas mixture causes the terraces to switch from CO to oxygen coverage but the high amount of carbon on the rough particles inhibits this switch and CO poisoning persists to higher temperatures.

For application of these results to advancements in real catalysis it is of course important to further study this trend. The measurements on a Pt film with less deposition cycles but differently shaped Pt particles showed less CO dissociation overall, but high amounts of carbon contamination still persisted to very high temperatures. Using other amounts of Pt (by either changing the number of ALD cycles or the deposition temperature) it may be possible to change the geometry of the Pt particles to a more favorable smooth geometry. It should also be investigated whether higher ratios of oxygen in the reaction mixture can circumvent the contamination from dissociation. High partial pressures of O_2 compared to CO might inhibit CO dissociation at steps even for the rough particles, facilitating the switch in coverage. For further steps it would therefore be reasonable to study the impact of different gas ratios and to adjust the model catalysts by modifying the catalyst preparation. Apart from changing parameters of the ALD process (depositing different amounts of Pt, obtaining different particle geometries), the influence of different support materials should also be tested.

Another interesting issue is polarization dependent SFG investigations of the CO oxidation reaction. They may yield a better understanding of coverage on different facets. This would be especially interesting if a preferential growth direction of the Pt particles could be achieved by a modified ALD particle preparation. The polarization measurements on CO adsorption already proved it an interesting tool to compare surface structures in gas atmosphere and would surely provide interesting results during oxidation measurements. In addition, the SFG experiments could also be extended by time-dependent pump-probe measurements. While this setup requires additional experimental adjustment, it may allow the direct study of increased temperature on the stability of carbon contamination (observed on particles) and how fast it spreads at different sample temperatures.

As a last point it would of course be interesting to use ALD prepared model catalysts for investigations of other reactions. Zirconia as a support material is for example found in various reforming catalysts (mostly in combination with Ni nano particles). Our studies using Pt model catalysts were very rewarding and the application of ALD model catalysts worked very well. So it may be straight forward to prepare different material combinations for ALD model catalysts in the future.

9 Acknowledgements

Research and writing required for a thesis take up lots of time and effort. It is therefore only possible with a solid social and work infrastructure. I want to thank all the people who contributed directly or indirectly to make this work possible for me, especially:

My supervisor Prof. Günther Rupprechter for providing the great work environment. My time as a PhD student was much fun with the possibility to join several international conferences and travels to research facilities abroad.

My co-supervisor Christoph Rameshan, who told a friend of mine about "this great PhD position with spectroscopy and lasers and stuff, where we investigate catalysts". Without him I would not have come to Vienna. And I would not have nagged him all the time with questions, while he was trying to concentrate on his work.

My colleagues at the institute and in the DK Solids4Fun as they were always ready to give advice if they could help with a problem and to chit-chat when I wanted to procrastinate. It also helped a lot to hear them complaining about their work, as it made my progress feel better. I am very happy that some of these colleagues became good friends: Thank you Laura, Clara, Philipp, Magdalena, Astrid and Thomas!

My fiancé Stefan for his love and care. Especially on days when I came home exhausted, he cooked supper and bought chocolate <3.

My family, as they always supported me in my decision to study physics and to follow up my master with a PhD. My parents helped me find a flat and move all my things when I came to Vienna.

The student in "Rechenübung PC2", who told me I would be a cool professor.

My physics teacher Georg Jud in the "Oberstufe", who showed me that physics was an exciting subject, after I hated it from the "Unterstufe". (The only thing I can remember of "Unterstufen"-physics is that we learned 5 different forms of water turbines.)

And of course the Austrian Science Fund FWF through the projects SFB FOXSI (F4502-N16) and DK Solids4Fun (W1243) and the TU Wien for the immense financial support.

10 Literature

[1] N.S. Lewis, D.G. Nocera, Powering the planet: Chemical challenges in solar energy utilization, Proceedings of the National Academy of Sciences, 103 (2006) 15729.
[2] R. Schlögl, Sustainable Energy Systems: The Strategic Role of Chemical Energy Conversion, Topics in Catalysis, 59 (2016) 772-786.
[3] L.M. Gandia, G. Arzamedi, P.M. Dieguez, Renewable Hydrogen Technologies: Production, Purification, Storage, Applications and Safety, Elsevier Science2013.
[4] D.P. Woodruff, Modern Techniques of Surface Science, Cambridge University Press2016.
[5] H.-J. Freund, H. Kuhlenbeck, J. Libuda, G. Rupprechter, M. Bäumer, H. Hamann, Bridging the pressure and materials gaps between catalysis and surface science: clean and modified oxide surfaces, Topics in Catalysis, 15 (2001) 201-209.
[6] M. Saurat, S. Bringezu, Platinum Group Metal Flows of Europe, Part 1, Journal of Industrial Ecology, 12 (2008) 754-767.
[7] C.-J. Yang, An impending platinum crisis and its implications for the future of the automobile, Energy Policy, 37 (2009) 1805-1808.
[8] Y. Sun, M. Delucchi, J. Ogden, The impact of widespread deployment of fuel cell vehicles on platinum demand and price, International Journal of Hydrogen Energy, 36 (2011) 11116-11127.
[9] C. Sealy, The problem with platinum, Materials Today, 11 (2008) 65-68.
[10] B. Qiao, A. Wang, X. Yang, L.F. Allard, Z. Jiang, Y. Cui, J. Liu, J. Li, T. Zhang, Single-atom catalysis of CO oxidation using Pt1/FeOx, Nat Chem, 3 (2011) 634-641.
[11] S. Alayoglu, A.U. Nilekar, M. Mavrikakis, B. Eichhorn, Ru-Pt core-shell nanoparticles for preferential oxidation of carbon monoxide in hydrogen, Nat Mater, 7 (2008) 333-338.
[12] G.N. Vayssilov, Y. Lykhach, A. Migani, T. Staudt, G.P. Petrova, N. Tsud, T. Skála, A. Bruix, F. Illas, K.C. Prince, V.r. Matolı´n, K.M. Neyman, J. Libuda, Support nanostructure boosts oxygen transfer to catalytically active platinum nanoparticles, Nat Mater, 10 (2011) 310-315.
[13] F. Tao, M. Salmeron, In Situ Studies of Chemistry and Structure of Materials in Reactive Environments, Science, 331 (2011) 171-174.
[14] B.E. Hayden, A.M. Bradshaw, The adsorption of CO on Pt(111) studied by infrared reflection—Absortion spectroscopy, Surface Science, 125 (1983) 787-802.
[15] F.J.C.M. Toolenaar, F. Stoop, V. Ponec, On electronic and geometric effects of alloying: An infrared spectroscopic investigation of the adsorption of carbon monoxide on platinum-copper alloys, Journal of Catalysis, 82 (1983) 1-12.
[16] M.J. Lundwall, S.M. McClure, D.W. Goodman, Probing Terrace and Step Sites on Pt Nanoparticles Using CO and Ethylene, The Journal of Physical Chemistry C, 114 (2010) 7904-7912.
[17] A. Crossley, D.A. King, Infrared spectra for co isotopes chemisorbed on Pt “111”: Evidence for strong absorbate coupling interactions, Surface Science, 68 (1977) 528-538.
[18] G. Rupprechter, Sum Frequency Generation and Polarization–Modulation Infrared Reflection Absorption Spectroscopy of Functioning Model Catalysts from Ultrahigh Vacuum to Ambient Pressure, in: B.C. Gates, H. Knözinger (Eds.) Advances in Catalysis, Academic Press 2007, pp. 133-263.
[19] R.W. Boyd, D. Prato, Nonlinear Optics, Elsevier Science 2008.
[20] Y.R. Shen, The Principles of Nonlinear Optics, Wiley 1984.

[21] C. Hirose, N. Akamatsu, K. Domen, Formulas for the analysis of surface sum-frequency generation spectrum by CH stretching modes of methyl and methylene groups, The Journal of Chemical Physics, 96 (1992) 997-1004.
[22] A.J. Moad, G.J. Simpson, A Unified Treatment of Selection Rules and Symmetry Relations for Sum-Frequency and Second Harmonic Spectroscopies, The Journal of Physical Chemistry B, 108 (2004) 3548-3562.
[23] X. Chen, M.L. Clarke, J.I.E. Wang, Z. Chen, Sum Frequency Generation Vibrational Spectroscopy Studies on Molecular Conformation and Orientation of Biological Molecules at Interfaces, International Journal of Modern Physics B, 19 (2005) 691-713.
[24] J.P. Kraack, P. Hamm, Surface-Sensitive and Surface-Specific Ultrafast Two-Dimensional Vibrational Spectroscopy, Chemical Reviews, 117 (2017) 10623-10664.
[25] P.B. Miranda, Y.R. Shen, Liquid Interfaces: A Study by Sum-Frequency Vibrational Spectroscopy, The Journal of Physical Chemistry B, 103 (1999) 3292-3307.
[26] K.B. Eisenthal, Liquid Interfaces Probed by Second-Harmonic and Sum-Frequency Spectroscopy, Chemical Reviews, 96 (1996) 1343-1360.
[27] F. Vidal, A. Tadjeddine, Sum-frequency generation spectroscopy of interfaces, Reports on Progress in Physics, 68 (2005) 1095.
[28] Z. Chen, Investigating buried polymer interfaces using sum frequency generation vibrational spectroscopy, Progress in Polymer Science, 35 (2010) 1376-1402.
[29] R.J.D. Tilley, Crystals and Crystal Structures, John Wiley & Sons Ltd. 2006.
[30] A.G. Lambert, P.B. Davies, D.J. Neivandt, Implementing the Theory of Sum Frequency Generation Vibrational Spectroscopy: A Tutorial Review, Applied Spectroscopy Reviews, 40 (2005) 103-145.
[31] X. Zhuang, P.B. Miranda, D. Kim, Y.R. Shen, Mapping molecular orientation and conformation at interfaces by surface nonlinear optics, Physical Review B, 59 (1999) 12632-12640.
[32] H.-F. Wang, W. Gan , R. Lu , Y. Rao , B.-H. Wu, Quantitative spectral and orientational analysis in surface sum frequency generation vibrational spectroscopy (SFG-VS), International Reviews in Physical Chemistry, 24 (2005) 191-256.
[33] K. Siegbahn, Electron spectroscopy for atoms, molecules, and condensed matter, Reviews of Modern Physics, 54 (1982) 709-728.
[34] T.A. Carlson, Photoelectron and Auger Spectroscopy, Springer, Boston, MA 1975.
[35] W.S.M. Werner, Electron transport in solids for quantitative surface analysis, Surface and Interface Analysis, 31 (2001) 141-176.
[36] R. Schlögl, In situ Characterisation of Practical Heterogeneous Catalysts, in: M. Baerns (Ed.) Basic Principles in Applied Catalysis, Springer Berlin Heidelberg, Berlin, Heidelberg, 2004, pp. 321-360.
[37] V.V. Kaichev, I.P. Prosvirin, V.I. Bukhtiyarov, H. Unterhalt, G. Rupprechter, H.-J. Freund, High-Pressure Studies of CO Adsorption on Pd(111) by X-ray Photoelectron Spectroscopy and Sum-Frequency Generation, The Journal of Physical Chemistry B, 107 (2003) 3522-3527.
[38] C. Rameshan, W. Stadlmayr, C. Weilach, S. Penner, H. Lorenz, M. Hävecker, R. Blume, T. Rocha, D. Teschner, A. Knop-Gericke, R. Schlögl, N. Memmel, D. Zemlyanov, G. Rupprechter, B. Klötzer, Subsurface-Controlled CO2 Selectivity of PdZn Near-Surface Alloys in H2 Generation by Methanol Steam Reforming, Angewandte Chemie International Edition, 49 (2010) 3224-3227.

[39] J.S. Luo, R.G. Tobin, D.K. Lambert, G.B. Fisher, C.L. DiMaggio, CO adsorption site occupation on Pt(335): a quantitative investigation using TPD and EELS, Surface Science, 274 (1992) 53-62.
[40] J.Z. Xu, J.T. Yates, terrace width effect on adsorate vibrations - a comparison of Pt(335) and Pt(112) for chemisorption of CO, Surface Science, 327 (1995) 193-201.
[41] K. Hayek, B. Jenewein, B. Klötzer, W. Reichl, Surface reactions on inverse model catalysts: CO adsorption and CO hydrogenation on vanadia- and ceria-modified surfaces of rhodium and palladium, Topics in Catalysis, 14 (2000) 25-33.
[42] G.A. Somorjai, C.M. Kim, C. Knight, Building of Complex Catalysts on Single-Crystal Surfaces, Surface Science of Catalysis, American Chemical Society1992, pp. 108-129.
[43] H. Li, J.-I.J. Choi, W. Mayr-Schmölzer, C. Weilach, C. Rameshan, F. Mittendorfer, J. Redinger, M. Schmid, G. Rupprechter, Growth of an Ultrathin Zirconia Film on Pt3Zr Examined by High-Resolution X-ray Photoelectron Spectroscopy, Temperature-Programmed Desorption, Scanning Tunneling Microscopy, and Density Functional Theory, The Journal of Physical Chemistry C, 119 (2015) 2462-2470.
[44] S. Coombs, A. Dameron, C. Engtrakul, S. Pylypenko, J. Lee, T.S. Olson, C. Bochert, T. Gennett, L. Simpson, B. Pivovar, H.N. Dinh, The Influence of Surfaces and Deposition Processes on Pt Structure and Properties, ECS Transactions, 33 (2010) 221-228.
[45] D.M. Hausmann, R.G. Gordon, Surface morphology and crystallinity control in the atomic layer deposition (ALD) of hafnium and zirconium oxide thin films, Journal of Crystal Growth, 249 (2003) 251-261.
[46] W.M.M. Kessels, H.C.M. Knoops, S.A.F. Dielissen, A.J.M. Mackus, M.C.M. van de Sanden, Surface reactions during atomic layer deposition of Pt derived from gas phase infrared spectroscopy, Applied Physics Letters, 95 (2009) 013114.
[47] T. Aaltonen, M. Ritala, Y.-L. Tung, Y. Chi, K. Arstila, K. Meinander, M. Leskelä, Atomic layer deposition of noble metals: Exploration of the low limit of the deposition temperature, Journal of Materials Research, 19 (2004) 3353-3358.
[48] T. Aaltonen, M. Ritala, T. Sajavaara, J. Keinonen, M. Leskela, Atomic layer deposition of platinum thin films, Chemistry of Materials, 15 (2003) 1924-1928.
[49] H.E. Swanson, E. Tatge, R.K. Fuyat, Standard X-ray diffraction powder patterns (1953).
[50] J. Stocker, R. Collongues, Sur la Preparation de Solutions Solides Cubiques de la Zircone, Comptes Rendus Hebdomadaires Des Seances De L Academie Des Sciences, 245 (1957) 695-697.
[51] P. Scherrer, Bestimmung der inneren Struktur und der Größe von Kolloidteilchen mittels Röntgenstrahlen, Kolloidchemie Ein Lehrbuch, Springer Berlin Heidelberg 1912, pp. 387-409.
[52] V. EKSLPA, Lithuania, SFG Spectrometer, 2018.
[53] G. Rupprechter, T. Dellwig, H. Unterhalt, H.-J. Freund, CO adsorption on Ni(100) and Pt(111) studied by infrared–visible sum frequency generation spectroscopy: design and application of an SFG-compatible UHV–high-pressure reaction cell, Topics in Catalysis, 15 (2001) 19-26.
[54] G. Rupprechter, Surface vibrational spectroscopy from ultrahigh vacuum to atmospheric pressure: adsorption and reactions on single crystals and nanoparticle model catalysts monitored by sum frequency generation spectroscopy, Physical Chemistry Chemical Physics, 3 (2001) 4621-4632.

[55] M. Roiaz, V. Pramhaas, X. Li, C. Rameshan, G. Rupprechter, Atmospheric pressure reaction cell for operando sum frequency generation spectroscopy of ultrahigh vacuum grown model catalysts, Review of Scientific Instruments, 89 (2018) 045104.
[56] M. Corva, A. Ferrari, M. Rinaldi, Z. Feng, M. Roiaz, C. Rameshan, G. Rupprechter, R. Costantini, M. Dell'Angela, G. Pastore, G. Comelli, N. Seriani, E. Vesselli, Vibrational fingerprint of localized excitons in a two-dimensional metal-organic crystal, Nature Communications, 9 (2018) 4703.
[57] W.G. Roeterdink, J.F.M. Aarts, A.W. Kleyn, M. Bonn, Broadband Sum Frequency Generation Spectroscopy to Study Surface Reaction Kinetics: A Temperature-Programmed Study of CO Oxidation on Pt(111), The Journal of Physical Chemistry B, 108 (2004) 14491-14496.
[58] K. Domen, A. Bandara, J. Kubota, K. Onda, A. Wada, S.S. Kano, C. Hirose, SFG study of unstable surface species by picosecond pump–probe method, Surface Science, 427-428 (1999) 349-357.
[59] E.H.G. Backus, A. Eichler, A.W. Kleyn, M. Bonn, Real-Time Observation of Molecular Motion on a Surface, Science, 310 (2005) 1790.
[60] NIST Mass Spec Data Center, S.E. Stein, director, Infrared Spectra, Eds. P.J. Linstrom and W.G. Mallard, National Institute of Standards and Technology, Gaithersburg MD, 20899, 2017.
[61] G. Rupprechter, T. Dellwig, H. Unterhalt, H.J. Freund, High-Pressure Carbon Monoxide Adsorption on Pt(111) Revisited: A Sum Frequency Generation Study, The Journal of Physical Chemistry B, 105 (2001) 3797-3802.
[62] K. Gustafsson, S. Andersson, Infrared spectroscopy of physisorbed and chemisorbed O2 on Pt(111), The Journal of Chemical Physics, 120 (2004) 7750-7754.
[63] C. Klünker, M. Balden, S. Lehwald, W. Daum, CO stretching vibrations on Pt(111) and Pt(110) studied by sumfrequency generation, Surface Science, 360 (1995) 104-111.
[64] X. Su, P.S. Cremer, Y.R. Shen, G.A. Somorjai, High-Pressure CO Oxidation on Pt(111) Monitored with Infrared−Visible Sum Frequency Generation (SFG), Journal of the American Chemical Society., 119 (1997) 3994-4000.
[65] H. Härle, U. Metka, H.-R. Volpp, J. Wolfrum, Pressure dependence (10 -8 –1000 mbar) of the vibrational spectra of CO chemisorbed on polycrystalline platinum studied by infrared–visible sum-frequency generation, Phys. Chem. Chem. Phys., 1 (1999) 5059-5064.
[66] S. Baldelli, A.S. Eppler, E. Anderson, Y.R. Shen, G.A. Somorjai, Surface enhanced sum frequency generation of carbon monoxide adsorbed on platinum nanoparticle arrays, Journal of Chemical Physics, 113 (2000) 5432-5438.
[67] F. Fournier, W. Zheng, S. Carrez, H. Dubost, B. Bourguignon, A restructuring of the CO/Pt(111) surface induced by femtosecond laser pulses, Surface Science, 528 (2003) 177–182.
[68] E.H.G. Backus, M. Bonn, A quantitative comparison between reflection absorption infrared and sum-frequency generation spectroscopy, Chemical Physics Letters, 412 (2005) 152-157.
[69] P. Galletto, H. Unterhalt, G. Rupprechter, The molecular orientation of CO on Pd(111): a polarization-dependent SFG study, Chemical Physics Letters, 367 (2003) 785-790.

[70] X. Li, M. Roiaz, V. Pramhaas, C. Rameshan, G. Rupprechter, Polarization-Dependent SFG Spectroscopy of Near Ambient Pressure CO Adsorption on Pt(111) and Pd(111) Revisited, Topics in Catalysis, (2018).
[71] B.E. Hayden, K. Kretzschmar, A.M. Bradshaw, An infrared study of the adsorption of CO on a stepped platinum surface, Surface Science, 149 (1985) 394-406.
[72] E. Schweizer, B.N.J. Persson, M. Tüshaus, D. Hoge, A.M. Bradshaw, The potential energy surface, vibrational phase relaxation and the order-disorder transition in the adsorption system Pt{111}-CO, Surface Science, 213 (1989) 49-89.
[73] R.A. Olsen, P.H.T. Philipsen, E.J. Baerends, CO on Pt(111): A puzzle revisited, The Journal of Chemical Physics, 119 (2003) 4522-4528.
[74] P. Deshlahra, J. Conway, E.E. Wolf, W.F. Schneider, Influence of Dipole-Dipole Interactions on Coverage-Dependent Adsorption: CO and NO on Pt(111), Langmuir, 28 (2012) 8408-8417.
[75] R.F. Steiger, J.M. Morabito Jr, G.A. Somorjai, R.H. Muller, A study of the optical properties and of the physical adsorption of gases on silver single crystal surfaces by low energy electron diffraction and ellipsometry, Surface Science, 14 (1969) 279-304.
[76] K.H. Ludlum, R.P. Eischens, Carbonyl formation in stainless steel infrared cells, Surface Science, 40 (1973) 397-398.
[77] X. Zhang, H. Wang, B.Q. Xu, Remarkable nanosize effect of zirconia in Au/ZrO2 catalyst for CO oxidation, Journal of Physical Chemistry B, 109 (2005) 9678-9683.
[78] J.H. Bitter, K. Seshan, J.A. Lercher, The State of Zirconia Supported Platinum Catalysts for CO2/CH4 Reforming, Journal of Catalysis, 171 (1997) 279-286.
[79] M. Corva, Z. Feng, C. Dri, F. Salvador, P. Bertoch, G. Comelli, E. Vesselli, Carbon dioxide reduction on Ir(111): stable hydrocarbon surface species at near-ambient pressure, Physical Chemistry Chemical Physics, 18 (2016) 6763-6772.
[80] SPECS GmbH, Useful Information and Facts about the Practice of Sputtering, SPECS GmbH.
[81] National Physical Laboratory, Ar Sputtering Yields at 0°, National Physics Laboratory, Hampton Road, Teddington, Middlesex, TW11 0LW, 2005.
[82] M. Tüshaus, E. Schweizer, P. Hollins, A.M. Bradshaw, Yet another vibrational study of the adsorption system Pt{111}-CO, Journal of Electron Spectroscopy and Related Phenomena, 44 (1987) 305-316.
[83] L. Manceron, B. Tremblay, M.E. Alikhani, Vibrational Spectra of PtCO and Pt(CO)2 Isolated in Solid Argon: Trends in Unsaturated Group 10 Metal Carbonyl Molecules, The Journal of Physical Chemistry A, 104 (2000) 3750-3758.
[84] T. Zubkov, G.A. Morgan, J.T. Yates, Spectroscopic detection of CO dissociation on defect sites on Ru(109): implications for Fischer–Tropsch catalytic chemistry, Chemical Physics Letters, 362 (2002) 181-184.
[85] J. Engbæk, O. Lytken, J.H. Nielsen, I. Chorkendorff, CO dissociation on Ni: The effect of steps and of nickel carbonyl, Surface Science, 602 (2008) 733-743.
[86] J. Goldstein, D.E. Newbury, P. Echlin, D.C. Joy, C. Fiori, E. Lifshin, Scanning Electron Microscopy and X-Ray Microanalysis, Springer US 1981.
[87] R.J. Wrobel, S. Becker, Carbon and sulphur on Pd(111) and Pt(111): Experimental problems during cleaning of the substrates and impact of sulphur on the redox properties of CeOx in the CeOx/Pd(111) system, Vacuum, 84 (2010) 1258-1265.
[88] A.V. Naumkin, A. Kraut-Vass, S.W. Gaarenstroom, and, C.J. Powell, NIST X-ray Photoelectron Spectroscopy (XPS) Database, Version 3.5, Measurement Services Division

of the National Institute of Standards and Technology (NIST) Material Measurement Laboratory (MML), 2000.
[89] R.B. Konda, C. White, D. Thomas, Q. Yang, A.K. Pradhan, Electrical characteristics of ZrO2/GaAs MOS capacitor fabricated by atomic layer deposition, Journal of Vacuum Science & Technology A: Vacuum, Surfaces, and Films, 31 (2013) 041505.
[90] E.M. Pazhetnov, S.V. Koshcheev, A.I. Boronin, Formation Mechanism and Structure of Monatomic Carbon Films in Ethylene Decomposition on the Pt(111) Surface According to XPS Data, Kinetics and Catalysis, 44 (2003) 414-419.
[91] B. Tränkenschuh, N. Fritsche, T. Fuhrmann, C. Papp, J.F. Zhu, R. Denecke, H.P. Steinrück, A site-selective in situ study of CO adsorption and desorption on Pt(355), The Journal of Chemical Physics, 124 (2006) 074712.
[92] R. Toyoshima, M. Yoshida, Y. Monya, K. Suzuki, K. Amemiya, K. Mase, B.S. Mun, H. Kondoh, A high-pressure-induced dense CO overlayer on a Pt (111) surface: a chemical analysis using in situ near ambient pressure XPS, Physical Chemistry Chemical Physics, 16 (2014) 23564-23567.
[93] D. Vogel, C. Spiel, Y. Suchorski, A. Trinchero, R. Schlögl, H. Grönbeck, G. Rupprechter, Local Catalytic Ignition during CO Oxidation on Low-Index Pt and Pd Surfaces: A Combined PEEM, MS, and DFT Study, Angewandte Chemie International Edition, 51 (2012) 10041-10044.
[94] C. Spiel, D. Vogel, R. Schlögl, G. Rupprechter, Y. Suchorski, Spatially coupled catalytic ignition of CO oxidation on Pt: mesoscopic versus nano-scale, Ultramicroscopy, 159 (2015) 178-183.
[95] S.C. Chang, L.-W.H. Leung, M.J. Weaver, Comparisons between coverage-dependent infrared frequencies for carbon monoxide adsorbed on ordered platinum (111),(100), and (110) in electrochemical and ultrahigh-vacuum environments, The Journal of Physical Chemistry, 93 (1989) 5341-5345.
[96] J. Xu, J.T.Y. Jr., Catalytic oxidation of CO on Pt(335): A study of the active site, The Journal of Chemical Physics, 99 (1993) 725-732.
[97] O. Pozdnyakova, D. Teschner, A. Wootsch, J. Kröhnert, B. Steinhauer, H. Sauer, L. Toth, F.C. Jentoft, A. Knop-Gericke, Z. Paál, R. Schlögl, Preferential CO oxidation in hydrogen (PROX) on ceria-supported catalysts, part I: Oxidation state and surface species on Pt/CeO2 under reaction conditions, Journal of Catalysis, 237 (2006) 1-16.
[98] M.S. Chen, Y. Cai, Z. Yan, K.K. Gath, S. Axnanda, D.W. Goodman, Highly active surfaces for CO oxidation on Rh, Pd, and Pt, Surface Science, 601 (2007) 5326-5331.